Dissertation
submitted to the
Combined Faculty of the Natural Sciences and for Mathematics
of Heidelberg University, Germany
for the degree of
Doctor of Natural Sciences

Put forward by

M.Sc. Damian Müll

born in Gießen

Oral examination: 10$^{\text{th}}$ January 2023

Photodetachment studies of negative ions at the Cryogenic Storage Ring

Photoablösungsstudien von negativen Ionen am kryogenen Speicherring

Die vorliegende Arbeit beschäftigt sich mit den experimentellen Messungen des Photoablösungsprozesses von Si^- und Al_4^-. Die Messungen wurden am kryogenen Speicherring (CSR), der sich am Max-Planck-Institut für Kernyphysik befindet, durchgeführt. Si^- wird bei einer Umgebungstemperatur von $T < 10\,K$ mit einer Speicherzeit von bis zu 2000 s gespeichert. Die verringerte Schwarzkörperstrahlung ermöglicht es den Zerfall der langlebigen ^2D Zustände und der schwach gebundenen ^2P Zustände zu verfolgen. Unter Verwendung von Dauerstrichlasern und gepulsten Lasern, wurde die Lebensdauer der ^2P Zustände auf $\tau = (22.5 \pm 2.5)s$ bestimmt. Für die langlebigen ^2D Zustände ist eine untere Grenze von $\tau_r > 5.7\,h$ (innerhalb eines 90% Konfidenzintervalls) gemessen worden. Weiterhin wurden Multi-Configuration Dirac-Hartree-Fock (MCDHF) Rechnungen zu den radiativen Lebensdauern der jeweiligen Zustände durchgeführt, die eine sehr gute Übereinstimmung mit den vorliegenden Messungen zeigen.

Der zweite Teil der Studien behandelt die Messung spontaner Kühlung von gespeicherten Al_4^- Ionen bei sehr langen Speicherzeiten. Es werden Messungen vorgestellt, die es uns erlauben die Cluster Kühlungsraten für bis zu 30 min zu beobachten. Anschließend vergleichen wir diese Ergebnisse mit vorherigen Messungen, die bei Raumtemperatur durchgeführt wurden. Die Kühlungsraten sind limitiert durch die Umverteilung von Schwingungsenergien innerhalb des Moleküls, die wir langsames Austauschmodell nennen. Kombiniert mit wiederkehrender Fluoreszenz für Energien oberhalb des ersten elektronischen angeregten Zustands, folgen sie den beobachteten Kühlraten.

Photodetachment studies of negative ions at the Cryogenic Storage Ring

In the present work, experimental studies of the photodetachment process of the Si^- and Al_4^- systems are presented. The measurements were carried out at the Cryogenic Storage Ring (CSR) facility located at the Max Planck Institute for Nuclear Physics in Heidelberg. By storing Si^- for up to 2000 s in the $T < 10\,K$ CSR environment, making use of the reduced blackbody radiation field inside the CSR, we were able to monitor the decay of long-lived ^2D states as well as the weakly bound ^2P states. Employing a set of continuous wave and pulsed lasers, the lifetime for the ^2P states were found to be $\tau = (22.5 \pm 2.5)s$. For the ^2D states, a lower limit of $\tau_r > 5.7\,h$ (within a confidence level of 90%) was measured. Furthermore, Multi-Configuration Dirac-Hartree-Fock (MCDHF) calculations were performed on the radiatiave lifetimes of the respective states, which show very good agreement with the present measurement. The second part of the studies focuses on the study of spontaneous cooling of stored Al_4^- ions at very long time scales. Here, we present measurements that allow us to monitor the cluster cooling rates for up to 30 min and we compare those results to previous measurements at a room temperature device. We find that the cooling time scale is limited by the redistribution of vibrational energy inside the molecule, which we call slow exchange model, and in combination with recurrent fluorescence for energies above the first electronic excited state, they match the observed cooling rates.

Contents

Contents

List of Figures

List of Tables

Acronyms

AEA adiabatic electron affinity

ASFs atomic state functions

CI Configuration Interaction

COMPACT Cold Movable Particle Counter

CSFs configuration state functions

CSR Cryogenic Storage Ring

CW continuous wave

DR dissociative recombination

EA electron affinity

HF Hartree-Fock

IC internal conversion

IIC inverse internal conversion

IR infrared laser

IVR internal vibrational redistribution

LPTS laser photodetachment threshold spectroscopy

MCDHF Multi-Configuration Dirac-Hartree-Fock

MCP Microchannel Plates

NICE Neutral Imaging in Cold Environment

OPO Optical Parametric Oscillator

PES photodetachment electron spectroscopy

RF recurrent fluorescence

RMS Root Mean Square

RRKM Rice-Ramsberger-Kassel-Marcus

TSR Test Storage Ring

VAE vertical attachment energy

VDE vertical detachment energy

Vis visible laser

Chapter 1

Introduction

Negative ions have an extra electron attached to the neutral parent atom or molecular species, which in total gives it a negative charge. In comparison to positive ions, the extra negative charge is only loosely bound, and therefore anions are much more fragile than neutrals or cations. This fragility of the negative ions makes studies particularly interesting, since they allow for sensitive tests of theoretical calculations.

Gas phase negative ions were first mentioned by Sir Joseph Thomson (Thomson 1913) during his cathode ray experiments, where he separated particles by their charge to mass ratios. Most of the early studies have been summarized in Massey 1938. Systematic studies on the binding energies for various atoms were reviewed by Hotop and Lineberger 1975, and have been updated by T. Andersen, Haugen, and Hotop 1999 and T. Andersen 2004. Comprehensive reviews have also been written by Pegg 2004 on photodetachment experiments and resonances in photodetachment cross sections by Buckman and Clark 1994.

First signs that negative ions are also relevant in the astrophysical environment are given in Goudsmit and Wu 1934 and Wildt 1939. Furthermore, carbon containing molecular ions have been detected in interstellar space recently, such as C_6H^- (McCarthy et al. 2006) and C_3N^- (Thaddeus et al. 2008). This has led to a possible link of diffuse interstellar bands with dipole-bound excited states of molecular negative ions (Sarre 2006). In fact, in the early universe collisions between H^- and H are the main formation mechanism for primordial H_2. The importance of this process that proceeds through short-lived $(H_2^-)^*$ resonances, was first recognized by Peebles and Dicke 1968, and confirmed by measurements (Kreckel et al. 2010) and models (Galli and Palla 2013).

In the D-region of the earth's ionosphere, photodetachment of negative ions and the inverse process of radiative electron attachment are primarily responsible for the free electron density, which can have a big impact on satellite- and radio-based signal communication. Here, especially O^- is a source of free electrons during the day (Pavlov

2014).

Interestingly, negative ions also play a role in fusion reactors, where fusion is happening in a toroidal magnetic field (Tokamak) such as at the International Thermonuclear Experimental Reactor (ITER) (Umeda et al. 2014). High temperatures need to be reached in order to make fusion possible, which is achieved by injection of strong neutral atomic beams. For this purpose, strong beams of H^- and D^- are used, which are neutralized by gas stripping or photodetachment. At the International Experimental Fusion Reactor (ITER) negative ion beam currents of $40\,A$ will be needed to achieve sufficient heating (Fantz et al. 2007).

Only a few anions have several bound levels, like Sc^-, Al^- or C^- (see T. Andersen, Haugen, and Hotop 1999) and even fewer have dipole-allowed transitions, which would be suitable for laser cooling. Os^- (Warring et al. 2009), Ce^- (Walter et al. 2011), La^- (Jordan et al. 2015) and more recently U^- (Tang et al. 2021) have been found to have dipole-allowed transitions between anionic states. As an interesting application, those might be utilized to cool antiprotons sympathetically (Kellerbauer and Walz 2006). This would even enable high precision measurements on antimatter gravity or tests on the charge-, parity- and time-symmetry conservation (CPT-theorem).

1.1 Atomic Negative Ions

For a charged particle like an electron, there is no long range attractive Coulomb force to the neutral atom. Considering basic principles of electrostatics the existence of negative ions seems questionable. However, when the neutral and electron are close enough to each other, the electron will rearrange the electron cloud around the neutral. The polarization of the electron orbitals, together with the shielded neutral, lead to an higher order electrostatic force. Consequently, the electron is attracted by the induced dipole and gets trapped. In this process the atom gains the binding energy of the negative ion, which is also called electron affinity (EA) of the neutral atom. It is defined as the difference between the total energy of the ground state of the neutral atom A and the ground state of the respective negative ion A^-. An energy schematic is shown in Fig. 1.1.

$$\text{EA}(A) = E_{tot}(A) - E_{tot}(A^-) \tag{1.1}$$

Ground states are defined as the lowest hyperfine structure levels of A and A^-, respectively. A positive value for EA corresponds to a stable negative ion. Anions with a positive EA typically exist long enough to play a role in chemical reactions and enable direct experimental investigations. In case of anions with a negative EA the time scale ($\approx ps$) is too short to play a significant role in any kind of chemical reaction.
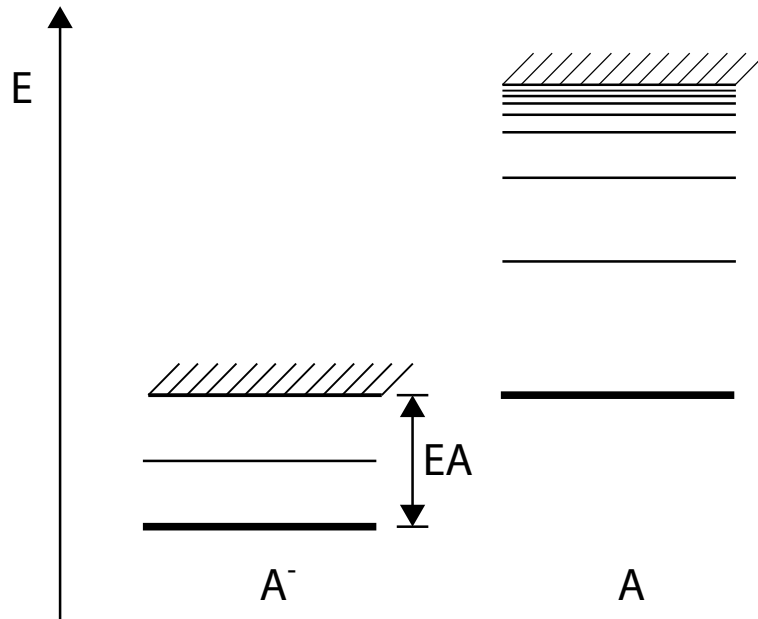
Figure 1.1: Schematic of the energy levels in a negative ion A$^-$ and the respective atom A. (figure is adapted from Pegg 2004)

With the absence of a long range Coulomb potential, the electron is only bound to the atom while being close to the atom. This system is much less stable than neutrals or positive ions. This is plausible, as the binding energy of negative ions is determined by the induced dipole potential, which is proportional to r^{-4}. Whereas electrons in the neutral atoms are bound by the Coulomb potential, which is proportional to r^{-1}, with r being the distance from the center of the nucleus. Those different binding mechanisms lead to various differences between positive and negative ions. A first look at the EA shows that it is approximately one order of magnitude lower than the ionization energy for the same atom. One simple example is the hydrogen atom H, where the EA is $0.75\,\text{eV}$ and the ionization potential is $13.6\,\text{eV}$. Hence, the short-range induced dipole potential allows for a small and limited number of states at most. Most stable negative ions only have one bound state. Often, only the different fine-structure levels of up to three term splitting levels of the ground state configurations are bound.

First studies of negative ion energies were performed by extrapolating ionization potentials from neutral atoms and positive ions to the negative ions isoelectronically. However, this often underestimates binding energies for known stable negative ions. The independent particle model, which is well known from the quantum mechanical description, failed to give accurate results even for the simplest negative ion H$^-$. As mentioned before, the binding energy is given by the correlated motions of the electrons, which plays a much larger role for negative ions. In order to predict the EA precisely, electron correlation effects have to be taken into account in detail. An overview of different methods is given in Section 2.2.

1.2 Molecular Negative Ions

Moving on to negative molecules introduces new aspects, which complicate the description. The EA of a neutral molecule is defined as the binding energy of an electron to the molecule, as illustrated in Fig. 1.2. The energy difference from the ground vibrational and rotational state of the negative molecule to the ground vibrational and rotational state of the neutral is called adiabatic electron affinity (AEA). Often this transition is not the most likely to occur. In general three concepts of possible energy differences are useful and are shown in Fig. 1.2. The first one is the vertical detachment energy (VDE). It is defined as minimum energy needed to eject an electron from the negative ion, which is in its ro-vibrational and electronic ground state. For such a process there is no time for geometry relaxation, which means that both the neutral and the anion are at optimized equilibrium nuclear configuration (r_e) of the anion. Conceptually, the vertical attachment energy (VAE) is the analogous process, but it refers to the energy released from the addition of an electron to a neutral molecule, which is in its ro-vibrational and electronic ground state, at optimized geometries of the neutral. The same way the AEA may be explained by the difference in total energies between the neutral molecule and negative ion (both in their ro-vibrational and electronic ground state) at the corresponding equilibrium nuclear configurations r_e. Those values are summarized in the following equations:

$$AEA = E(\text{optimized neutral}) - E(\text{optimized anion}) \tag{1.2}$$

$$VDE = E(\text{neutral with optimized anion geometry}) - E(\text{optimized anion}) \tag{1.3}$$

$$VAE = E(\text{optimized neutral}) - E(\text{anion with optimized neutral geometry}) \tag{1.4}$$

1.3 Production of Negative Ions

Since negative ions and molecules are systems with diffuse outer orbitals, they are likely to be destroyed in particle-particle collisions even at low energies. Their production is challenging because it has to compete with a more probable destruction process. For the formation of a negative ion, an electron has to be attached to a neutral atom or molecule. With the electron having a kinetic energy E_{kin} when it attaches to the neutral atom, the sum of the electron affinity and E_{kin} has to be disposed. For an atom, possible attachment processes are radiative capture, charge transfer and three-body capture. The attachment processes for a molecule are dissociative attachment,
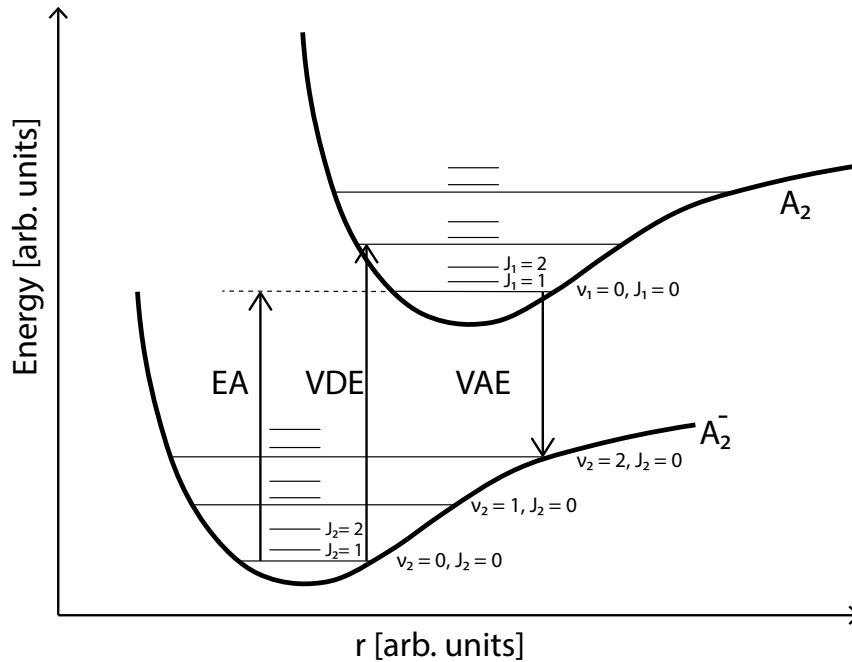
Figure 1.2: Schematic of diatomic molecular potentials for the molecule A_2 and the respective anion A_2^-. The principles are applicable for diatomic and polyatomic molecules. The transitions given are the adiabatic electron affinity (AEA), the vertical detachment energy (VDE), and vertical attachment energy (VAE). Vibrational and rotational excited levels are shown as horizontal lines inside the potentials. This figure was adapted from Rienstra-Kiracofe et al. 2002.

resonant capture or ion-pair production. In the radiative attachment process excessive energy is released with a photon, and thus the radiative capture is the opposite effect of photodetachment. For dissociative attachment, the energy is released by breaking up the molecule, while associative detachment is the inverse process. In the case of high pressures, three-body capture and charge transfer become more dominant, while in a low pressure environment radiative and dissociative attachment processes happen more often. Sometimes the kinetic energy of the electron converts to an excited state of the atom. Often those excited atoms are more polarizable than atoms in the ground state and are more likely to capture an extra electron. Furthermore, by first exciting the atom and then capturing the electron, those negative ions are typically more often in an excited state than in the ground state.

Attachment processes are employed in different types of ion sources. Using a volume source, negative ions are produced by electron-atom or electron-molecule collisions in a gaseous discharge. In the case of surface sources, negative ions are produced by having heavy particles colliding onto surfaces with low work functions. Those two types of sources are also reviewed by Alton 1989. A different type of source is utilized in charge transfer collisions, as used by Donnally and Thoeming 1967. The two-step process of neutralization followed by capture of electrons yields a higher fraction of metastable

negative ions.

A very versatile source is the sputter ion source, and it is commonly used for experiments. The commercial caesium beam sputter sources are based on the design of Middleton 1989. This type of source has been used for the present work. Caesium (Cs) is heated in an oven and ionized by an ionizer coil. The Cs^+ ion beam is used for sputtering the target material from a surface. In order to accelerate the Cs^+ ions towards the cathode, a potential is applied between the cathode surface and the ionizer. Additionally, the non-ionized Cs vapor condenses on the cool cathode resulting in a lower work function of the sputter surface, thus providing a higher chance of attaching an extra electron to the sputtered atom or molecule. Finally, the ions are extracted through a thin hole in the ionizer. This type of ion source is shown schematically in Fig. 1.3.
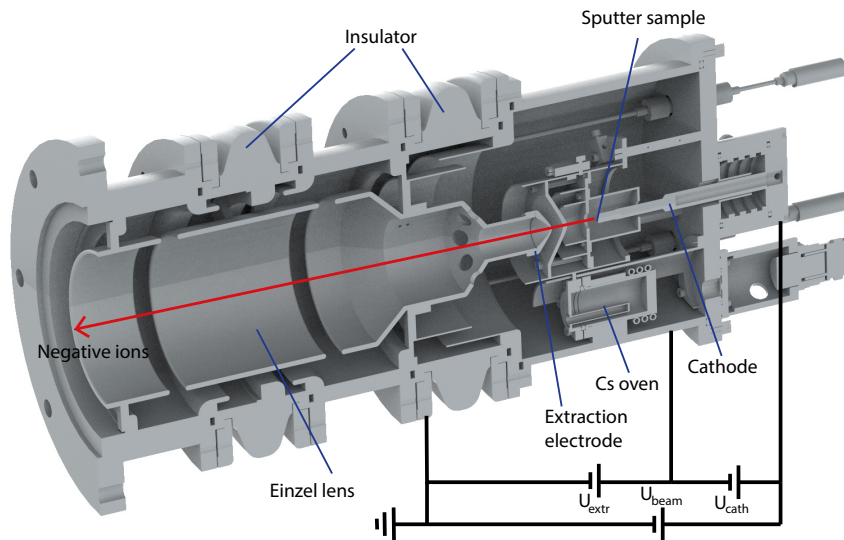
Figure 1.3: Schematic of a Cs sputter ion source. Cs vapor is produced in an oven, then ionized and accelerated towards the cathode. The negative ions are accelerated by the same potential into the opposite direction and extracted by another potential.

1.4 The Photodetachment process

Most experiments with negative ions rely on their destruction in a defined way, allowing for studies of the structure and dynamics of the anions. The detachment process can be understood as the transition from a bound state into a continuum state that includes the atom and the free electron. Both photon and particle impact can be used to induce the electron detachment process. Here we focus on photon interactions. Studying the relation of cross section and energy of the photon helps to understand the interaction
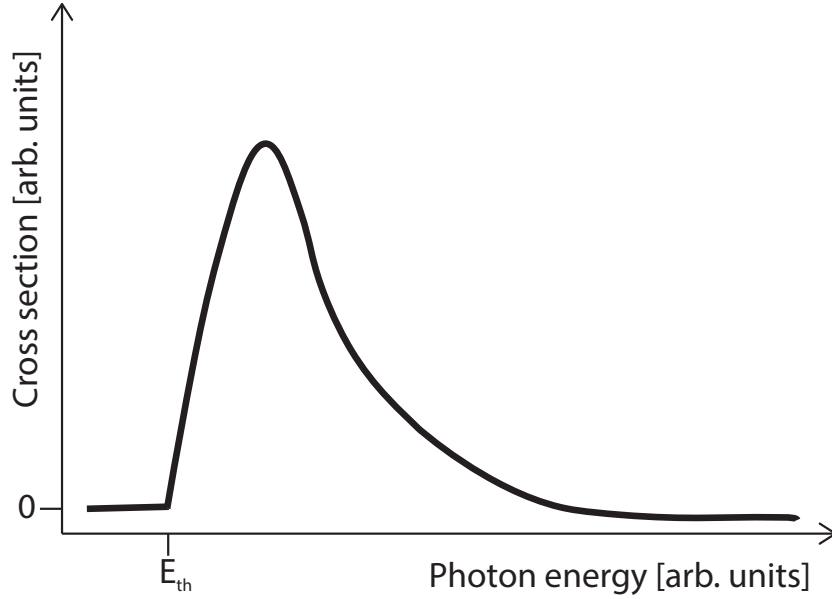
Figure 1.4: Typical non-resonant photodetachment cross section for one electron detachment.

of the negative ions and radiation. A typical cross section for single electron photodetachment is shown in Fig. 1.4. It starts at zero, rises to a maximum after the threshold energy E_{th} is reached and decreases afterwards. The threshold behavior, as well as resonance structures, play an important role, since they are often both involved in the correlated motion between the electrons.

The escape process by photodetachment is mainly described by the threshold behavior. The near-threshold cross section σ for detaching a single electron from the atomic negative ion is given by the Wigner Law (Wigner 1948), which is derived from Fermi's golden rule. The probability P going from an initial state $|\Psi_i>$ to a final state $<\Psi_f|$ following the interaction of a photon and an atom is given by:

$$P = \frac{2\pi}{\hbar}|<\Psi_f|D|\Psi_i>|^2\rho_f \tag{1.5}$$

Here D is the electric dipole coupling operator. ρ_f is the density of final states in the continuum, which is proportional to the square root of the energy E of the ejected electron.

$$\rho_f \propto \sqrt{E} \tag{1.6}$$

Once the detachment of the electron by a photon happened, the two-body three dimensional problem can be reduced to a one-body one dimensional problem as described in Farley 1989. The electron mass is replaced by the reduced mass μ and an effective potential $V_{\text{eff}}(r)$ is introduced:

$$V_{\text{eff}}(r) = V(r) + \frac{\hbar^2 l(l+1)}{2\mu r^2} \tag{1.7}$$

$V(r)$ is the potential from the atomic core and the second term refers to the centrifugal force, with l being the angular momentum of the outgoing electron. Since the photodetached (for photon energies close to the threshold) electron's velocity is low, the threshold behavior is governed by the long range behavior of the potential. This means that for large r the centrifugal barrier term ($\propto r^{-2}$) is the dominant term, with the potential term being proportional to r^{-4} (induced dipole potential). Hence, the cross section σ is described by

$$\sigma \propto k^{2l-1}, \tag{1.8}$$

where l is the angular momentum and k donates the linear momentum of the detached electron. Equation 1.8 is known as the Wigner threshold law. In terms of excess energy above threshold $E - E_{th}$, the cross section is given ($E > E_{th}$)

$$\sigma(E) \propto (E - E_{th})^{l+1/2} \tag{1.9}$$

and $\sigma(E) = 0$ for $E < E_{th}$. In case of the angular momentum of the ejected electron being zero ($l = 0$), the cross section will be given by

$$\sigma(E) \propto \sqrt{E}. \tag{1.10}$$

This type of energy dependence of the cross section is shown in Fig. 1.5 by the dotted line and is called s-wave. Applying the quantum mechanical selection rule for dipole interactions with $\Delta l = \pm 1$, and knowing that the photon has angular momentum of $l = 1$ means that the total angular momentum of the system after photodetachment changes. In case of the detached electron being in a s-state with $l = 0$ before photodetachment, the electron will leave the ion with the angular momentum of $l = 1$ after being photodetached. The corresponding energy dependence is shown as p-wave in Fig. 1.5. For electrons with a higher l in the anion, higher l contributions in the outgoing electron will be suppressed by the centrifugal barrier, which leads to $\Delta l = -1$ dominating near threshold. Other potentials, as the polarization potential, do not change the Wigner Law at threshold, but will limit the range of the Wigner Law.

Besides the smooth cross section at threshold, which is described by the Wigner Law, there often are also peaks in the cross section at a particular energy. Those peaks are referred to as resonances. Typically resonance structures in photodetachment spectra arise due to photoexcitation of unbound excited state in the negative ion and are found in the continuum above detachment level. These states will autodetach quickly after excitation.
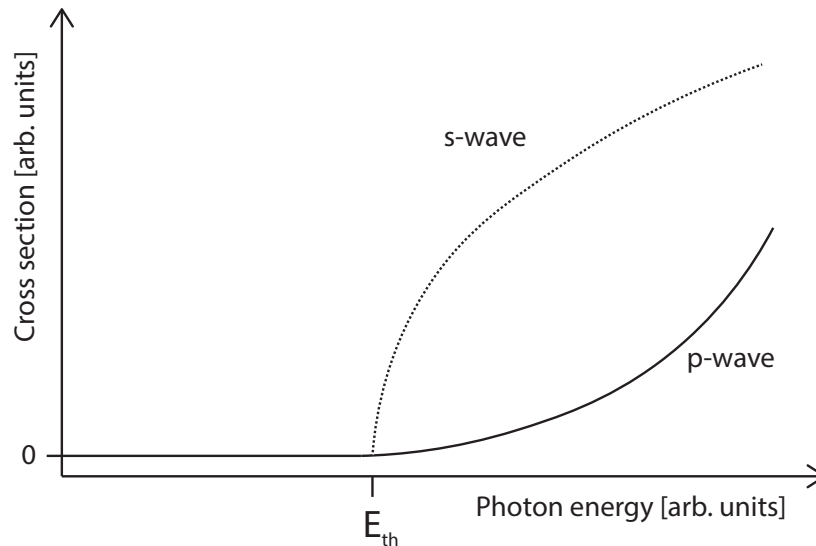
Figure 1.5: Energy dependence of the Wigner Law at the threshold for photodetachment for the s-wave ($\propto E^{1/2}$) and p-wave ($\propto E^{3/2}$) continuum.

1.5 Overview of the Cryogenic Storage Ring

The measurements carried out in this work were all performed at the Cryogenic Storage Ring (CSR) located at the Max Planck Institute for Nuclear Physics in Heidelberg. A detailed description of the storage ring and its capabilities and infrastructure is given in von Hahn et al. 2016. In the following section a short overview of the experiment will be given.

The CSR is an entirely electrostatic storage ring with a circumference of about 35 m, designed for the storage of positive and negative ions of up to 300 keV kinetic energy per charge unit. A photograph is shown in Fig. 1.6. By only using electrostatic elements, storage of atomic and molecular ions is achieved independent of their mass. This opens up the possibility of studies on molecules, clusters and even biomolecules. The inner parts of the CSR are designed to minimize heat entries from external environments. The experimental vacuum chambers can be cooled down to 4 K using a closed cycle helium system. This is achieved by a commercial cryostat (Linde) liquifying the gas down to 3 K. Inside the CSR, the helium is guided through cooling lines attached to copper blocks,which have copper stripes attached to the blocks and are connected to the experimental vacuum chambers that are wrapped in copper. The helium line is attached to to an aluminum shield, which is called 40 K radiation shield and surrounds the inner vacuum chambers of the CSR and the two helium line systems. After two more circulations inside CSR the helium line is connected to a second aluminum shield, which is called 80 K radiation shield. This shield is wrapped in superinsulation foil and is surrounding the 40 K radiation shield. Both shields reduce thermal radiation

Figure 1.6: Photograph of the Cryogenic Storage Ring (CSR). For demonstration purposes the outer walls of the vacuum chambers have not been mounted yet. (Credits: Christian Föhr 2013)

transport from the outer vacuum chamber (which is at room temperature) to the cold surface of the inner vacuum chamber.

Having the inner vacuum chambers at this low temperature of the $5\,\text{K}$ cooling line reduces thermal radiation dramatically. Furthermore, the chambers act as a cryopump, reducing the residual gas density down to $\leq 1000\,\text{cm}^{-3}$, equivalent to a room temperature pressure of $<10^{-14}$ mbar (von Hahn et al. 2016). This helps greatly in enhancing the lifetime of the stored particles, as electron stripping and capture processes are suppressed at low residual gas densities. These conditions of a low black body radiation field and long storage times, allow for stored molecules with a permanent dipole moment to cool into their rovibrational ground state by radiative cooling. This was shown for positive (O'Connor et al. 2016) and negative ions (C. Meyer et al. 2017). Furthermore, it enables measurements on very weakly bound metastable states of negative ions, such as Si^- presented in this work.

Atomic and molecular ions can be produced by various ion sources that can be mounted on two separate high-voltage platforms. The illustration in Fig. 1.7 shows an overview. After acceleration up to $60\,\text{keV}$ per charge unit (small platform) and $300\,\text{keV}$ per charge unit (large platform), the respective ions are mass selected by dipole mag-
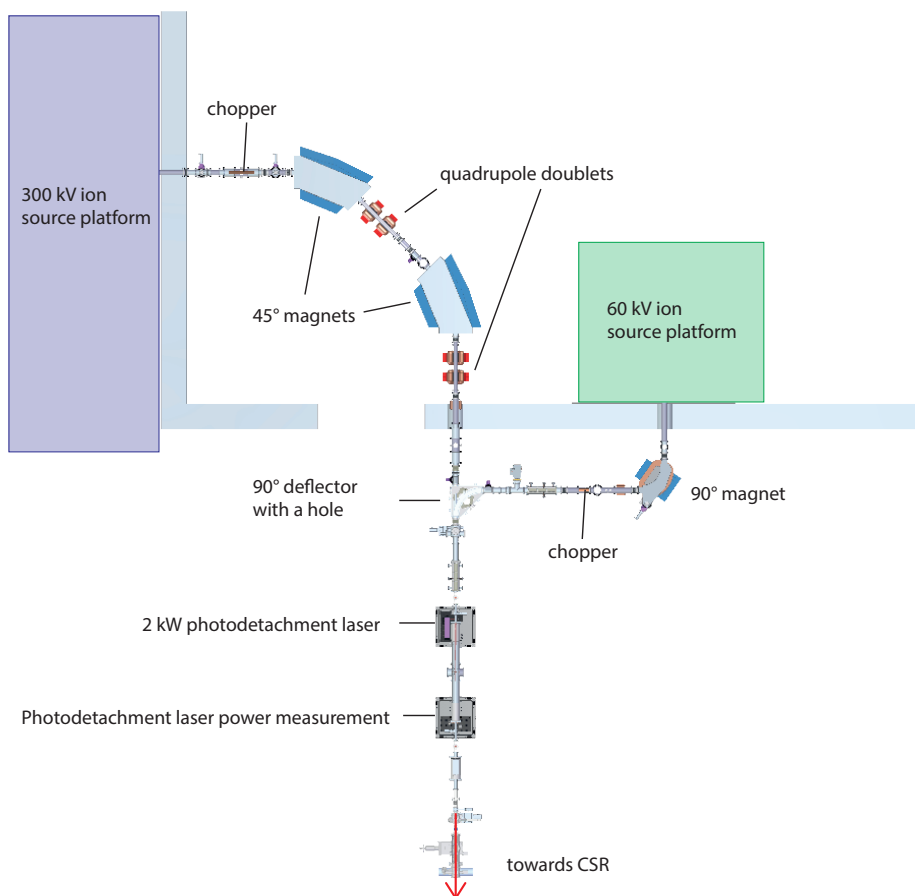
Figure 1.7: Overview of the ion source platforms and injection beamlines at the CSR facility. Besides the strong photodetachment laser used for ion-neutral experiments, this overview shows the key elements needed to guide the ions from either platform towards CSR. (Note that only part of the 300 keV is shown here.)

nets. The ions from the 300 keV ion source platform are then guided through a transfer beamline consisting of two magnetic quadrupole doublets and two electric quadrupole triplets for optimizing transfer and beam quality. Faraday cups and wirescanners are used as beam diagnostics. Moreover, parallel plate deflectors are installed right after both of the ion source platforms. By fast switching on hundreds of ns time scale of the parallel plate deflectors the respective ion beam is only allowed to pass through those deflector plates in a certain time window (chopper). The beamlines from both platforms merge in a large cylindrical 90° deflector with a hole in the rear plate. By switching the high voltage of the deflector plates, the beam from either platform can be guided towards the CSR. A more detailed description of the transfer beamline and the ring can be found in Florian Grussie 2016.

Typically, different experiments at the CSR are conducted in separate beamtime blocks, which last for a weak. Since many of the experiments, for example the electron cooler beamtimes, require high acceleration voltages in order to facilitate the cooling
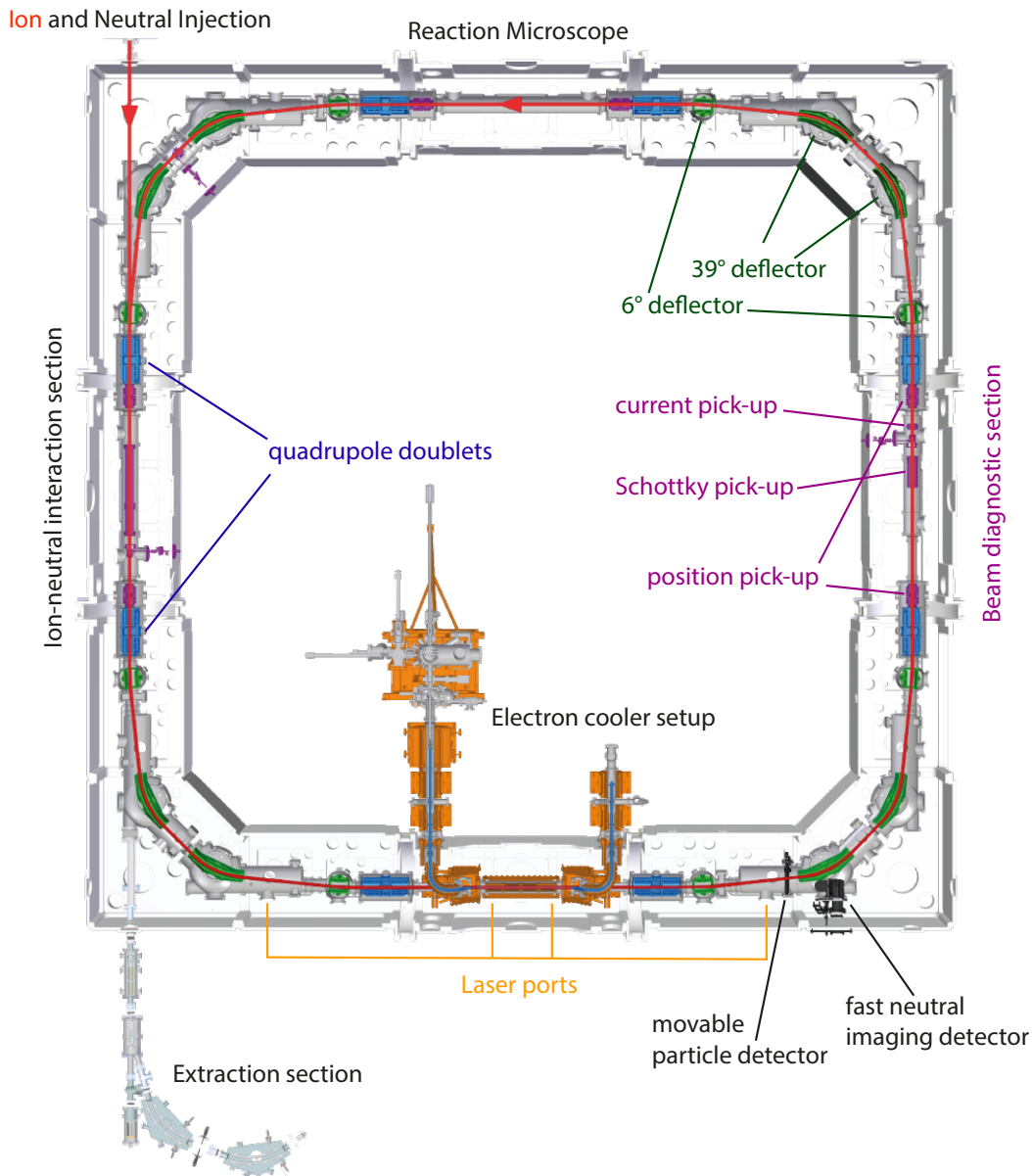
Figure 1.8: Schematic setup of the Cryogenic Storage Ring. In the upper left corner the ions are injected (red) and are guided counterclockwise through the CSR. The straight sections house the experimental setups. The deflecting elements, consisting of a pair of 6° and 39° deflectors located in every corner, are shown in green. Two quadrupole doublets in each of the straight sections are used for focussing. Beam diagnostics (the Schottky, current and position pick-up) are shown in purple. Viewports for the laser experiments are indicated by the orange lines. Both particle detectors used to detect products of ion-electron or ion-photon interactions are depicted.

process, switching of ion sources and changing the polarity of the large platform are time-consuming. Therefore, the smaller platform was chosen for the Si^- beamtimes, since kinetic energies of 60 keV were sufficient for this experiment.

A more detailed drawing of the CSR is shown in Fig. 1.8. After injection, the ions are kept on a closed orbit by two electrostatic 6° and 39° deflectors in each corner. For injection, the voltage on the first 6° deflector is switched from zero to nominal voltage by a high voltage switch. Beam shaping is done by focussing and defocussing with two quadrupole doublets in each straight section.

Experiments are performed in three of the straight sections, as shown in Fig. 1.8. The first straight section allows for ion-neutral merged beams experiments (F. Grussie et al. 2022). Reaction products for this type of experiment can either be analyzed with movable detectors at the second corner of the ring (not shown in the figure) or with a dedicated beam extraction section.

In the second straight section of the CSR, electron collision experiments can be performed, using a low-energy electron cooler. There are two possible types of applications that can be done using the electron beam. Firstly, phase-space cooling of the stored ions can be done in order to lower velocity spread and beam size. Secondly, it may be used as a collision target in merged beams configuration. A more detailed description of the electron cooler setup is given in Wilhelm 2019.

Relevant for this work are the laser experiments performed in the same straight section that houses the electron cooler. Different continuous wave laser beams as well as a pulsed Optical Parametric Oscillator can be guided through the experimental vacuum chambers, using viewports and mirrors inside the vacuum chambers. There is one configuration for quasi-colinear overlap, as well as two crossed-beam configurations. A detailed description of the laser setup at the CSR will be given in Section 3.1.

Collision products from photon- or electron-induced collisions are detected after the first 6° deflector in that section, further downstream of the ion-photon or ion-electron interaction region. For photodetachment studies, we will primarily detect neutralized atoms and molecules. Two detectors are available for this purpose and are shown in Fig. 1.9. The Neutral Imaging in Cold Environment (NICE) detector is a single particle detector based on Microchannel Plates (Becker 2016), combined with a phosphor screen, which allows imaging of the fragment positions. It is an excellent tool to study fragmentation kinematics for dissociative recombination and to demonstrate transverse cooling. The Cold Movable Particle Counter (COMPACT) (Spruck et al. 2015) is a movable single particle detector that is also based on MCP detection, but without imaging capabilities. It allows detection of charged and neutral fragments. Its dark count rate is $< 0.1\,s^{-1}$, while the NICE dark count rate is much higher $(< 50\,s^{-1})$ due to its larger active MCP area. Both detectors have a heating element connected to their MCPs. This is needed because the resistance of the MCPs are depending strongly on the temperature and can go easily from $50\,M\Omega$ at room temperature up to $\approx 100\,G\Omega$ at 20 K. The heating elements give the option to keep the MCPs warmer than the vacuum chambers and improve the high-rate response of the channel plates. Both detectors were
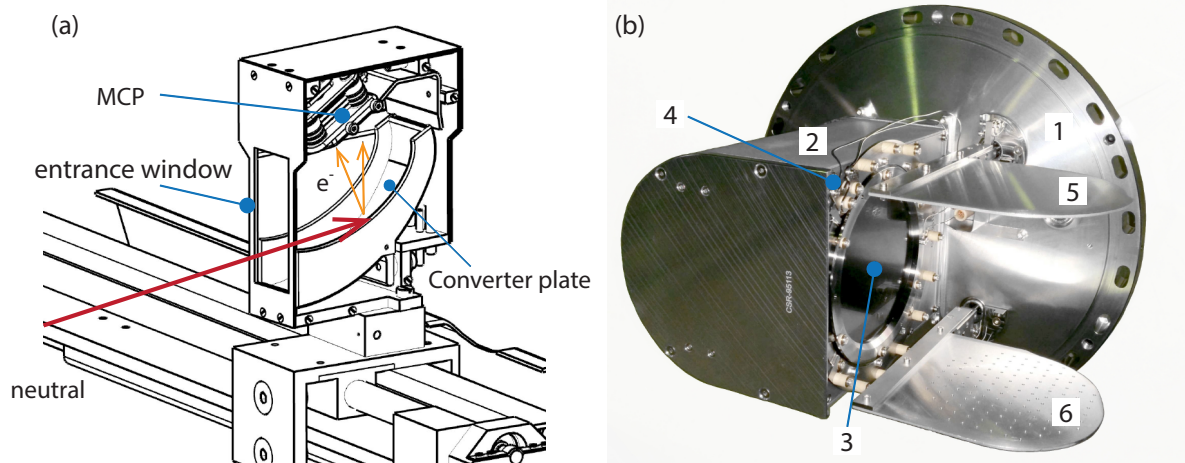
Figure 1.9: Particle detectors COMPACT (a) and NICE (b). At COMPACT the neutrals enter through the entrance window. On the converter plate a negative voltage is applied, in order to repell electrons. The neutrals impinge on the converter plate, where secondary electrons are produced. These electrons are then accelerated towards the MCP, where they are detected. COMPACT may be moved along the horizontal axis. NICE is mounted to the inner vacuum chamber (1). In comparison to the COMPACT MCP the NICE MCP (3) active area is much larger. Together with a MCP heating element (4), it is located within the detector housing (2). Electrons from the MCP are accelerated towards the phosphor screen (which is not shown in this figure). The light is then deflected by a mirror and detected by a high-speed camera. The MCP can be covered by a beam-shutter (5) or a calibration mask (6).

used for the present work.

The third straight section houses most of the beam diagnostic elements. Two capacitive current pick-up electrodes detect mirror charges of stored ions and were used for measuring absolute ion numbers in this work. There is also the Schottky-noise pick-up, designed for detecting a coasting beam, and two position pick-ups. The realization of the pick-up system is described thoroughly in Vogel 2016. There is two position pick-up electrodes in each of the straight sections, except for the electron cooler section.

Part I

Metastable states of Si$^-$ observed in a cryogenic storage ring

Chapter 2

Anionic states of Silicon

In this chapter the general properties of the negative states of silicon are discussed. A detailed overview of the level diagram, binding energies and lifetimes, as well as a brief introduction into the Multi-Configuration Dirac-Hartree-Fock (MCDHF) method are given. In the context of this work, new MCDHF calculations were carried out by the theory group at MPIK. Those results will be compared to lifetimes calculated in previous works of Andersson et al. 2006 and O'Malley and Beck 2003.

2.1 Metastable states of Si$^-$

Most elements in the periodic table form stable negative ions and have positive values for the electron affinity (EA). Since the outer electron is only loosely bound (see Sec. 1.1) electron configuration calculations, taking into account correlation effects, are crucial for the stability of many negative ions, and provide a sensitive test for many-electron theories.

Most of the information on negative ions has been obtained by negative ion spectroscopy. Here, the aim is to determine accurate binding energies (described in greater details in T. Andersen, Haugen, and Hotop 1999). Two basic methods are applicable in order to measure the bound-free photodetachment transition, where a photon γ hits an anion in an inital state $A^-(i)$ and photodetaches the extra electron e^- that will gain kinetic energy $\epsilon_{if\gamma}$, with the atom in a final state $A(f)$:

$$A^-(i) + \gamma \rightarrow A(f) + e^-(\epsilon_{if\gamma}) \tag{2.11}$$
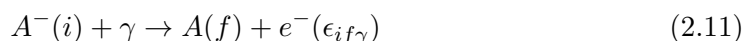
- By using photodetachment electron spectroscopy (PES) the energy of the pho-
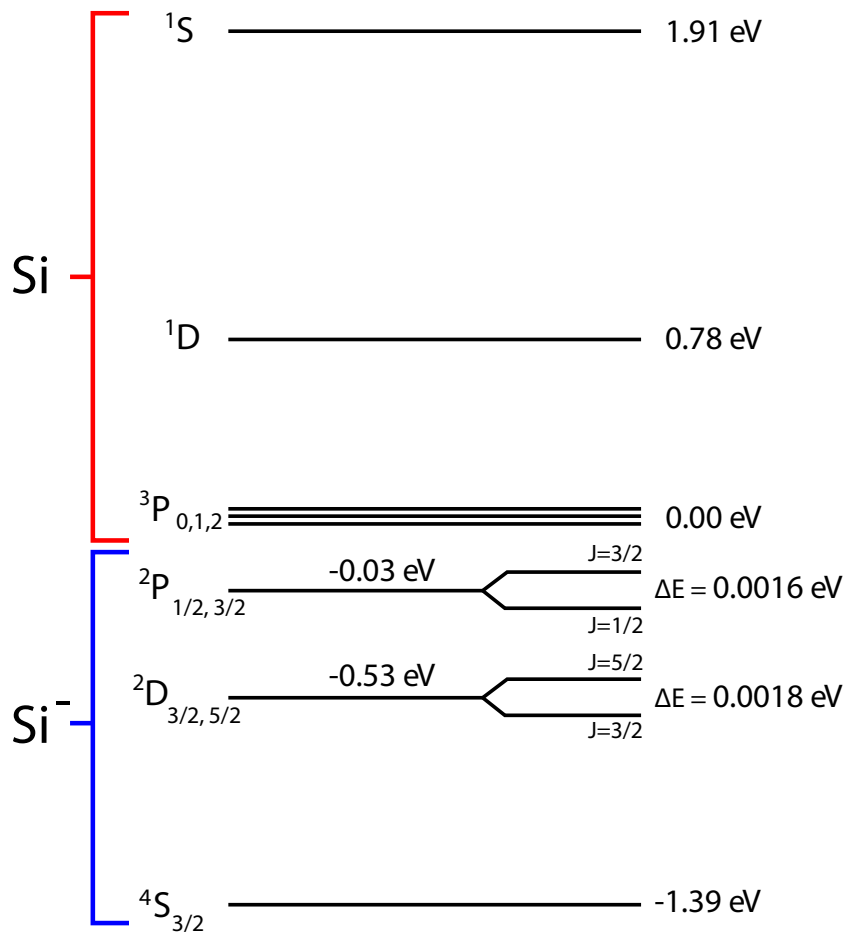
Figure 2.1: Level diagram of Si$^-$ with all the relevant neutral levels and the negative levels. The energies are given relative to the ^{3}P$_0$ state (energy axis not to scale). The values for ΔE were taken from Kasdan, Herbst, and Lineberger 1975 and Scheer et al. 1998.

todetached electron is measured at a fixed photon energy, where the photoelectron energy in its rest frame is given by:

$$\epsilon_{if\gamma} = E_\gamma - (E_f - E_i) \tag{2.12}$$

- laser photodetachment threshold spectroscopy (LPTS) is done by measuring the neutralized products in dependence of a tunable narrow band laser at threshold photon energies:

$$E_{if}^{THR} = h\nu_{if}^{THR} = E_f - E_i \tag{2.13}$$

Most information that we have on the state energies of Si$^-$ stems from these types of experiments. Si$^-$ has three electrons in the same, half-filled $3p$ orbital: $1s^2 2s^2 2p^6 3s^2 3p^3$. This results in a ^{4}S ground state with an EA of 1.39 eV as well as two doublet terms ^{2}D and ^{2}P. The level diagram is shown in Figure 2.1. First indications that show

metastable populations of the ^{2}D states were obtained by photodetachment measurements by Feldmann 1971. PES was used by Kasdan, Herbst, and Lineberger 1975 to measure the binding energies of (1.385 ± 0.005)eV for the ^{4}S and (0.523 ± 0.003)eV for ^{2}D state, respectively. It was also shown that the ^{2}P states were populated at a binding energy of (0.029 ± 0.005)eV, and from isoelectronic extrapolation the ^{2}P fine-structure splitting was estimated to be 1.6 meV. However, the energy resolution was limited to a few meV (Hotop and Lineberger 1975).

Higher accuracies are obtained by using LPTS. Scheer et al. 1998 measured neutralized negative ions as a function of the varied wavelength using a narrow band infrared laser. As a result, accuracies could be improved for the ^{2}D binding energies (0.527234 ± 0.000025)eV and (0.525489 ± 0.000020)eV for the $J = 3/2$ and $J = 5/2$ levels, respectively, resulting in a fine-structure splitting of $(1.75 \pm 0.02)10^{-3}$eV. The most accurate measurement for the ground state EA of Si has been achieved by photodetachment microscopy (described in Blondel et al. 2005), with the most recent result of $(1.3895210 \pm 0.0000007)$eV (Chaibi et al. 2010).

2.1.1 Previous work on negative state lifetimes of Si$^-$

Previous measurements on lifetimes of Si$^-$ and other negative ions were performed by Andersson et al. 2006 at the magnetic storage ring CRYRING. Using a probe laser to detect a neutral signal as a function of time after injecting the negative ions in the ring, lifetimes of metastable states that were bound with less than 1.17eV, which means excluding the ^{4}S ground state of Si$^-$, were performed. The CRYRING is a magnetic room temperature storage ring. CRYRING provided much higher gas densities (in comparison to the CSR), which limited the lifetimes of the stored ions due to collisions to 2.5 s. Furthermore, the authors attribute the measured photodetachment signal exclusively to the ^{2}D states and argued that the ^{2}P state of the silicon anions could not survive the source conditions and the black body radiation field of the storage ring. The limited storage time only allowed to infer a lower limit of > 1 min for the ^{2}D states.

In previous theoretical works, lifetimes for the ^{2}D states showed substantial differences for both $J = 5/2$ and $J = 3/2$. Employing relativistic configuration interaction calculations O'Malley and Beck 2003 inferred a lifetime of 27.3h for $J = 5/2$ states. Interestingly, a shorter lifetime for $J = 3/2$ of only 162s was calculated, attributed to a mixing with other states of the same J. Later on, MCDHF calculations by Andersson et al. 2006 have been carried out yielding different results. Lifetimes of 12h and 15h for the ^{2}D states were determined, which the authors believed to be more reliable, since the calculated binding energies agree better with the experimental results. Both calculations show a similar result for the ^{2}P$_{1/2}$ state. Unfortunately O'Malley and Beck 2003 did not publish a lifetime for the ^{2}P$_{3/2}$ state. Both theoretical results are shown in table 2.1. The measurement at CRYRING with the lower limit of > 1 min for the lifetime of the ^{2}D states, did not allow to resolve the discrepancy between these two theoretical predictions.

Table 2.1: Previous calculations of radiative lifetimes for the silicon anion. The calculations by O'Malley and Beck 2003 and Andersson et al. 2006 are shown.

State	O'Malley and Beck (2003) multi-configuration Hartree-Fock with relativistic corrections	Andersson et al. (2006) relativistic configuration interaction
$^2P_{3/2}$	-	25.1s
$^2P_{1/2}$	23.6s	28.1s
$^2D_{5/2}$	27.3h	12.2h
$^2D_{3/2}$	162s	14.5h

2.2 Theoretical calculations on the anionic structure

New calculations were carried out for a better understanding of the experimental results. These calculations include the Multi-Configuration Dirac-Hartree-Fock (MCDHF) method, which is briefly intoduced in the following section.

2.2.1 Hartree-Fock Method

The Hartree-Fock (HF) (Hartree 1928) method is one approach to approximate solutions for the Schrödinger equation of a multi-electron system. In the context of this approximation, the movement of an electron is no longer affected by interaction with other electrons, but is considered affected by a mean field generated by the other electrons. D. Hartree described the solution of the Schrödinger equation by a product of the orbitals of all available electronic states:

$$\Psi_{EL} = \psi_1 \psi_2 ... \psi_N = \prod_{i=1}^{n} \psi_i(i). \tag{2.14}$$

However, this simple product does not include the general antisymmetry postulate. With the addition of the Pauli principle that implies that two electrons cannot be identical in all quantum numbers, the n-electron antisymmetric product wavefunction Ψ (so-called Slater determinant) is given by

$$\Psi = \frac{1}{\sqrt{N!}} \begin{vmatrix} \psi_1(1) & \psi_2(1) & \cdots & \psi_N(1) \\ \psi_1(2) & \psi_2(2) & \cdots & \psi_N(2) \\ \vdots & \vdots & \ddots & \vdots \\ \psi_1(N) & \psi_2(N) & \cdots & \psi_N(N) \end{vmatrix}. \tag{2.15}$$

The columns are assigned to the orbitals and the rows are assigned to the coordinates of the electrons. Knowing the basic properties of determinants one can infer:

- Swapping two rows (which is identical to swapping two electrons) leads to change of sign, thus the antisymmetry principle is fulfilled

- If two columns of a determinant are equal, its value is 0, meaning two electrons are in the same orbital, the wavefunction cannot be normalized anymore. Hence the Pauli principle is also fulfilled.

The HF equations are a set of coupled, nonlinear Schrödinger equations for each of the single particle states. The eigenvalues are obtained using the variational principle, where for any choice of Ψ, the expected energy $<\Psi|\hat{H}|\Psi>$ is an upper limit to the ground state energy of H. The best approximation to the ground state is obtained by minimization of the energy expectation of some set of functions in which Ψ is constrained.

2.2.2 Configuration Interaction

Another approach to solve the Hamilton operator for the Schrödinger equations for a multi-electron system is by using the Configuration Interaction (CI) method (Sherrill and Schaefer 1999). In comparison to the HF-Method, it also takes into account electron correlation effects by using more than one configuration and having electrons put in different orbitals, which allows for spatial correlation of the electron motion. Therefore, the trial wavefunction Ψ_i is given by a linear combination of configurations ψ_i, weighted with a mixing coefficient c_i

$$\Psi_i = \sum_{i=1}^{n} c_i \psi_i \tag{2.16}$$

A lot of ab-initio codes are based on CI to infer the structure of atoms and ions. Again the variational principle is used in order to optimize the mixing coefficients c_i. High accuracy is achieved by adding more configurations.

2.2.3 Multi-Configuration Dirac Hartree-Fock

The MCDHF method is a combination of the already introduced CI and HF methods. In this case the wavefunctions are given by a set of configurations that are represented by Slater determinants and correspondingly weighted by mixing coefficients. For this approach both the set of configurations and the mixing coefficients are optimized. In comparison to Multi-Configuration Hartree Fock (MCHF), MCDHF also contains the relativistic formalism of the electron motions. Following the scheme, the wave functions of the many-electron atomic states, the so-called atomic state functions (ASFs), are linear combinations of configuration state functions (CSFs) with total angular momentum J, magnetic M and parity P quantum numbers. From this follows the wavefunction

$$|\Psi PJM> = \sum_{k} c_k |\psi PJM>. \tag{2.17}$$

$|\psi P J M>$ CSFs are constructed as jj-coupled (where the angular momenta and spins of each electron couples to a total angular momentum) Slater determinants of one electron orbitals, while Ψ_k summarizes all the remaining information for defining the CSFs, such as orbital occupation and angular momenta of single electrons.

2.2.4 Updated Comparison of various theoretical calculations

The basic aspects of the MCDHF method as it was used in Müll et al. 2021 are introduced in this chapter. The calculations were carried out by the theory group (Ionic Quantum Dynamics and High-Precision Theory group at Max Planck Institute for Nuclear Physics) using the code from Froese Fischer et al. 2019, in combination with relativistic configuration (RCI) interaction, which includes corrections regarding the Breit interaction and approximate quantum electrodynamics terms. The results will be compared to other theoretical calculations and to the measurement.

With the outermost electron being only weakly bound to the atom, ASFs have to be expanded in a large CSFs basis in order to account for the electron correlation precisely. As described in Müll et al. 2021, two schemes are applied for the calculations. For the first scheme the set of CSFs is created by single and double excitation (SD) from electrons in the $3s^2 3p^3$ valence orbital to high lying virtual orbitals. Included are the most relevant triple and quadruple excitations by SD from the $\{3s^2 3p^3, 3s 3p^3 3d, 3s^2 3p 3d^2, 3p^3 3d^2, 3s 3p^3 4s, 3s^2 3p 4s^2, 3s^2 3p^2 4p, 3s^2 3p 4p^2, 3s 3p^3 4d,$ $4s^2 3p 4d^2\}$ multi-reference configurations.

Lifetimes and binding energies were monitored via layer-by-layer expansion and optimizing of the active space of virtual orbital from the $3d$ up to the $10l$ subshell. After having generated 3478527 CSFs for the total angular momentum $J = 1/2, 3/2, 5/2$ the resulting excited energies of the ^{2}D and ^{2}P states deviated by 1.8% from the experimental values given in Scheer et al. 1998. Now for the second scheme the full triple excitation from the $3s^2 3p^3$ configuration up to $9l$, as well as the full quadruple excitation from the earlier multi-reference configurations up to the $5f$ are included. 7327283 CSFs are generated yielding excited state energies of 0.869 17 eV and 0.870 88 eV for the ^{2}D$_{3/2}$ and ^{2}D$_{5/2}$ state, respectively, and 1.369 03 eV and 1.372 90 eV for the ^{2}P$_{1/2}$ and ^{2}P$_{3/2}$ states, respectively. They agree within 0.9% with the experimental values of Scheer et al. 1998. Although the 3.87 meV fine-structure splitting for the ^{2}P has not been measured yet, the calculated value for the fine-structure splitting of the ^{2}D state (1.745 ± 0.025)meV is close to the experimental value in Scheer et al. 1998. Also the binding energies of the [Ne] $3s^2 3p^2$ ^{3}P$_{0,1,2}$,^{1}D$_2$ and ^{1}S$_0$ states for the neutral Si have been calculated, using the first scheme. There 602646 CSFs have been generated for $J = 0, 1, 2, 3, 4$ from $\{3s^2 3p^2, 3s^2 3p^2, 3s 3p^2 3d, 3s^2 3d^2, 3p^2 3d^2, 3s 3p^2 4s, 3p^2 4s^2, 3s^2 4p^2, 3s^2 3p 4p, 3s 3p^2 4d,$ $3s^2 4d^2\}$ multi-reference configuration. The resulting EA is 1.395eV for the ^{4}S$_{3/2}$ ground state of Si$^-$, which agrees within 0.4% with the experimental value in Chaibi et al. 2010.

Since ^{2}D and ^{2}P decay by magnetic dipole $M1$ and electric quadrupole $E2$ transitions, those two states are metastable with a rather long lifetime. Applying the first MCDHF-

Table 2.2: Theoretical radiative lifetimes for the silicon anion. The MCDHF-RCI method was used to calculate the lifetimes and previous values from O'Malley and Beck 2003 and Andersson et al. 2006 are given.

State	present work	O'Malley and Beck (2003)	Andersson et al. (2006)
$^2P_{3/2}$	(20.6 ± 1.6)s	-	25.1s
$^2P_{1/2}$	(22.1 ± 1.5)s	23.6s	28.1s
$^2D_{5/2}$	(9.6 ± 0.7)h	27.3h	12.2h
$^2D_{3/2}$	(11.9 ± 0.8)h	162s	14.5h

RCI scheme, the calculated lifetimes are (11.9 ± 0.8)h and (9.6 ± 0.7)h for the $^2D_{3/2}$ and $^2D_{5/2}$ state, respectively, and (22.1 ± 1.5)s and (20.6 ± 1.6)s for the $^2P_{3/2}$ and $^2P_{1/2}$ state. The results are shown together with the previous calculations in Table 2.2.

2.2.5 Calculating photodetachment cross sections

In order to support the analysis of the experimental data, calculations on the photodetachment cross section of the anionic states of Si$^-$ have been carried out for two specific photon wavelengths, namely 1390 nm and 635 nm. The choice of the wavelength is motivated by the two continuous wave laser systems that were used for our measurements on long-lived state lifetimes. The cross sections are used to estimate the laser depletion time scales for long exposure (see Section 4.3).

So far, all the calculations describing the neutral and negatively charged Si have been using the functions generated with the MCDHF-RCI method. For modeling photodetachment paths the grasp2K (Jönsson et al. 2007) and RATIP (Fritzsche 2012) codes have been applied. The grasp2K is based on MCDHF and higher-order corrections (see Grant et al. 1980) and is an updated version of the grasp92 (Dyall et al. 1989) code (general-purpose relativistic atomic structure program). The RATIP (program for relativistic calculations of atomic transistion, ionization and recombination properties) is an updated version of the grasp2k and grasp92 code. The basic concept of those codes is to combine different atomic bound-state wave functions for different levels and charge states with continuum orbitals, in order to calculate many-electron transition amplitudes and other properties that follow from those. Three main types of transition amplitudes can be classified:

1 electron-electron interaction (based on the Dirac-Coulomb-Breit Hamiltonian)

2 electron-photon interaction with the coupling of the atoms to a radiation field

3 electron-nucleus interaction because of electric and magnetic multipole fields of the nucleus (hyperfine)

The calculations for the photodetachment cross sections have been carried out for the two experimentally relevant wavelengths at 1390 nm and 635 nm, which can be found

in Table 2.3. From the invariance in different gauges, an uncertainty of 50% for the calculations is inferred.

Table 2.3: Calculated photodetachment cross section σ_{pd} in units of megabarn (10^{-18}cm^2) for the Si$^-$ states at two laser wavelengths: 1390 nm (0.89 eV) and 635 nm (1.95 eV).

Transition	σ_{pd} (1390 nm $\simeq$ 0.89 eV)	σ_{pd} (635 nm $\simeq$ 1.95 eV)
$^4S_{3/2} \to {}^3P_0$	-	1.47
$\to {}^3P_1$	-	2.58
$\to {}^3P_2$	-	3.90
$^2D_{3/2} \to {}^3P_0$	1.17	0.85
$\to {}^3P_1$	3.05	2.27
$\to {}^3P_2$	0.36	0.45
$\to {}^1D_2$	-	4.68
$^2D_{5/2} \to {}^3P_0$	1.0×10^{-5}	9.4×10^{-5}
$\to {}^3P_1$	0.23	0.59
$\to {}^3P_2$	2.42	2.26
$\to {}^1D_2$	-	2.13
$^2P_{1/2} \to {}^3P_0$	0.55	0.94
$\to {}^3P_1$	1.68	2.07
$\to {}^3P_2$	1.08	1.64
$\to {}^1D_2$	2.00	3.38
$\to {}^1S_0$	-	7.04
$^3P_{3/2} \to {}^3P_0$	0.09	0.15
$\to {}^3P_1$	0.54	0.91
$\to {}^3P_2$	1.67	2.25
$\to {}^1D_2$	1.24	2.58
$\to {}^1S_0$	-	6.98

Chapter 3

Photodetachment setup

Experiments of the metastable states on Si$^-$ require a low blackbody radiation field in order to not detach the weakly bound ^{2}P states, and long storage times in order to follow the decay of the ^{2}D states in the photodetachment signal.

In this chapter an overview of the experimental setup is given, with a focus on the laser-ion interaction section. Two beamtimes have been performed on the Si$^-$ system. The first beamtime took place in 2015 before I even was part of the Cryogenic Storage Ring (CSR) team. In this beamtime first data on Si$^-$ has been taken, which have been analyzed by me. Afterwards there were still open questions, which have been adressed in a second beamtime, where I have been part of, in 2018. In between both beam times, there have been significant experimental upgrades, such as the implementation of the electron cooler, which is placed in the same straight section of Cryogenic Storage Ring (CSR) as the laser setup. Therefore, the position of the laser mirrors inside the experimental vacuum chambers had to be adjusted and both configurations will be described in the following section.

3.1 Laser Setup

In order to photodetach the outer electron, the stored ions are overlapped with a laser beam entering and leaving the experimental vacuum chambers through two sets of sapphire viewports. Sapphire viewports were chosen because they withstand a large temperature range from cryogenic 2 K up to baking temperatures of 500 K and they have sufficient heat conductivity. Furthermore, 300 K radiation has its highest power density at around 8000 nm, hence sapphire was chosen with a wavelength transmission from 200 nm to 6000 nm, which helps minimizing 300 K blackbody radiation. The laser
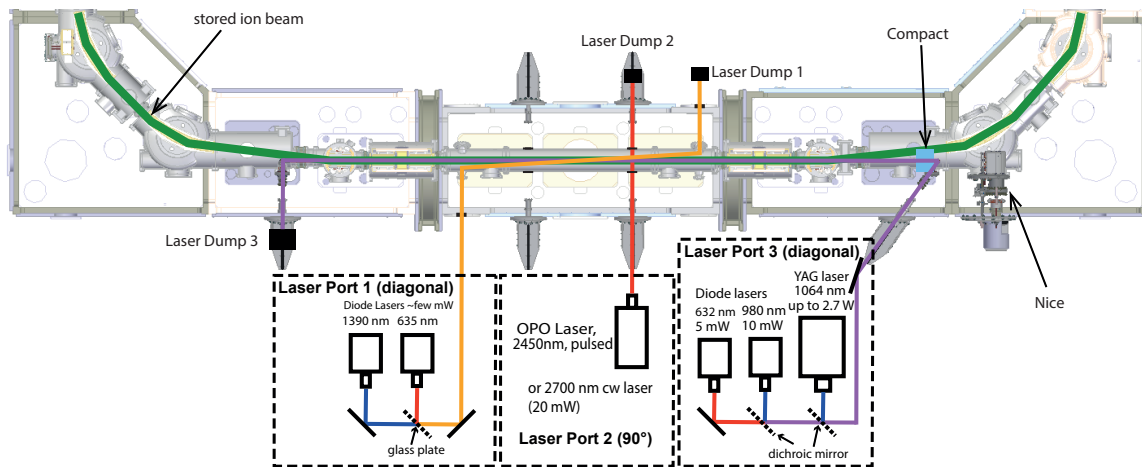
Figure 3.1: Schematic of the laser interaction section at the CSR and the experimental setup (not to scale). The ion trajectory is displayed by a solid green line and the insets show simplified sketches of the optical setups (not all optical elements are shown). Neutralized particles were counted by Cold Movable Particle Counter (Compact).

mirrors inside the CSR are used to guide the laser beam through the experimental vacuum chamber.

Various continuous wave lasers and a pulsed Optical Parametric Oscillator (OPO) were coupled into the storage ring at different viewports. The straight section used for laser experiments, a simplified sketch of the laser setup, as well as the particle detectors used to count neutralization events are shown in Fig. 3.1. Missing in this figure are the electron cooler setup and the extraction section, which were also not implemented during the first part of the measurement campaign on Si$^-$. Laser port 1 shows the laser setup for the first beamtime with a diagonal laser-ion overlap at a grazing angle of 3.4° (described in detail in Christian Meyer 2018). The detailed technical drawing of laser port 1 is shown in Fig. 3.2.

Laser port 3 offers a diagonal laser-ion overlap at a grazing angle of 1.1° and was implemented since the existing laser path had to be modified in order to allow the implementation of the electron cooler. A detailed technical drawing of laser port 3 is shown in Fig. 3.3. The laser beams have to pass through the viewports and several cryogenic shield layers to enter the experimental vacuum, and their path is more complex than it can be shown in this figure. After transmission through CSR the remaining laser power was recorded multiple times. The lasers and part of the optics are mounted on an optical table close to the CSR. Inside the experimental vacuum chambers, there are two broadband mirrors with a dielectric coating that reflect wavelengths from 300 nm to 2000 nm. For longer wavelengths the crossed beam configuration at laser port 2 (90°) needs to be used. A diagonal path allows for a larger overlap between ion and laser beam. Thus, the diagonal laser path was chosen whenever possible.

For all of the laser beams, telescopes using pairs of lenses were set up such that there
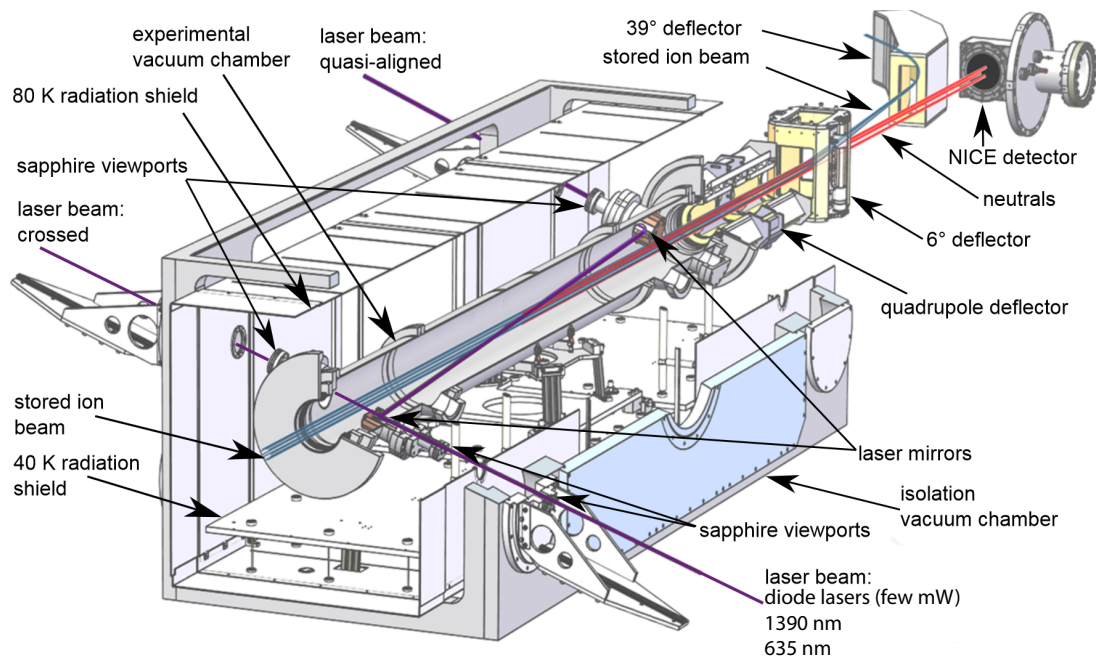
Figure 3.2: Technical drawing of the laser-ion interaction section for the laser port 1 config-
uration. The neutrals are detected at the NICE detector while the ions are kept
on their trajectory by the ion optical elements. The laser beams enter and exit
the experimental vaccum chamber by sapphire view ports. The surroundings of the
experimental vacuum chambers are shown (40 K, 80 K radiation shields and the iso-
lation vacuum chamber). (This figure was taken from the dissertation of Christian
Meyer 2018)

was no focus in the interaction region. Inside of the CSR, the laser beam diameters
were $> 5\,\text{mm}$ ($> 0.2\,\text{cm}^2$). Taking the highest power $P = 10\,\text{mW}$ of the probing lasers
results in intensity levels of $< 0.05\,\frac{\text{W}}{\text{cm}^2}$. For the pulsed OPO, the pulse energy at
2450 nm (recorded right before CSR) was $5\,\mu\text{J}$, resulting in an intensity of $< 10^4\,\frac{\text{W}}{\text{cm}^2}$.
This intensity is still a factor of 10^3 lower than the intensity at which two-photon
processes are strongly suppressed. Thus, two-photon processes will be ignored (Scheer
et al. 1998).

stored ion beam

39° deflector

isolation vacuum
chamber

6° deflector

quadrupole deflector

sapphire viewport

laser mirror

40 K radiation shield

80 K radiation shield

crossed beam laser path

sapphire viewport

crossed beam laser path

quadrupole deflector

6° deflector

experimental vacuum chamber

39° deflector

quasi-aligned laser beam

laser mirror

NICE detector

Figure 3.3: Technical drawing of the laser-ion interaction section for the laser port 3 configuration. The stored ion beam (blue) and the electrostatic elements (6° and 39° deflectors and the quadrupole deflectors) are shown. The laser beam (red) is quasi-aligend with the ions at an angle of 1.1° and the neutrals are collected at the NICE detector. Also shown are parts of the electron cooler upgrade.

Chapter 4

Experimental Results

In this chapter the results from both beam time campaigns will be presented. From the first data set a lower limit for the ^{2}D states will be introduced. Those results will also be compared to theoretical calculations by Andersson et al. 2006 and O'Malley and Beck 2003 as well as the most recent calculations performed in the group of Zoltan Harman at our institute. Furthermore, the dependence of the photodetachment signal on the number of stored ions will be shown. Employing the depletion measurements from the second data set, the fractions of ions in a metastable state will be estimated. The measurements using the pulsed OPO laser revealed the lifetime of the ^{2}P state. The analysis in Müll et al. 2021 is based on this chapter.

4.1 Timing Scheme

For the purpose of following the time dependence of the photodetachment signal of the Si$^-$ ions, a timing scheme for the CW lasers was developed (in the course of this thesis), which is presented in detail in this section. The timing scheme for one injection cycle is displayed in figure 4.1. The idea is to record signals versus background contributions, which is realized by switching the lasers on and off by generating digital outputs using a LabVIEW NI PCIe-6612 card. The pattern can be chosen by tuning the values *delay 1, delay 2, width 1, width 2, and period 1, period 2*. In principal, one can extend the amount of lasers being switched by this program, but for this beamtime only up to three lasers were switched. The injection cycle, shown in Fig. 4.1, starts with the request pulse sent to a timing generator called attaclock (main timing generator of the CSR) that controls the storage ring injection. After around 50 ms, the injection confirmation pulse is sent and triggers all of the following lines. A fast switched pair of electrodes (in
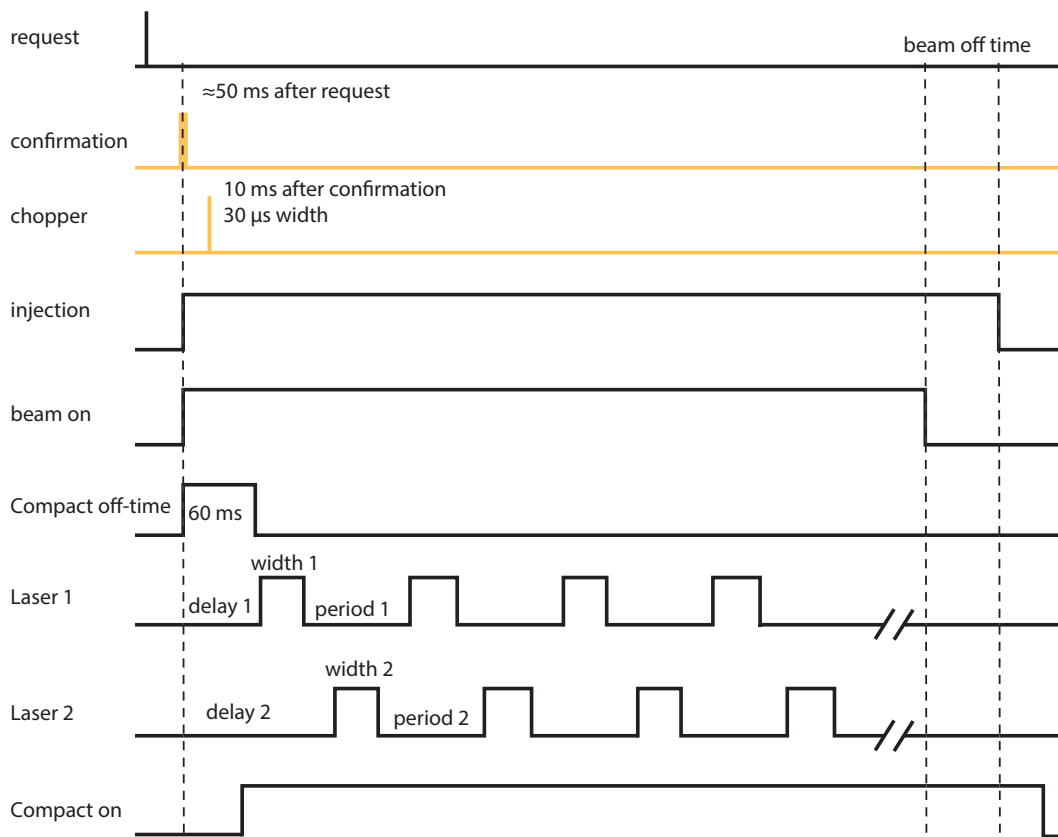
Figure 4.1: Timing scheme for the CW lasers. The black lines indicate timing generated by the data acquisition PC and the orange lines indicate timing generated by the attaclock (main timing generator of the CSR).

the injection beamline) called chopper allows the ions for $30\,\mu$s to pass by, $10\,$ms after the confirmation pulse. Injection and beam-on-phase start as soon as the confirmation pulse is sent. The off-time of the COMPACT detector is used to avoid high count rates, which would be generated in the first revolutions of the stored ions. Additionally, the off-time at the start of every injection is used to avoid the *injection flash* (electronic noise of switching from the first 6° deflector). For the measurements that are presented here, the patterns of both lasers had the same frequency and width. In order to extract the count rate caused only by collisional detachment, a time gap between the on-phases of the two lasers was established. During the beam-off-time (which is usually set up to approximately 10% of the storage time) counts without ions in the ring are recorded. This time window is used to calculate the dark count rate for every injection and is subtracted from the events during the beam-on-phase in the analysis later on. The counts are recorded for a predefined bin together with a flag which indicates the status of each laser during that bin. Typical time scales for laser windows were on the order of $1\,$s. Therefore a time binning of $100\,$ms was chosen to over-sample one laser step.

4.2 Low background measurements: Overview

During the first measurement campaign, which was set up as a test beamtime on the Si anion, two CW lasers were used: a 635 nm (1.95 eV) visible laser (Vis), which is able to detach all metastable states of Si$^-$ as well as the ground state, and a 1390 nm (0.89 eV) infrared laser (IR) that is only detaching the excited ^{2}D and ^{2}P states. Since it was expected that only a small fraction of the Si$^-$ beam would consist of metastable state population, the power of the IR laser was chosen much higher than for the Vis laser. Around 15 mW from the IR light were sent into CSR. Since the measurement was done at the end of the first cold period that lasted several months, a thin layer of ice had been accumulated on the laser windows inside the CSR (the viewports have been upgraded to prevent such effects after this beam time). The transmission of the IR laser power through the four viewports of the CSR was found to be less than one percent. Therefore, we estimate an effective laser power of 1 mW at the ion-photon interaction region. The intensity of the Vis laser was chosen to be much lower (4 mW), because it was expected that most Si$^-$ ions populate the ground state. As we used a glass plate to merge both laser beams, only 0.5 mW of Vis light was sent towards CSR. It is attenuated even more than IR light, which led to a not precisely measurable power level at the exit port. Switching the lasers with the following pattern: [1s IR - 1s lasers off - 1s Vis - 1s lasers off] results in a total cycle length of 4s. Hence the duty cycle is $D = 1/4$ for both lasers.

The analyzed data for the observed laser signals is represented in Fig. 4.2. Neutralized Si atoms were counted on the downstream COMPACT detector. For the analysis, total counts and the measured time for each bin were summed up for all injections. Count rate versus storage time is shown with a time bin width of 4 s . The error bars are given by the standard deviation σ of the accumulated counts, calculated by taking the square root of the accumulated counts (using Poisson statistics) in the corresponding time bin. For presentation reasons the error bars are not shown. Figure 4.2 depicts the neutral count rates for both lasers (upper panel) and the rate during the laser-off phases (lower panel). The data consists of 18 consecutive injections, which corresponds to a total data taking time of 13 h.

The count rates detected in the laser-off-phases arise because of collisional detachment, on top of a constant detector noise level. From the initial collisional background rate the residual gas density is calculated to $n_{rg1} = 130^{+260}_{-70}$cm^{-3} (a detailed explanation and the corresponding equation 4.29 is given in Sec. 4.6). Furthermore, the mean free path $\lambda = 1/(n_{rg}\sigma_{cd})$ is calculated. The beam lifetime due to collisional detachment is given by $\tau_{coll} = \lambda/v = 1.7 \cdot 10^5$s ($v$ denotes the velocity of the Si$^-$ ions). This large value clearly shows that collisional detachment has no significant impact on the observed lifetimes at these low background measurements conducted in the first measurement campaign.

The data is fitted by a sum of three exponential functions and a constant offset:
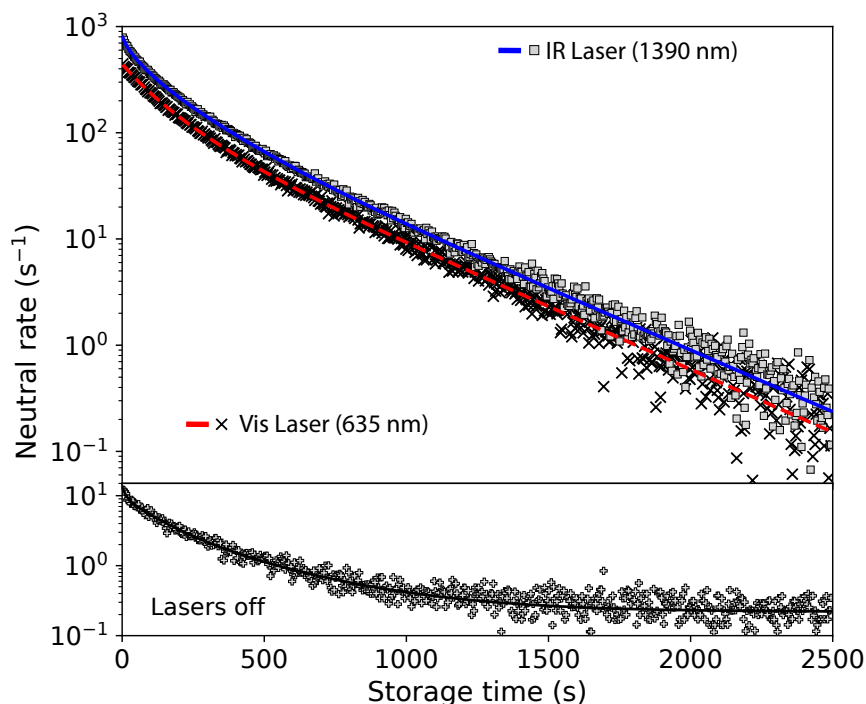
Figure 4.2: Neutral count rates induced by the merged laser beams versus storage time in the first beamtime. The crossed points are events induced by the Vis laser and squared ones by the IR laser. The red and blue lines are exponential fits to the respective data sets and on the lower panel the events during the lasers off phases are shown.

$$R(t) = \sum_{i=1}^{3} A_i e^{-t/\tau_i} + c_{dark} \tag{4.18}$$

The value of $c_{dark} = 0.219(7)\,\mathrm{s}^{-1}$ is given by the detector dark counts. Amplitudes and lifetimes for the laser-off-phase are given in table 4.1. In order to display the laser induced count rates, the counts after a laser-off step were subtracted from the counts in the laser-on step.

The photodetachment rates for both lasers look very similar. Even though the IR laser exclusively detaches the excited Si$^-$ states only, it basically follows the course of the Vis laser that includes photodetachment of the ground state. Although the intensity of the Vis laser is likely to be a factor of 50-100 lower than for the IR laser, the IR/Vis rate ratio is only $\approx$1.5. With the calculated photodetachment cross section (from 2.3) of the ^{4}S ground state being slightly higher, in comparison to the cross section of the ^{2}D states with the IR laser, this ratio already suggests that the population of metastable sates is in the percent range (depletion measurements shown in section 4.7 will affirm this result).

Appropriate fits to the data are achieved by using a sum of four exponentials for the IR laser, while for the Vis laser the fit does not improve using more than three

Table 4.1: Fit parameters for multi-exponential regression shown in Fig. 4.2. The number of injected ions was $N_{ion} = 2.9 \times 10^8$.

Lasers	τ_1 (s)	A_1 (s^{-1})	τ_2 (s)	A_2 (s^{-1})	τ_3 (s)	A_3 (s^{-1})	τ_4 (s)	A_4 (s^{-1})
off	351±30	3.4±0.7	123±17	5.8±0.5	14.0±4.6	3.8±0.7	-	-
Vis	367.2±5.0	137.1±7.4	150±12	221±27	64±13	87±31	-	-
IR	375.1±5.5	185±12	172±10	318±18	58.8±8.0	218±18	11.0±3.0	96±17

exponential functions. The most significant difference between the two signals is the steeper decay for the IR laser, having an additional short lifetime component of about 11 s. The remaining three components with lifetimes of around 60 s, 160 s and 370 s are identical for both lasers within the errorbars. Therefore those signals are most likely not representing metastable lifetimes, but beam intensity decay, which will be explained in the following section.

4.3 Dependence of the photodetachment signal on the number of stored ions

Having the measurement from the previous section with an injected ion number $N_{ion} = 2.9 \cdot 10^8$, the effect of increasing or reducing the ion number by a factor of 3 has also been studied. Using a variable aperture in the transfer beamline towards the CSR, the current of the ion beam could be tuned without changing the ion source settings. Beam emittance might also be changed by this procedure, however the effect on the initial storage conditions is negligible, as the CSR acceptance is much larger than the maximum emittance possible within the geometry of the transfer beamline. The results are depicted in Fig. 4.3.

Detaching all Si$^-$ states with the Vis laser gives a much steeper initial decay in the observed signal with higher numbers of injected ions. Again exponential fits have been applied and the amplitudes A_i^N (normalized to unity for better comparison) and lifetimes τ_i are listed in Table 4.2. For higher numbers of stored ions N_{ion} three exponential functions were needed for a reasonable fit, while for the low ion number two exponentials were applied. The short component with a lifetime of around 60 s in those three cases is strongly dependent on the number of ions. For the fit of the lowest ion numbers this lifetime component is not visible. Consequently, we attribute this short lifetime to storage ring effects, which get stronger with higher N_{ion}. The effect of the ion numbers with regards to the longer lifetimes of around 150 s and 370 s shows a weaker dependence.

Table 4.2: Fit parameters different ion numbers shown in Fig. 4.3. The number of injected ions was $N_{ion} = 2.9 \cdot 10^8$.

N_{ion}	τ_1	A_1^N	τ_2	A_2^N	τ_3	A_3^N
$7.4 \cdot 10^8$	380.6	0.11	175.7	0.33	69.6	0.57
$2.9 \cdot 10^8$	367.2	0.30	149.9	0.50	64.0	0.20
$9.4 \cdot 10^7$	367.9	0.46	128.9	0.54	-	-

In principle, one would expect that the decreasing number of ions in the storage ring over time can be described by a single exponential decay function, in case that the chosen ion species has only one bound state and if there is a uniform loss mechanism, independent of the number of ions and the ion orbit. If that is the case, the inverse of the decay constant (characteristic for the beam loss process) is the beam lifetime. In fact, there are often effects that disturb this simple case and a single exponential is found rarely. Some of the effects that lead to deviations from a single exponential are easy to explain and also to discriminate against. The best example is the initial high count rates on the detector after storing the ions, which is attributed to ions being at trajectories that are not compatible with a stable ion orbit. Furthermore, there is the effect of space charge limitations and intrabeam scattering, which is related to injecting large number of ions, and which has been demonstrated in this section. This effect is typically observable for up to several tens of seconds. Another effect that has been observed in CSR (von Hahn et al. 2016), are diffusive momentum changes on the timescale of the long storage times. The increased ion momentum spread is believed to be the main reason for beam loss. Noise on the electric dipoles that are used to guide the ion beam (which is independent of N_{ion}) and ion-ion collisons or ion-beam space charge (which are both dependent on the ion number) might be the reason for beam diffusion. While we do not understand the lifetimes in detail, having a two component exponential lifetime even at lower numbers of injection ions, indicates that there are at least two independent loss processes.

4.4 Signal at long storage times: Lower lifetime limit for the ^{2}D states

Interestingly, overall the signal for both lasers in Fig. 4.2 shows a very similar course, except for the short storage times. Having a signal from the IR laser at times $> 2000\,\text{s}$ shows that there has to be at least one very long lived metastable state. In order to get an idea of the lower limit of this long lived state, the decay constants from both laser
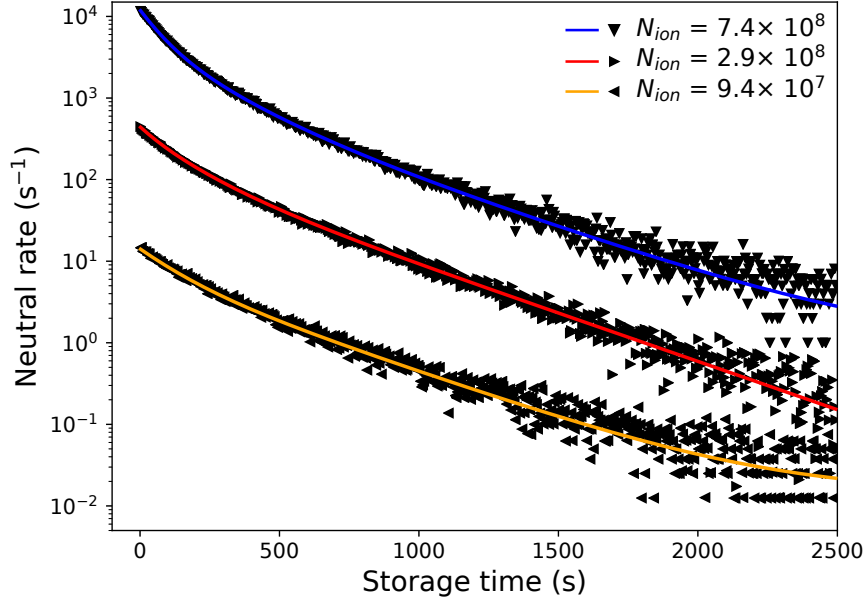
Figure 4.3: Photodetachment signals obtained using the Vis laser for three runs with different average numbers of injected ions. The upper and lower curve have both been shifted by multiplying them with a factor of 10 and 0.1, respectively. The fit parameters are given in table 4.2

signals (see Fig. 4.4) are compared at long storage times (t > 800 s). On this timescale a single exponential fit is enough to reproduce the data for both laser signals, giving lifetimes of (360 ± 2.4)s for the IR and (358.4 ± 3.0)s for the Vis laser. Within the error bars, those lifetimes are the same.

Although the IR laser intensity is much higher, the photodetachment signal from the Vis laser is stronger and is likely to be dominated by the negative ground state (additional measurements supporting this assumption will be given in the section 4.7). Hence, this signal is also independent on changes in the state populations of the stored ion beam. Because of this the decay constant is likely to show the intrinsic lifetime of the stored ions. With this assumption, a lower limit for the metastable states being probed by the IR laser can be derived from the fitted decay constants.

In order to simplify the estimation, only two states are assumed to be populated, the ground state population N_g and the excited state population N_e, with the corresponding decay constant k_r. The total number of ions after 800 s is N and the fraction of excited ions is η. The population of the excited state is described by

$$N_e = \eta N e^{-(k_r+k_{beam})t} \tag{4.19}$$

and the population of the ground state is given by

$$N_e = N e^{-k_{beam}t} - \eta N e^{(k_r+k_{beam})t} \tag{4.20}$$
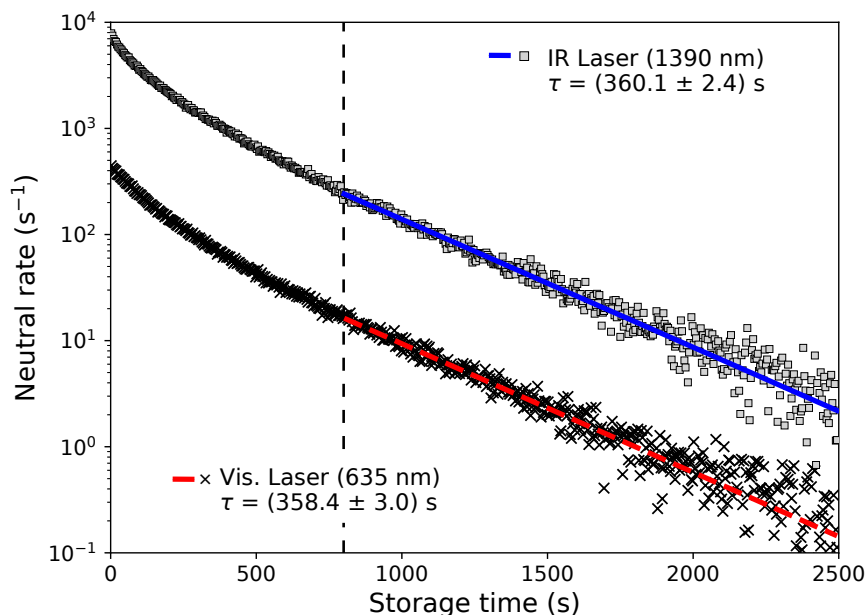
Figure 4.4: Photodetachment signals of the Vis laser (black dots) and of the IR laser (black circles) at long storage times $> 800\,\text{s}$. The red and blue line are single exponential fits to the respective laser signal. The IR signal has been multiplied by a factor of 10.

This set of equations is only applicable if the beam lifetime k_{beam} is matching for the ground and excited state. This assumption makes sense since collisional detachment happens so rarely that storage times are not limited. The main loss mechanism is an increase in the momentum spread of the stored ions, leading to a limitation in beam lifetime as shown in von Hahn et al. 2016. Thus the beam loss rate does not depend on the internal state of the stored ions. The rates during the laser-on-phases are linked to the population:

$$R_{IR} = f_e^{IR} N_e(t) \tag{4.21}$$

$$R_{Vis} = f_g^{Vis} N_g(t) + f_e^{Vis} N_e(t) \tag{4.22}$$

with f_e^{IR}, f_g^{Vis} and f_e^{Vis} being constants accounting for laser-ion interaction. They cover photon intensities in the interaction region, geometric overlap between laser and ion beam, and the photodetachment cross section of the excited states and the ground state for the specific wavelength, and are assumed to be constant in time. In the following the model count rates are compared with the observed rates after $800\,\text{s}$ from Fig. 4.4. For the Vis laser the measured rates fit very well using a single exponential fit, although the model shows two decay constants. This is due to most of the ions after $800\,\text{s}$ of storage time being in the ground state leading to a $\eta \ll 1$. From the photodetachment cross section calculations in table 2.3, we find that the excited states

do not have a very large photodetachment cross section at the wavelength of the Vis laser, which otherwise could dominate the observed photodetachment signal. Therefore $\eta f_e^{Vis} \ll f_g^{Vis}$ is assumed, which leads to a simplified rate for the Vis laser:

$$R_{Vis} = f_g^{Vis} N e^{-k_{Vis}t} \tag{4.23}$$

and the decay constant of the Vis laser giving the beam decay $k_{Vis} = k_{beam}$. The beam lifetime is then given by the fit $\tau_{vis} = \tau_{beam} = 1/k_{beam} = 358.4(30)\,\text{s}$ and for the rate of the IR laser follows:

$$R_{IR} = f_e^{IR} \eta N e^{-(k_r + k_{beam})t}. \tag{4.24}$$

The fit from the IR signal gives $\tau_{IR} = 1/(k_r + k_{beam}) = 360.1(24)\,\text{s}$. Now the radiative decay constant is

$$k_r = k_{IR} - k_{beam} = (-1.32 \pm 2.98) \cdot 10^{-5}\text{s}^{-1}. \tag{4.25}$$

The radiative decay constant k_r is compatible with zero. Using prominent examples from Nishino et al. 2009 (for giving a lower limit for the lifetime of proton decay) and Cairncross et al. 2017 (upper bound of the electron electric dipole moment), a confidence level of 90 % is chosen (1.645σ of k_r) to estimate the lower limit of $k_r < 4.9 \cdot 10^{-5}\text{s}^{-1}$. This results in a lower limit for the radiative lifetime of the metastable state of

$$\tau_r > 2.0 \cdot 10^4 \text{s} = 5.7\,\text{h}. \tag{4.26}$$

In order to get an idea whether depletion through iradiation of the ions by the laser light inside CSR could influence the measurement, an estimate of the time scale of this process will be given in the following section.

4.4.1 Estimate of the depletion time scale

In order to estimate the depletion time scale τ_{pd} that originates from the interaction with the IR laser, the calculated photodetachment cross section (see Table 2.3) is applied. Since the power of the Vis laser is much lower, while the cross sections of the photodetachment of both metastable states are comparable for both lasers, the depletion timescale for the measurements using the Vis laser is much larger. The depletion time scale for the metastable states can be calculated via

$$\tau_{pd} = \left(\sigma_{pd} \phi \frac{L_{ov}}{L_{csr}} D \right)^{-1} \tag{4.27}$$

with $\phi = 8.9 \cdot 10^{15}$ cm^{-2}s^{-1} as the photon flux per area and second (effective laser power of $P = 1\,\text{mW}$ at $0.89\,\text{eV}$ photon energy and a laser radius of $r_L = 0.5\,\text{cm}$), and the fraction of laser-ion overlap length L_{ov} of the total closed orbit $L_{CSR} = 3500\,\text{cm}$ of the ions. Knowing the angle $\theta = 3.4°$ between the laser and the ions, the overlap length is given by $L_{ov} = 2r_L/\sin\theta = 16.9\,\text{cm}$. The duty cycle D for the IR laser is $D = 0.25$.

Since the ^{2}P states are short-lived, only the cross sections of the long lived ^{2}D states are of interest. To gain a conservative value, an effective cross section is calculated using the sum of the calculated cross sections from the ^{2}D$_{3/2}$ and ^{2}D$_{5/2}$ state to the neutral states (see 2.3), leading to $\sigma_{pd} = 4.58 \times 10^{-18}$cm^{-2} for the ^{2}D$_{3/2}$ and $\sigma_{pd} = 2.65 \times 10^{-18}$cm^{-2} for the ^{2}D$_{5/2}$ state. Weighting the cross sections with the multiplicities of both states gives an effective cross section of $\sigma_{pd} = 3.4 \times 10^{-18}$cm^{-2}. Using this effective cross section, results in a coarse estimate for the depletion time scale of $\tau_{pd} = 2.0 \cdot 10^4 s$. Please note that the exact laser-ion overlap was not tuned for optimal overlap and the effective laser power is not precisely known. Also the calculated cross sections have an uncertainty of 50%.

Comparing the depletion time scale to the lower limit of the radiative lifetime in the previous section (4.4), shows that both lifetimes have very similar values. It should be noted that the estimate of the depletion time scale is only very coarse, with the effective laser power and the photodetachment cross section having large uncertainties. Also due to the fact that both decay time constants in the laser signals (see Fig. 4.4) are identical within the error margins, shows no indication of laser depletion. Nevertheless it is possible that depletion already limits the observable lifetime.

Although we can not derive a value for the lifetimes of the ^{2}D states, the long lifetime we obtained by comparing both photodetachment signals, shows the great potential with these kind of low rate measurements inside CSR. At present, this is the longest metastable state observed experimentally for an atomic anion.

4.5 Signal at short storage times: Hints for the population of the ^{2}P state

We observed a noticable difference between the two laser signals at short storage times. To emphasize the difference we subtracted the neutral count rates caused by the two lasers.

For the single exponential fit, only decay constants are needed in order to estimate the lifetimes. In case that the fit function is modified the same as the data, any data modification like a different linear combination will leave the decay constants unaffected. From this follows that multiplying the Vis laser signal by a constant factor and then subtracting the result from the IR laser signal is possible, in order to see the difference in both laser signals. The constant is chosen such that both signal rates are roughly equal. Given that both lasers show the same behavior, the resulting rate should be zero. However, having a feature, within one of the laser signals, will appear as a visible difference. Here we also assume that the Vis laser is proportional to intrinsic beam losses. This method is used to enhance weak features by getting rid of strong features that are found in both data sets. Fig. 4.5 shows the resulting count rate. The feature at

Figure 4.5: Rates obtained in the difference signal of the Vis and IR laser after multiplying by a constant factor and subtracting the Vis laser signal. The inset shows a zoom into the short storage times and the red line shows a single-exponential fit. A constant offset has been added to the data and the dashed line shows the zero level

short storage times $\tau_{eff} = (17.5 \pm 1.8)$s is fitted by a single-exponential decay resulting in an effective lifetime of

$$\tau = \left(\frac{1}{\tau_{eff}} - \frac{1}{\tau_{beam}} \right)^{-1} = (18.4 \pm 1.7)\text{s} \qquad (4.28)$$

where $\tau_{beam} = (358.4 \pm 3.0)$s attributed to the beam decay constant derived from the fit to the Vis laser signal at long storage times. The value for the effective radiative lifetime would change to $\tau = 24.0$ s however, if we take τ_3 as the dominant beam decay constant at short storage times from table 4.2 for $N_{ion} = 7.4 \times 10^8$. Since there is a single exponential decay at short storage times in the difference signal of both lasers, effects like storage ring stability and other slow varying artifacts can be excluded. Thus, the observed difference can be assigned to a difference in photodetachment cross section of both lasers. It could be possible that this lifetime is owed to the decay of the ^{2}P state which has predicted lifetimes that are also in the range of ≈ 20 s. However the data shown in fig. 4.5 could not be reproduced in subsequent runs, and additional measurements with a pulsed laser were carried out and are shown in section 4.9.

(a) Collisional background during first beamtime   (b) Collisional background of second beamtime
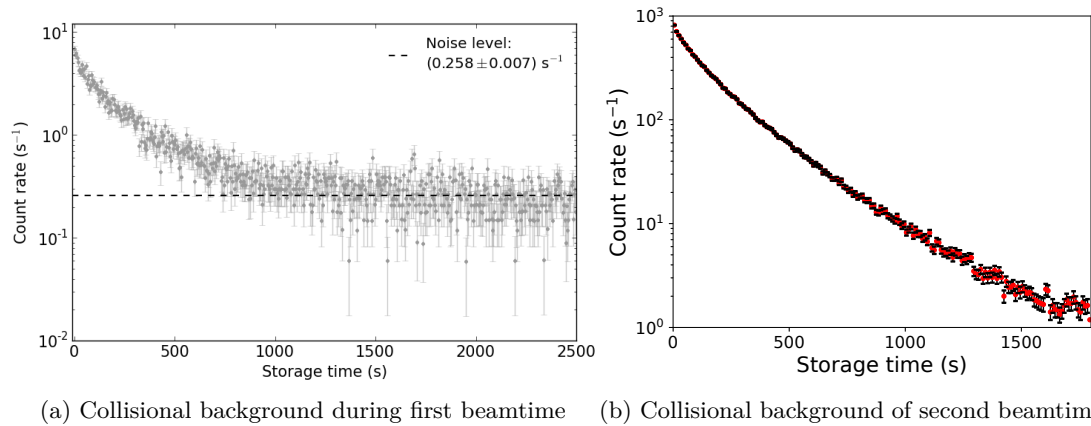
Figure 4.6: Comparison of the collisional background from both beamtime campaigns. The data shows neutralized particles counts detected by COMPACT when there was no laser on.

4.6 Residual gas pressure inside CSR

Until now, only results from the first beamtime campaign have been presented. After the first beamtime campaign on Si^- some questions remained unanswered, which will be discussed in Sec. 4.7. The different measurement conditions throughout both beamtime campaigns will be discussed in the following. In the second beamtime campaign, parts of the cryomachine were not working very well, which resulted in temperature variations and therefore also pressure fluctuations inside the experimental vacuum chambers. Additionally the electron cooler and the extraction section have been introduced into the CSR, possessing additional open areas, where a 300 K radiation field is present. Furthermore, the complete campaign conducted in 2018 was intended as a test beam time, and the experimental vacuum chambers have not been baked. One way to monitor those changes is to check for the residual gas density or pressure.

As in von Hahn et al. 2016, initial measurements showed a particle density of less than $140 \, cm^{-3}$ which is the room temperature equivalent of less than 10^{-14}mbar. The first data set on Si^- was also conducted during the same beamtime. In this case the pressure cannot be measured by ion gauges any more. It can only be inferred from beam lifetimes or the neutralization rate on the particle detector.

Obtaining the number density (which is used to calculate the room temperature equivalent pressure) requires the determination of stored ions using the capacitive pick-up electrodes (for more details see Laux 2011) and counting the neutralized ions with the detector at the same time. Applying the same formula (as in von Hahn et al. 2016) for the first Si^- beamtime:

$$n_{rg} = \frac{R_{cd}}{\epsilon N_{ion} f_0 l_b \sigma_{cd}} \tag{4.29}$$
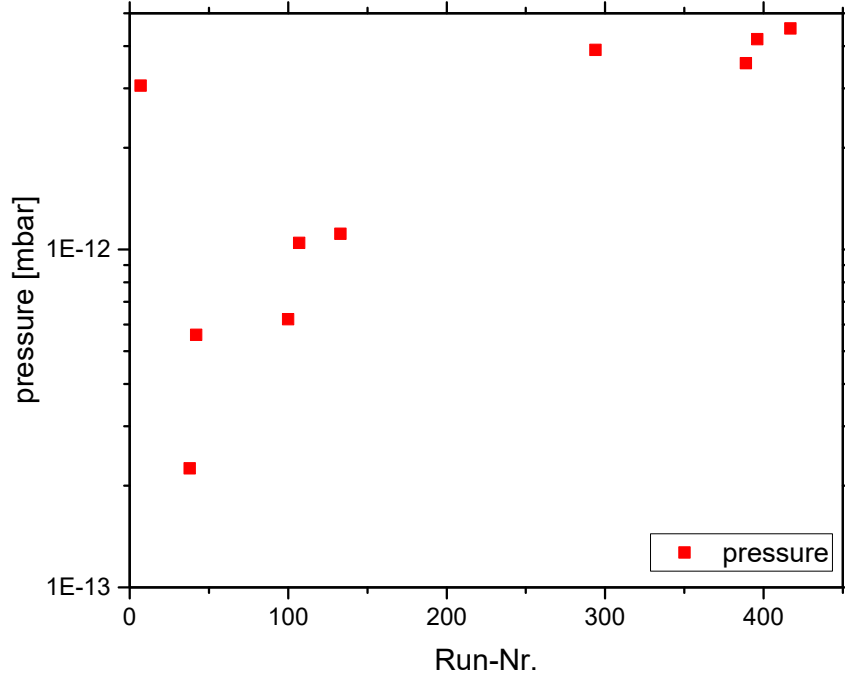
Figure 4.7: Pressure throughout the second Si$^-$ beamtime.

with the same detection efficiency $\epsilon = 0.09^{+0.12}_{-0.01}$ which attributes for geometric losses due to the limited detection area as in von Hahn et al. 2016. $N_{ion} = 2.9^{+0.4}_{-1.7} \cdot 10^8$ denotes the number of stored ions, $f_0 = 18.3 \, \text{kHz}$ is the revolution frequency, $l_b = 1.5 \, \text{m}$ denotes the length of the straight section in front of the detector and $\sigma_{cd} = 7.7 \cdot 10^{-16} \text{cm}^2$ is the literature value of Si$^-$ ions stripping in a helium gas target (Luna et al. 2001) at the relevant cross section. Although the detachment cross sections between H$_2$ and He gas targets vary slightly, the estimate for the number density should be reasonable. The rate R_{cd} on the detector is shown in Fig. 4.6 (a) and is attributed to detachment by collisions with residual gas plus the dark count rate $R_{darkcount}$. After $\approx 1500 \, \text{s}$ the signal drops below the noise level of the detector of about $R_{darkcount} = 0.258(7) \, \text{s}^{-1}$. The number of ions was measured within the first second while the rate on the detector was measured to $R_{cd} = 7 \, \text{s}^{-1}$. This results in a number density of $n_{rg1} = 130^{+260}_{-70} \text{cm}^{-3}$, which is comparable with the previous estimate.

In a next step, this estimate is compared with the second beamtime shown in figure 4.6 (b). The count rate on the detector is approximately two orders of magnitude higher, while the detector noise level was improved from $R_{darkcount} = 0.26 \, \text{s}^{-1}$ down to $R_{darkcount} \approx 0.07 \, \text{s}^{-1}$, resulting in a higher signal to noise ratio. Using equation 4.29 with $R_{cd} = 850 \, \text{s}^{-1}$ and $N_{ion} = 2.3 \cdot 10^7$ leads to a number density of $n_{rg2} = 198^{+24}_{-113} \times 10^3 \text{cm}^{-3}$. Converting the number densities to pressure limits at room temperature $T = 300 \, \text{K}$ using $p = n_{rg} k_b T$ leads to $p_1 < 10^{-14} \text{mbar}$ and $p_2 < 10^{-11} \text{mbar}$. This demonstrates that vacuum conditions got worse by orders of magnitude in the second beamtime. One possible explanation might be the upgrade on the experiments, namely

the installation of the electron cooler as well as the extraction section, which both have a room temperature vacuum system that merges into the experimental vacuum system of the CSR. However, while both contribute to a somewhat increased gas density, later beamtimes have shown that this effect is much smaller. Most importantly for the present experimental campaign, the cryomachine was running in an unstable mode, resulting in pressure fluctuations throughout the beamtime. Additionally, the experimental vacuum chambers have not been baked. Figure 4.6 (b) only shows one run taken. In order to demonstrate these fluctuations during the second beamtime, all the runs where the ion number N_{ion} and initial count rate on the detector were recorded, are presented in Fig. 4.7. The calculated values of the pressure (room temperature equivalent) for the individual runs show large deviations in the order of a magnitude. That reflects the difficulties caused by the unstable mode of the cryomachine. The collisional background rate for all of the results that will be presented in the following sections, is increased by at least two orders of magnitude, but the measurements still gave useful results.

4.7 Depletion Measurements

So far only the data from the first measurement campaign has been used. From these first measurements on Si$^-$ three questions remained open:

1. What is the fraction of ions that are in a metastable state?

2. Do the intermediate decay constants ($\approx 160\,$s see Figure 4.2 and Table 4.1) originate from metastable state decay or do they indicate a storage ring-related lifetime?

3. Does the feature in Fig. 4.5 at short storage times really originate from the weakly bound ^{2}P states?

In order to address the first two questions a continuous laser at relatively high power was utilized, which is able to create a pure ground state ^{4}S$_{3/2}$ Si$^-$ beam by depleting all of the excited states. Thus detachment signals obtained from lasers or collisions will only reflect the decay of the stored ion beam. A CW Nd:YAG laser at a wavelength of 1064 nm and a maximum power output of 2.7 W was installed at laser port 3 with a grazing angle of 1.1° (see Figure 3.1).

Similar to the previous measurements two probe lasers were used at laser port 3 at the same path as the depletion laser. One Vis diode laser with a wavelength of 632 nm and a power of 5 mW and another IR diode laser with a wavelength of 980 nm and a power of 10 mW. The Vis laser is able to detach all anionic states whereas the IR laser is only able to detach the metastable states. The total laser cycle period was 10 s in
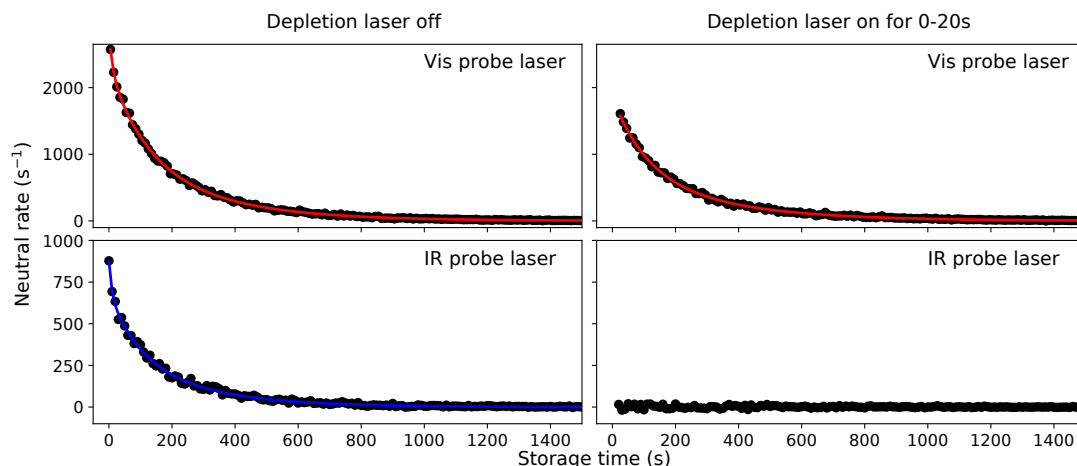
Figure 4.8: Photodetachment signals for the probe lasers with and without 20 s of depletion (laser-off background is subtracted). Number of injected ions was $N_{ion} = 2.5 \cdot 10^7$. The red and blue lines are multi exponential fits (parameters are in Table 4.3) for the Vis and IR laser, respectively.

Table 4.3: Fit parameters from multi exponantial fits for Figure 4.8.

	τ_1 (s)	A_1 (s^{-1})	τ_2 (s)	A_2 (s^{-1})	τ_3 (s)	A_3 (s^{-1})
no depletion Vis laser	288 ± 13	1022 ± 125	116 ± 11	1282 ± 98	10.9 ± 4.4	533 ± 118
no depletion IR laser	263 ± 21	308 ± 69	101 ± 20	374 ± 55	8.9 ± 4.7	196 ± 48
depletion Vis laser	306.9 ± 6.8	813 ± 50	104 ± 7.1	1049 ± 46	-	-

which the lasers were switched in the following pattern: 0.5 s IR - 4.5 s lasers off - 0.5 s Vis - 4.5 s lasers off. However, for the first 20 s only the depletion laser was switched on at maximum power (2.7 W). During this time frame no data was recorded and the detector was switched off, in order to not saturate or damage the detector during this high neutral count rate.

Figure 4.8 shows the background-subtracted photodetachment signal for both probe lasers with and without depletion. Having basically no signal from the IR laser after 20 s of depletion, confirms that the metastable states have all been removed from the stored Si$^-$ beam.

Multi-exponential fits have been applied to the recorded data (the parameters are given in Table 4.3). In comparison to the previous measurement (see Table 4.1) campaign the time constants seem to be shorter now. The reason for this shortened time constants is likely due to the much higher residual gas pressure inside CSR. Another point is the $\tau_3 \approx 10$ s lifetime component which might indicate the presence of the ^{2}P

states. It disappears in the Vis laser signal after 20 s of depletion, since data taking only started afterwards. Furthermore the 60 s lifetime component that was present for a high number of stored ions vanished, since much fewer ions were injected. Most importantly, the $\tau_2 \approx 110$ s component is the strongest component and does not change its relative strength in comparison to τ_1. Both components remain at comparable amplitudes after depletion has been introduced. Thus this component is attributed to storage ring effects and is not caused by metastable state decay. Consequently no signal was observed that could be linked to the lifetime of 162 s for the $^2D_{3/2}$ calculated by O'Malley and Beck 2003.

4.8 Fraction of metastables in the beam

By using the Nd:YAG depletion laser at a moderate power of 30 mW and reducing the number of ions to an extent that the detector was not saturated, allowed the quantification of the fraction of stored ions in metastable states. Depletion was monitored for the first minute of storage as depicted in Figure 4.9. The number of ions was reduced such that after the laser is turned off, the laser-off count rate follows a single exponential decay. In comparison to previous measurements, we only used a comperatively low number of ions $N_{ion} = 1 \cdot 10^7$. In order to estimate the number of ions in metastable states, the single exponential fit for the laser-off phase was extrapolated towards short storage times and subtracted from the integrated counts in the laser-on phase. Additionally, the laser power was optimized in order to make the step visible after 60 s as small as possible. All the counts above the extrapolated curve are attributed to the photodetachment signal and are summed together, resulting in 30 000 neutrals caused by the photodetachment of ions in a metastable state. Assuming the detector efficiency $\epsilon = 0.09^{+0.12}_{-0.01}$ (von Hahn et al. 2016) and the initial number of stored ions, leads to a metastable ion population of 3.3% (with a large uncertainty factor of 2.5 with the above assumptions). This measurement was repeated for various source settings tying to try to increase this fraction, however this was not possible. Therefore this measurement is used as confirmation for the assumption that the photodetachment signal of the Vis laser is dominated by the negative $^4S_{3/2}$ ground state that was used in the derivation for the lower limit of the ^2D states in section 4.4.

Figure 4.9: Neutral count rates measured with the depletion laser at moderate power. For the first 60 s of this measurement the Nd:YAG laser was switched on. The red curve is a single exponential decay fitted for the laser-off phase and extrapolated to shorter times. The number of counts from photodetachment was estimated by integrating the counts in the laser on window and subtracting the extrapolated curve.

4.9 ^{2}P states decay observed with a pulsed laser

In order to obtain a signal for the weakly bound ^{2}P state, we used a pulsed laser at 2450 nm. Since the residual gas pressure was much higher in the second beamtime, the pulsed laser offers the great advantage of coincidence counting with nanosecond laser pulses which helps reducing the background signal by detachment from residual gas collisions. A pulsed OPO (Ekspla NT342b) laser was used at 2450 nm (0.506 eV) which is just below the binding energy -0.53 eV of the ^{2}D states. Thus the laser only detaches the ^{2}P states. The laser was operated at its limits considering its output range and only very little effective laser power of 1 μJ could be guided to the laser-ion interaction zone. The laser had to be placed in laser port 2 into a crossed beam configuration as seen in Figure 3.1, since the mirrors for the diagonal laser ports are only suitable for wavelengths from 300 nm $-$ 2000 nm. This results in a significantly reduced laser-ion overlap. However, the pulsed laser offers a strong background supression with short laser pulses of 5 ns, at a repetition rate of 20 Hz. These time windows can be used to assign detected counts. The inset of Figure 4.10 shows a measurement that lasted ≈ 5 h (in which $\approx 3 \cdot 10^5$ pulses were generated) where the counts are shown as a function of time after laser pulse. Knowing the distance from the laser interaction section to the detector (3.3 m), and the ion velocity ($6.4 \cdot 10^7$ m/s), the time of flight can be calculated to 5.2 μs. A clear peak is showing up at the expected time of flight period. Although as much ions as possible were injected (up to 10^9 ions) in order to boost the signal, we only observed less than one event every injection (with 20 s storage times).
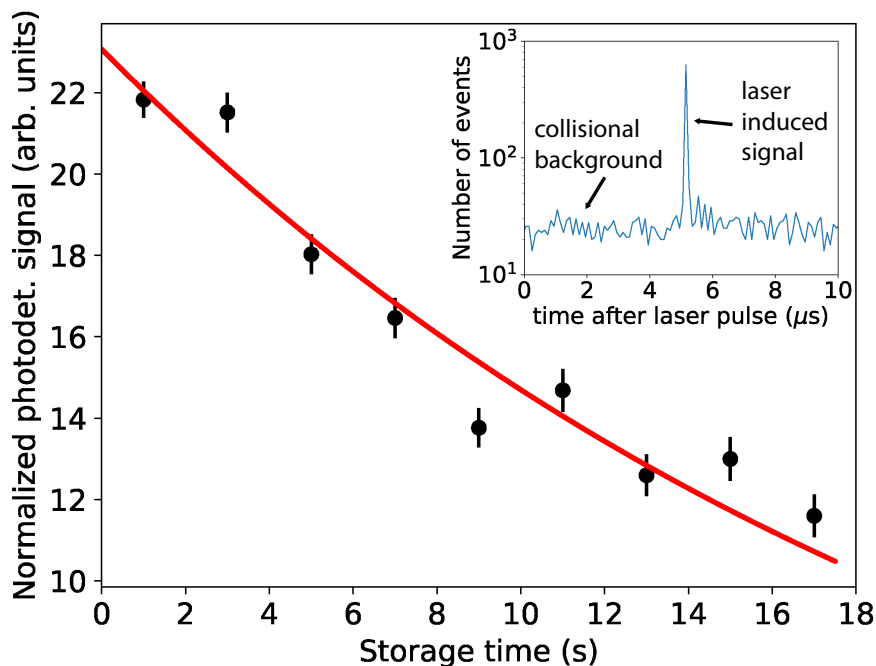
Figure 4.10: Background subtracted normalized photodetachment signal using a pulsed OPO laser. The laser was set to 2450 nm and is only detaching the ^{2}P states. A single exponential was fitted to the data (red curve) showing a lifetime of $\tau = (22.5\pm2.5)$s. The inset is showing neutral counts in dependence of time after laser pulse.

A narrow time window with a width of $0.2\,\mu$s has been used to assign laser events. The collisional background events have been averaged and then subtracted from the events inside the laser window. Consequently the background subtracted photodetachment signal was divided by the averaged collisional background at the respective storage time bins, where the resulting normalized photodetachment signal is expected to be independent of beam loss processes. The signal is shown in Figure 4.10. Performing a single exponential fit results in a lifetime of $\tau = (22.5 \pm 2.5)$s. This time constant is assigned to the combined decay of the ^{2}P states. Comparing this experimentally obtained value with the present MCDHF calculations shown in the previous theory section 2.2 and with the single value from O'Malley and Beck O'Malley and Beck 2003 gives an excellent agreement. The lifetimes given in Andersson et al. 2006 appear to be a bit larger (see table 2.2.4).

4.10 Summary and conclusive remarks

The metastable states of the silicon anion in the $3p^3$ electron configuration (half-filled), sets a fascinating case for lifetime studies. It is particularly challenging because of the long lifetimes (small rates) and the small binding energies of the ^{2}P states. The CSR offers a unique experimental evniroment in order to study those properties. The low temperatures inside the cryogenic vacuum chambers reduce black body radiation drastically and the long storage lifetimes that are achievable by the low residual neutral gas densities enable this kind of studies with only minimal external perturbations.

Measurements in the first beamtime showed a possible hint on the ^{2}P state lifetime. Since those measurements were not reproducible and only occured within one run, in the second campaign a pulsed OPO at 2450 nm was used to determine a lifetime of $\tau = (22.5 \pm 2.5)$. The measured lifetime agrees very well with our updated MCDHF calculations. This value also agrees well with the ^{2}P$_{1/2} = 23.6$ s state lifetime given by O'Malley and Beck 2003. The lifetimes given by Andersson et al. 2006 are slightly longer (in the range of $25.1\,\text{s} - 28.1\,\text{s}$). Furthermore all of the lifetimes that have been calculated by Andersson et al. 2006 and O'Malley and Beck 2003 are longer than the lifetimes presented with the recent MCDHF calculations, which have been performed with more computing power and more possible states have been taken into account.

The measurements using a strong infrared CW laser enabled laser depletion measurements. They revealed that the fraction of metastable ^{2}D and ^{2}P Si$^-$ ions from the sputter ion source is $\approx 3\%$ having a large uncertainty factor of around 2.5. In order to increase the fraction of metastables in future experiments, double electron capture by a positively charged Si$^+$ beam in a vapor cell could be prepared (see Lee et al. 1997 for ^{2}D states of C$^-$).

At long storage times the photodetachment signals generated by the IR laser, which only probes the metastable Si$^-$, and the Vis laser, probing all of the Si$^-$, are very similar. This indicates that there has to be at least one very long-lived metastable state which has a lifetime of $> 5.7\,\text{h}$ at a 90% confidence level. In comparison with the theoretical calculations, an assignment to the ^{2}D states seems reasonable. O'Malley and Beck 2003 predicted a lifetime of 162 s for the ^{2}D$_{3/2}$ state, which does not reflect the experimental data. Although a lifetime component of $\approx 120\,\text{s}$ additional depletion measurements demonstrated that this lifetime component does not originate from the metastable anionic states. The hypothesis that the ^{2}D$_{3/2}$ state is not populated by the ion source and therefore will not appear in the detachment signal, is unlikely, since in previous measurements the populations in the ^{2}D fine-structure levels have been found to be close to thermal (Scheer et al. 1998).

The MCDHF calculations presented in this work provide an excellent match to our data. The lower limit of 5.7 h makes this ^{2}D state, to the best of our knowledge, the longest lifetime limit observed for any metastable state in negative ions.

In order to improve the measurement the stored Si$^-$ beam can be phase space cooled via the CSR electron cooler, which will reduce losses because of diffusive beam growth.

This technique has already been applied on various atoms and molecules improving storage lifetimes. Increasing the storage lifetimes even further, this might at some point help to distinguish between the theoretical calculations which range from $9\,\mathrm{h}$ up to $27\,\mathrm{h}$. Our understunding of the storage ring parameters keeps improving, and so are the observed lifetimes. So far, in a non-published work a lifetime of $3400\,\mathrm{s}$ of uncooled Al_4^- has been recently demonstrated, and will be discussed in the course of this work.

Part II

Studies on the cooling behavior of isolated Al_4^- molecules in a cryogenic storage ring

Chapter 5

Cooling of isolated systems and the Al_4^- molecule

The second part of this work is focused on the cooling of isolated clusters systems. The Al_4^- molecule will be used as a model system.

This chapter provides an overview on the properties of the Al_4^- ion. Firstly, an introduction on the cooling of isolated molecules will be given, followed by an overview of the previous works that have been conducted on Al_4^-. Then the states of Al_4^- will be shown and a method to calculate cooling times will be explained. The importance of internal vibrational redistribution (IVR) will be discussed. Next, a theoretical description of delayed electron emission will be given. Finally, the process of photon-induced delayed electron emission will be explained, and a way to calculate the electron emission rate will be described.

5.1 Introduction

The radiative cooling of polyatomic molecules and clusters is an interesting thermodynamical process. It is particularly interesting for systems with a small number of atoms, where the thermodynamical principles are not easily applicable. Many physical applications and systems require a comprehensive understanding of the radiative cooling process. In the interstellar medium, molecules offer the only pathway for converting kinetic collision energies into radiation, which eventually escapes from dense regions, and thus can facilitate star formation (Glover 2005). Ion traps and storage ring devices have been employed to keep clusters and molecules in a well-confined space for long enough time for them to cool down to the ambient temperatures (L. Andersen, Heber,

and Zajfman 2004). Another aspect of radiative cooling for large molecules is discussed in Hackermüller et al. 2004. Since large molecules can store much energy in numerous degrees of freedom, the internal energy can be converted into thermal radiation and then induce decoherence. The field of quantum technologies has led to a large interest in decoherence, since this is the process that limits the appearance of quantum effects, turning them into classical phenomena.

The cooling process of smaller molecules has been studied in detail in previous works. The vibrational cooling times of diatomic HD^+ (Amitay et al. 1999) and triatomic H_3^+ (Kreckel et al. 2004) have been measured at the room temperature Test Storage Ring (TSR), which was also located at the Max Planck Institute for Nuclear Physics. Measurements of rotational cooling have become accessible with the CSR, which is offering a very low ambient temperature and long storage times. Measurements on CH^+ (O'Connor et al. 2016) and OH^- (C. Meyer et al. 2017) have been conducted, where rotational cooling was observed for both systems.

Moving to systems with a larger number of atoms, such as Al_4^-, adds more possible modes combined with a smaller level spacing. This could give access to a statistical description of this system, since vibrational cooling will not show the same behavior as for diatomic molecules, which can be described by a set of exponential functions, with each of the exponential functions corresponding to one vibrational mode.

It is technically challenging to measure direct radiative cooling of small isolated systems, since the photon flux is very low. Optical emission spectra have been recorded on C_{60} (Mitzner and Campbell 1995), niobium (Nb) clusters (Frenzel, Roggenkamp, and Kreisle 1995) and tungsten (W), and hafnium (Hf) clusters (Frenzel et al. 1997). Typical cluster sizes were above 60 atoms at temperatures above $2000\,K$. Further developments in ion trapping and ion storage devices allow for indirect observation of radiative cooling. Typical time scales have been measured for this process. For small polyatomic molecules 'slow' radiative cooling rates (on the order of $\sim 1\,s^{-1}$) have been measured and are assigned to infrared-active vibrational transitions (Dunbar 1992). For metal clusters, fast radiative cooling on the order of ms has been reported (Hansen et al. 2001 and Warring et al. 2009) at temperatures above $1000\,K$.

5.2 Previous Work on Al_4^-

An overview of studies carried out on the Al_4^- molecule, both experimentally and theoretically, will be given in the following section.

First experimental studies on Al_4^- have been conducted in an electrostatic room temperature ion beam trap by Toker et al. 2007. The stored Al_4^- molecules, which were produced in a hot ion source, have been irradiated with a short laser pulse (ns) at different storage times. Besides prompt electron detachment or prompt dissociation of

the molecule, also the respective delayed process is observable. Delayed electron emission proved to be a very effective method to study molecular properties. The following processes of detachment or dissociation are possible:

$$Al_4^- + h\nu \rightarrow Al_4^{-*} \rightarrow \begin{cases} Al_4 + e^- (2.13\,\text{eV}), & (5.30a) \\ Al_3^- + Al(2.67\,\text{eV}), & (5.30b) \\ Al_2^- + Al_2(3.28\,\text{eV}), & (5.30c) \\ Al^- + Al_3(4.09\,\text{eV}), & (5.30d) \\ Al_4^- + h\nu'. & (5.30e) \end{cases}$$
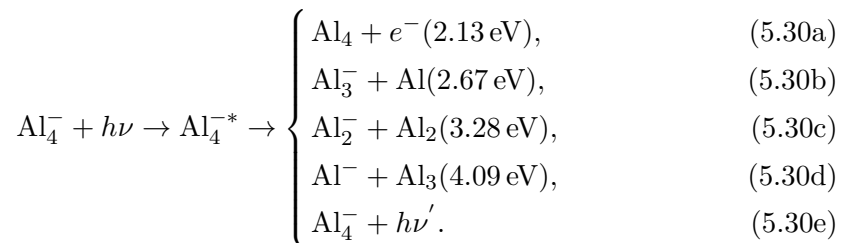
The barrier energies in the above formula have been taken from Aviv et al. 2011. Spectra of delayed electron emission (case (a)) were recorded for up to hundreds of microseconds after firing the laser at a photon energy of 2.063 eV. Note that the photon energy is below the nominal detachment threshold, and therefore detachment is only possible for excited ions. The authors found that the rate of delayed electron emission was dependent on the internal excitation of the clusters before laser irradiation. In this way, they used the rate as a probe for the canonical temperature of the clusters as a function of storage time. The measured radiative cooling rate was described by a generalized Stefan-Boltzmann law (T^b with $b = 3.5 \pm 0.2$), analogous to the cooling of a blackbody. The authors concluded their work with stating that there have to be either electronic transitions or very collective infrared-active vibrations at transition energies of $\sim 200\,\text{meV}$. However, for modelling the generalized Stefan-Boltzmann law, which is done by a complex fitting procedure, the adiabatic electron detachment energy was needed as an input parameter.

Several studies were conducted on theoretical models describing the neutral aluminum clusters (Upton 1987; Meier, Peyerimhoff, and Grein 1990; Sun et al. 2006). Those studies were successful in describing a variety of properties with increasing clusters size. However, the theoretical models in these publications are not suitable for predicting reliable electron detachment energies of negative ions. First calculations on the electron affinity of Al_4^- are given in Zhao and Zhang 2007, using the Möller-Plesset perturbation theory. More recently, Sommerfeld 2010 has adressed missing points like the postulated states at transition energies of $\sim 200\,\text{meV}$ and a more precise value for the adiabatic electron detachment energy, by utilizing complete-active-space self-consistent-field calculations (CASSCF) (16 orbitals, 12 or 13 electrons). This approach shows that using a single-reference configuration to describe the electronic structure of the relevant states is well-suited. For quantitative predictions, electron correlation effects beyond second-order perturbation theory are needed. The coupled-cluster method is employed to describe several low-energy states of Al_4 and Al_4^-. Möller-Plesset perturbation theory (MP2) has been used to calculate minimal energy structures. The calculations show that Al_4^- and Al_4 both have several low-lying electronic states in the order of a few hundred meV. Also, values for the adiabatic electron detachment energy are given for the ^2A_g and $^4B_{3u}$ states of Al_4^- at 2.17 eV and 1.98 eV, respectively.

Another experimental study has been performed by Aviv et al. 2011 at a bent electrostatic ion beam trap, which enabled simultaneous measurement of delayed electron and delayed atom emission from photoexcited Al_4^- clusters for up to $400\,$ms of storage. Both decay channels have been studied in a photon range of $1.55\,$eV to $2.25\,$eV. Integrated relative cross sections, decay spectra and branching ratios have been measured as a function of storage time and photon energy. Interestingly, it was found that at all photon energies, delayed one-atom fragmentation was competing with electron emission and even dominates at photon energies below $1.7\,$eV. This was unexpected, as the calculated binding energies are $\sim 0.5\,$eV higher than the electron detachment energy. The authors assign this to some of the Al_4^- molecules having effective barrier energies for one-atom fragmentation below the channel of electron detachment. It was assumed that states with high rotational angular momenta, which are populated in the cool-down process of Al_4^-, show these reversed barrier energies and are responsible for the competition of delayed fragmentation and detachment even at low photon energies. The authors of the paper conclude with the suggestion, to repeat this measurement on Al_4^- with colder ions.

In the experimental studies that have been carried out by Kafle et al. 2015 at a bent electrostatic ion beam trap, absolute photodetachment cross sections of Al_4^- have been measured for photon energies between $1.8\,$eV $- 2.7\,$eV. Simultaneous measurement of the neutral Al_4 and the Al_3^- fragment showed the competition between both processes. Again it was observed that for photon energies below $\sim 2.2\,$eV, fragmentation was the dominant process, even though its threshold is expected to be higher than the electron detachment energy. They found the adiabatic electron detachment energy of Al_4^- to be $E_a = (2.18 \pm 0.02)$eV and the one-atom fragmentation to be $D_0 = (2.34 \pm 0.05)$eV.

The studies conducted at the Max Planck Institute for Nuclear Physics by Lange et al. 2012 have been investigating the radiative cooling of Al_4^- and Al_5^- cluster anions in a cryogenic ion beam trap with an ambient temperature $< 15\,$K and storage times of $3\,$s. A statistical rate model of the measured delayed detachment rate after laser excitation was applied and a vibrational temperature as a function of cooling time was inferred. It was shown that the vibrational cooling slows down, once the ions reach approximately room temperature, which was assigned to fast initial cooling because of the presence of low-lying electronic states of the anion. Lastly, the radiative cooling of Al_5^- appears to be slightly slower than for Al_4^-.

5.3 States of Al_4^-

In order to understand the physical properties and observations obtained in our measurement, calculations on the electronic structure and vibrational levels will be discussed in the following. The calculations for the electronic structures were done by our
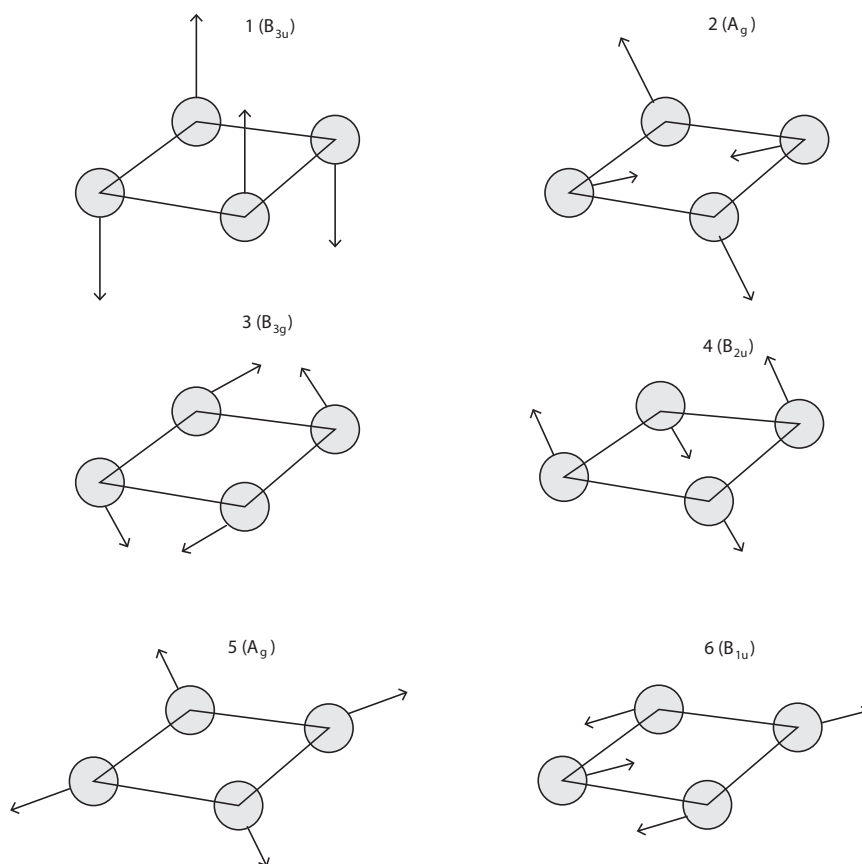
Figure 5.1: Visualization of the six vibrational modes for the electronic ground state (^2A_g) of Al_4^-. The blue arrows indicate the direction of motion.

colleague Mark Iron at the Weizmann Institute of Science in Israel (Iron 2022). Density functional theory calculations were done, using Gaussian16 revision C.01. (Frisch et al. 2016) in order to obtain optimized geometries. Coupled-cluster calculations were done, using CFOUR version 2.1. (Matthews et al. 2020) in order to determine accurate level energies.

The same D_{2h}-symmetry (Hermann-Mauguin notation) geometry as in Zhao and Zhang 2007 and Sommerfeld 2010 have been used as a starting point. The geometry was then optimized at B2PLYP/def2-QZVPPD level of theory. The binding energies were determined, using coupled cluster calculations for single and double excitation and a perturbative estimate of triple excitations (CCSD(T) Stanton 1997) in a similar way, as it was previously used on the C_{10}^- system (Saha et al. 2018).

The geometry parameters for the different low-lying electronic states of Al_4^- are given in table 5.1.

Al_4^- has a rhomboidal symmetry with six vibrational modes (3N-6) in the electronic ground state, which are given in table 5.2. The vibrational frequencies are scaled by a factor $\lambda_{zpe} = 0.9987$, as described in Iron and Gropp 2019, which results in more

Table 5.1: Geometric parameters for the electronic states of Al_4^-. Bond distances r_1 in Å, angles Θ in degrees. Relative energies ΔE_e in eV.

State	Point Group	r_1 (Al-Al)	θ(Al-Al-Al)	ΔE_e B2PLYP	ΔE_e CCSD(T)/aQZ	ΔE_e CCSD(T)/CBS
^2A_g	D_{2h}	2.5533	106.1	0.000	0.000	0.000
$^2A_{2u}$	D_{4h}	2.6236	90.0	0.120	0.142	0.152
$^2B_{1g}$	D_{4h}	2.4543	90.0	0.794	0.340	0.329
$^4B_{1g}$	D_{2h}	2.5781	115.7	1.284	1.204	1.213
$^4B_{2g}$	D_{2h}	2.6891	116.2	0.765	0.722	0.739
$^4B_{2u}$	D_{2h}	2.6356	120.8	0.241	0.205	0.219
$^6A_2$	D_{2d}	2.6559	69.3	1.027	0.849	0.867

reliable zero-point (vibrational) frequencies. Three of those modes are IR active, with the highest vibrational mode B_{3u} at $43.2\,\text{meV}$ featuring a radiative lifetime of $19.75\,\text{s}$. The lifetimes of the other two vibrational modes are $3.19\,\text{s}$ for the B_{2u} and $39.17\,\text{s}$ for the B_{1u} mode, respectivley. The vibrational lifetimes τ_{ν_i} for the respective level are calculated from Einstein coefficients

$$\tau_{\nu_i} = \left(\sum_j A_{\nu_i,\nu_j} \right)^{-1}, \tag{5.31}$$

where A_{ν_i,ν_j} are the Einstein-A coefficients. They are given by the expression (see Bernath 2020 for more details)

$$A_{\nu_i,\nu_j} = 7.5346063 \times 10^{11} \cdot \nu_{i \to j}^2 \frac{2J'' + 1}{2J' + 1} \int \sigma d\nu. \tag{5.32}$$

Here, $\nu_{i \to j}^2$ denotes the energy (in $[\text{cm}^{-1}]$) between the modes i and j, and σ is the cross section. Since the output of the software for the infrared intensity I_{IR} is given in $[\text{km/mol}]$, it has to be first converted into the integrated absorption cross section $\int \sigma d\nu$ (in units of $[\text{cm/molecule}]$):

$$\int \sigma d\nu = \frac{10^5}{ln(10)N_A} I_{IR}, \tag{5.33}$$

with N_A being Avogadro's constant. J' and J'' are the total angular momenta of the initial and final state. For Al_4^-, the transition from the respective vibrational excited levels to the ground state (occupied rotational numbers are high (≈ 200) as estimated in subsec. 5.4.4) is approximated by $J' \approx J''$. The Einstein-A coefficient is then calculated by

$$A_{\nu_i,\nu_j} = \frac{1.25115 \times 10^{-7}}{ln(10)} \cdot \nu_{i \to j}^2 \cdot I_{IR} \left[\frac{\text{km}}{\text{mol}} \right]. \tag{5.34}$$

Table 5.2: Scaled frequencies, vibrational energies, IR intensities and radiative vibrational lifetimes for the electronic ground state ^2A_g (D_{2h}) of Al_4^-.

vibrational symmetry	scaled frequency (cm^{-1})	vib. energy (meV)	IR intensity (km/mol)	radiative lifetime (s)
B_{1u}	86.687	10.748	27.1489	39.17
A_g	166.502	20.644	0	-
B_{2u}	273.174	33.869	33.5647	3.19
B_{1g}	285.139	35.353	0	-
A_g	316.297	39.216	0	-
B_{3u}	348.645	43.226	3.33	19.75

Fig 5.1 shows these modes. The modes 2 to 6 are in plane, while mode 1 breaks the planar symmetry.

5.4 Cooling processes

After introducing the states of the Al_4^- molecule, it is interesting to see how these states behave in the cryogenic environment of the CSR. Ions are typically created in hot ion sources with internal energies that can exceed the binding energy substantially. Very hot aluminum clusters will dissociate spontaneously. This process will happen on a very short time scale within the transport from the source to the ring or within the first revolutions inside the CSR. Afterwards the clusters are less likely to dissociate. Another process the clusters can undergo is cooling by photon or electron emission. This section will discuss three channels involved in the cooling process by photon emission.

5.4.1 Recurrent fluorescence

The Al_4^- ions are produced in a hot sputter ion source. Hence, a lot of excited states (electronic and vibrational) will be populated. The relaxation process of small molecules has been studied extensively by multiple pump-probe experiments and it is known that internal conversion (IC), which is the intramolecular process by which energy from electronic excitation is distributed to vibrational modes, proceeds on the order of picoseconds or faster (Radloff et al. 1997). There is also the inverse process, which is called inverse internal conversion (IIC). Here, energy is transferred from vibrational modes of the ground state back to electronic excited states, which is followed by the emission of photons, referred to as recurrent fluorescence (RF). The schematic for this process is shown in Fig. 5.2.
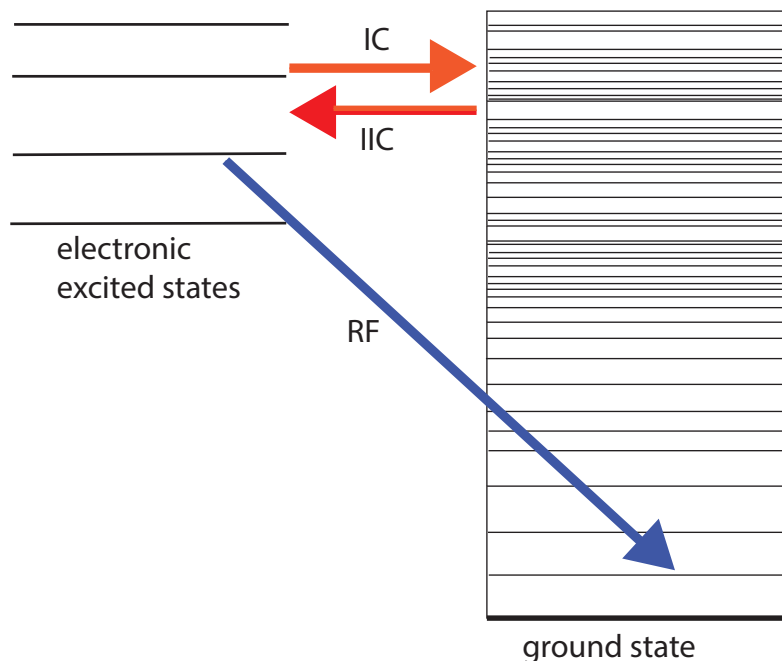
Figure 5.2: Schematic energy diagram for recurrent fluorescence (RF). The RF is shown by the blue arrow and internal conversion (IC) as well as inverse internal conversion (IIC) is shown by the red arrow. The figure was adapted from Ebara et al. 2016.

In table 5.1 $^2A_{2u}$ is the lowest excited electronic state state with an energy between $0.12\,\mathrm{eV}$ and $0.153\,\mathrm{eV}$ (depending on the theoretical method that was chosen). Since RF photons appear on the time scale of μs (see Ebara et al. 2016), fast cooling rates are expected to be seen in the transfer beamline already and in the first couple of revolutions of the stored Al_4^- in the ring. However, once the cluster's internal energy is below the level of the first electronic excited level, RF stops and electronic excited states are not expected to be populated any more. The rate for recurrent fluorescence of the first electronically excited state can be calculated following the reasoning in Chandrasekaran et al. 2014. The rate $k_{\mathrm{RF}}(\epsilon)$ for the RF process is given by the formula

$$k_{\mathrm{RF}}(\epsilon) = A_1(E_1)\frac{\rho(\epsilon - E_1)}{\rho(\epsilon)}, \tag{5.35}$$

where $A_1(E_1)$ is the Einstein coefficient for the transition from the first electronic state to the ground state and E_1 is the energy difference between both states. ρ is the density of states. Vibrational modes of the electronically excited state and the electronic ground state are assumed to be the same and contributions from higher-lying electronic states to the level densities are considered to be very small and will be neglected.

5.4.2 Internal vibrational redistribution

First concepts (Rice and Ramsperger 1927 and Kassel 1928) involving the flow of internal energy in a molecule for the theoretical treatment of unimolecular reaction rates are almost a century old. Combined with the transition state theory, these first concepts led to the very successful Rice-Ramsberger-Kassel-Marcus (RRKM) (RRKM) approach (Marcus 1952) for chemical reactivity. It is based on the statistical distribution of vibrational energy among the active degrees of freedom. Predictions made by the RRKM approach are based on the improbability of finding a high enough fraction of the energy located in specific coordinates prior to the reaction. Hence, it is a probabilistic approach that handles IVR as happening much faster than the reaction time scale, without requiring any knowledge of underlying quantum mechanical details or physical understanding of the process.

Intramolecular dynamics including nonradiative vibronic transitions and IVR have been discussed in Harris 1963. Although there had been numerous experiments on various molecules, during this time, it could not be shown how radiationless vibronic or vibrational transistions occured in isolated molecules. Bixon and Jortner 1968 showed the necessity of such transitions combined with arguments made on existing experimental data and a theoretical explanation on vibronic coupling, which are enabling IVR, is demonstrated. The main result from this work is the implentation of Fermi's Golden Rule, which relates the rate Γ of the vibronic transition to the density of states ρ and the coupling strength V^2:

$$\Gamma = \frac{2\pi}{\hbar}V^2\rho. \tag{5.36}$$

There have been various more recent experimental and theoretical works (e.g. Nesbitt and Field 1996 and Karmakar and Keshavamurthy 2020) on the IVR process. The energy flow in molecules has become an recurring question in physical chemistry (Karmakar and Keshavamurthy 2020).

Experimental studies of IVR mostly employ laser excitation to specific spectroscopically accessible bright states that have access to many vibrational background modes. The occurance of IVR is explained by the splitting of absorption lines into multiplets, which is shown by the coupling to vibrational states that are energetically close to the initial state. Measuring the multiplet width gives access to the time scale and therefore also the depletion rate of bright states. In a more recent study, the IVR process has been studied in real-time by a pump-probe experiment using ultrafast laser pulses. The measured IVR time scale was on the order of picoseconds to nanoseconds (Makarov, Malinovsky, and Ryabov 2012), because highly excited states were studied that were adressed by laser light. Note that experimental results are often unlikely to scale with simple rules as following the density of states (Gruebele and Wolynes 2004), which motivates the inclusion of effects such as dynamical traps (Manikandan and Keshavamurthy 2014) and further development of theoretical tools (Karmakar and Keshavamurthy 2020).

At the CSR, the IVR process is studied under very different conditions, allowing access to very long storage times and low temperatures. Having the stored ions at cryogenic temperatures, IVR is usually considered insignificant because of the low density of states. Even so, for understanding the cooling dynamics of molecules in the interstellar medium, the IVR process is still important. Without collisions and at low temperatures, the main cooling mechanism for the isolated molecules in interstellar space is vibrational radiative cooling. For the case of symmetric molecules, vibrational cooling down to their vibrational ground state is only possible in the presence of IVR, since otherwise energy would be 'trapped' in IR inactive modes.

Earlier works on radiative cooling have taken into account both extreme cases, where IVR is either negligible, or much faster than radiative cooling (Aviv et al. 2011, Kafle et al. 2015 and Chandrasekaran et al. 2014). A recent work on anionic carbon clusters stored in the DESIREE cryogenic storage ring showed 'ultra-slow' radiative cooling on a time scale of seconds. Additionally, it was shown that the cooling rate depends on the internal energy of the clusters, and it was concluded that IVR takes place and is probably very fast, because of a better fit of the data by a model including instantaneous IVR (Bull et al. 2019 and Stockett et al. 2020).

We will have a closer look on the role of IVR in the following section.

5.4.3 Vibrational cooling

Vibrational cooling refers to the energy dissipation of the molecule through the emittance of a photon, which is often referred to as IR radiation, as this is the wavelength it is typically emitted with. Infrared radiation covers the wavelength range from $700\,\mathrm{nm}$ up to $1\,\mathrm{mm}$. Within this range most vibrations that might occur, are covered.

A first approach towards understanding vibrational cooling is to calculate the level density for a given set of vibrational excitations. The results from calculating vibrational cooling rates will be shown after the introduction of the methods to estimate the level densities. One powerful tool to start with, is the Beyer-Swinehart algorithm named after the inventors (a detailed description of the employment of this algorithm can be found in Hansen 2013). It is a numerical method with the idea of harmonic oscillators being independent, where the energy can then be written as a sum of energies over individual oscillators. The level density is defined as the numbers of levels per unit of the total vibrational energy, and it is a convolution of the individual degrees of freedom. For a set of n harmonic oscillators ω_i that have a total level density of $\rho(E, n)$, it is possible to find the total level density for an $n+1$ oscillator system, where an oscillator at the frequency ω_{n+1} has been added:

$$\rho(\epsilon, n+1) = \int_0^\epsilon \rho(\epsilon - E, n) \left(\sum_{k=0}^\infty \delta(E - k\hbar\omega_{n+1}) \right) dE. \tag{5.37}$$

The sum runs over k to infinity and it calculates the level density of the $n+1$ oscillator. $\rho(\epsilon - E, n)$ is only non-zero, if k is less than or equal to $[\epsilon/\hbar\omega_{n+1}]$. Integrating over E
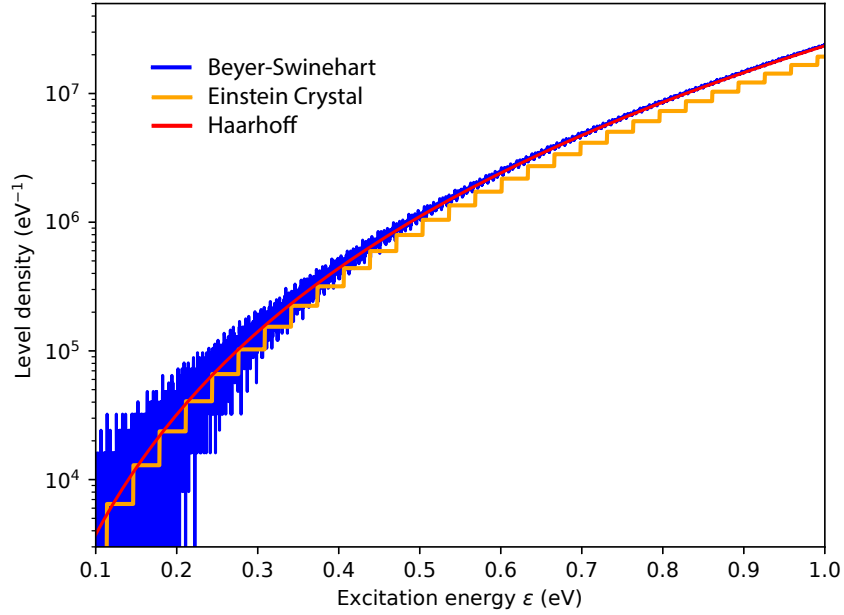
Figure 5.3: Calculated density of states $\rho(\epsilon)$ of Al_4^-. The Beyer-Swinehart, Einstein Crystal and Haarhoff models have been applied. All curves show an asymptotic behavior (see Hansen 2008).

gives a discrete sum over all possible energy segments:

$$\rho(\epsilon, n + 1) = \sum_{k=0}^{[\epsilon/\hbar\omega_{n+1}]} \rho(\epsilon - k\bar{\omega}_{n+1}, n). \tag{5.38}$$

It is a recurrence relation, initialized by calculating the level density of the first oscillator as the sum of δ functions at multiples of the energy quantum. We have applied the Beyer-Swinehart algorithm to the Al_4^- molecule and the level density is shown in Fig. 5.3.

In case of degenerate oscillators, meaning that all vibrational frequencies are identical, another approach (taken from Hansen 2013) is possible, which is the so-called Einstein crystal method. It is a sum of δ functions, which are located at multiples of the quantum energy. In case of the vibrational level energies of Al_4^-, this approach seems to be unjustified. Nevertheless, we have made a rough assumption of taking the mean vibrational frequency $\hbar\omega$ of all vibrations $\sim 31\,\mathrm{meV}$ with $s = 6$ identical oscillators and applied the formula

$$\rho(\epsilon) = \frac{1}{\hbar\omega} \frac{\left(\frac{\epsilon}{\hbar\omega} + s - 1\right)!}{\left(\frac{\epsilon}{\hbar\omega}\right)!(s - 1)!}. \tag{5.39}$$

The result of this calculation is also shown in Fig. 5.3. It follows the exact numerical

approach of the Beyer-Swinehart algorithm quite well at low energies, but deviates at higher energies. Another approach to describe the density of vibrational energy levels numerically is given in Haarhoff 1964b. Various approximations have been employed, which give an easy applicable expression to calculate the shape of the level density.

$$\rho(\epsilon) = \left(\frac{2}{\pi n}\right)^{1/2} \frac{(1 - 1/12n)\lambda}{h\bar{\omega}(1+\eta)} \left[\left(1 + \frac{\eta}{2}\right)\left(1 + \frac{2}{\eta}\right)^{\eta/2}\right]^n \left[1 - \frac{1}{(1+\eta)^2}\right]^{\beta_0}, \quad (5.40)$$

where n is the number of vibrational modes, $\eta = \epsilon/\epsilon_z^0$ and $\epsilon_z^0 = \sum_i h\omega_i/2$. $1/\lambda = \prod_i(\omega_i/\bar{\omega})$ with $\bar{\omega}$ being the average vibrational frequency and $\epsilon = h\omega$. β_0 is given by

$$\beta_0 = \left[(n-1)(n-2)\alpha_2 - n^2\right], \quad (5.41)$$

where

$$\alpha_2 = \frac{\sum_i \omega_i^2/n}{\bar{\omega}}, \quad (5.42)$$

which was taken from Haarhoff 1964a. The resulting curve is also shown in Fig. 5.3 and matches the Beyer-Swinehart algorithm very well, while still being continuous.

5.4.3.1 Harmonic Cascade Model

A first approach to calculate the decay rate of delayed electron emission is done by applying the harmonic cascade model. In this model it is assumed that vibrations can be treated as harmonic oscillators, which also means that the different vibrational modes decay seperately. Thus, the vibrational energy levels $E_i(\nu)$ of each vibration are equally spaced

$$\epsilon_i(\nu) = \nu\epsilon_i \quad (5.43)$$

and it is also assumed that IR transitions only occur between neighboring levels. For ν_i being the occupation of vibration i, the state of the system is then defined as the collection of all occupancies: $\{\nu_i\}$, which have the energy

$$\epsilon(\{\nu_i\}) = \sum_i \nu_i\epsilon_i. \quad (5.44)$$

Within this model it is assumed that the rate for IVR is much faster than the rate of radiative cooling (IVR will be treated as instantaneous). The energy levels are grouped in bins with a width ΔE, which is also the same bin width that is used to calculate the density of states. Another assumption is made by neglecting IVR between states from different bin widths. Now the decay rate $k(\epsilon, i)$ via IR emission from the i-th vibrational mode is given by (see Chandrasekaran et al. 2014; Bull et al. 2019 and Stockett et al. 2020):
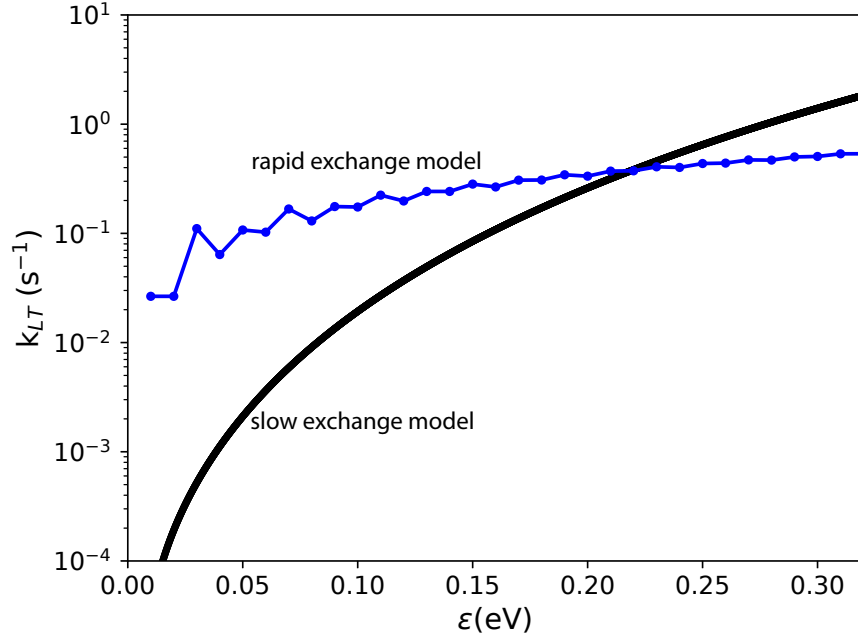
Figure 5.4: Calculated decay rate in dependency of the internal excitation ϵ of Al_4^-. The blue curve shows the calculated cooling rate in the case of IVR being very fast (assumed instantaneous) and the black curve shows the case of IVR being very slow, and effectively limiting the cooling process.

$$k(\epsilon, i) = \sum_m k_{1,0}^i \frac{\rho(\epsilon - m\epsilon_i)}{\rho(\epsilon)}. \tag{5.45}$$

$k_{1,0}^i$ is equal to the inverse lifetime of the $\nu = 1 \to 0$ transition of the i-th vibration. The above equation (5.45) is based on the rate of decay for the $\nu \to \nu - 1$ transition being given by $k_{\nu,\nu-1}^i = \nu k_{1,0}^i$. The sum over all different vibrational modes yields the total decay rate:

$$k(\epsilon) = \sum_i k(\epsilon, i). \tag{5.46}$$

The result of this calculation is shown in Fig. 5.4. At very low energies ($\epsilon < 34 \, \text{meV}$) the rate is small, but with energies above the vibrational mode B_{2u}, with the strongest IR intensity at $\approx 34 \, \text{meV}$, we observe a faster decay rate. We will refer to this model as *rapid exchange model*. The term *rapid* is related to the assumption of fast IVR.

Let's look at the opposite case. The mathematical description and idea (as well as the name) was given by our collegue Yoni Toker from the Bar Ilan University in Israel (Toker 2022). This case will be called slow exchange limit, where we assume IVR to take place and to take longer than radiative cooling

$$k_{\text{ivr}} \ll k_{\text{IR}}, \tag{5.47}$$

where k_{ivr} denotes the rate for IVR. If we assume a state with an energy ϵ having various different vibrational modes $\{\nu_i\}$ occupied, a state, which is able to cool down has to have at least one IR active mode with an occupation larger than 1. The density of such states is then given by $\rho_c(\epsilon)$ and the states, which can not cool down are denoted by $\rho_{nc}(\epsilon)$. The total density of states is then given by $\rho = \rho_c + \rho_{nc}$. In the slow exchange limit, the cooling rate is calculated with the formula

$$k_{\text{cooling}} = k_{\text{ivr}} p_c, \tag{5.48}$$

and p_c denotes the probability that an individual state can cool

$$p_c(\epsilon) = \frac{\rho_c(\epsilon)}{\rho} = 1 - \frac{\rho_{nc}(\epsilon)}{\rho_c}. \tag{5.49}$$

Here ρ_{nc} is calculated as the density of states of the molecule without the strongest IR active mode. Using $k_{\text{ivr}}(\epsilon) = B\rho(\epsilon)$, and B being a proportionality constant, gives:

$$k_{\text{cooling}} = B \cdot \rho(\epsilon) \cdot \left(1 - \frac{\rho_{nc}(\epsilon)}{\rho(\epsilon)}\right) = B \cdot (\rho(\epsilon) - \rho_{nc}(\epsilon)) \tag{5.50}$$

The result of the slow exchange model is shown in Fig. 5.4. For this figure the proportionality constant has been taken from the later analysis and is extracted from the fit in Fig. 7.12 and is $B = 1.3 \times 10^{-5}$ s^{-1} (for more details see Sec. 7.9). Presently, the energy dependence of the two cases is more relevant than the absolute scale.

5.4.4 Rotational excitation

The aluminum molecules are produced in a hot ion sputter source and in this section an estimate on the rotational angular momentum of the molecules leaving the source is made. From the Maxwell-Boltzmann distribution the most probable energy $\langle E \rangle$ for the ions at temperatures of 3000 K is given by

$$\langle E \rangle = \frac{3k_B T}{2} \cong 0.38 \, \text{eV}. \tag{5.51}$$

The rotational energy E_{rot} of a rigid diatomic molecule is calculated with

$$E_{\text{rot}} = \frac{\hbar^2}{2I} J(J+1) = B \cdot hc \cdot J(J+1), \tag{5.52}$$

where $B = h/(8\pi^2 cI)$ is the rotational constant of the molecule and $J = 0, 1, 2 \ldots$ is the quantum number that designates the energy level. I is the inertia tensor (in *Cartesian coordinates* x,y,z)

$$I = \begin{bmatrix} I_{xx} & I_{xy} & I_{xz} \\ I_{yx} & I_{yy} & I_{yz} \\ I_{zx} & I_{zy} & I_{zz} \end{bmatrix}, \tag{5.53}$$
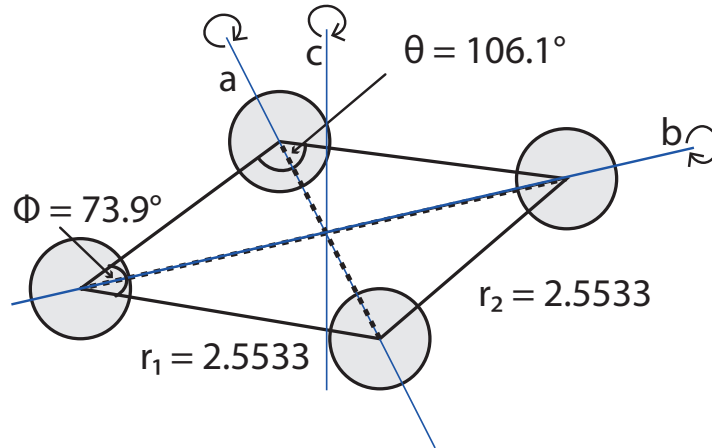
Figure 5.5: Rotational axis of the Al_4^- molecule. The bond lengths $r_1 = r_2$ are given in Å.

which can be transferred to *molecule based coordinates*, with axes that are labeled a, b and c. The above matrix can then be decomposed into a diagonal matrix:

$$I = \begin{bmatrix} I_a & 0 & 0 \\ 0 & I_b & 0 \\ 0 & 0 & I_c \end{bmatrix}. \tag{5.54}$$

The labeling of the molecule-based coordinates is done such that

$$I_a < I_b < I_c \tag{5.55}$$

is fulfullied. For the case of the Al_4^- molecule, the molecule-based coordinates are shown in Fig. 5.5. The moments of inertia for the respective rotational axis are then calculated to

$$I_a = 2 \cdot m_{Al} \cdot \left[\cos(\theta/2) \cdot r_1\right]^2 = 2.112 \times 10^{-45} \text{kg m}^2, \tag{5.56}$$

$$I_b = 2 \cdot m_{Al} \cdot \left[\cos(\phi/2) \cdot r_1\right]^2 = 3.732 \times 10^{-45} \text{kg m}^2, \tag{5.57}$$

$$I_c = 2 \cdot m_{Al} \cdot \left[\cos(\theta/2) \cdot r_1\right]^2 + 2 \cdot m_{Al} \cdot \left[\cos(\phi/2) \cdot r_1\right]^2 = 5.842 \times 10^{-45} \text{kg m}^2. \tag{5.58}$$

The rotational kinetic energy operator H_{rot} for a non-linear polyatomic molecule is expressed with

$$H_{\text{rot}} = \frac{1}{2} \left(\frac{J_a^2}{I_a} + \frac{J_b^2}{I_b} + \frac{J_c^2}{I_c} \right). \tag{5.59}$$

The components of the quantum mechanical angular momentum operators J_a, J_b and J_c will not be given in this section. Instead, a simplification will be made, where

$I_a = I_b = I_c$ is assumed. In case of a molecule, where the three principal moment of inertia values are identical, the molecule is called a *spherical top*, with

$$H_{\text{rot}} = \frac{J^2}{2I}. \tag{5.60}$$

The eigenfunctions of H_{rot} are the ones from J^2 and the related energies are given by

$$E = \frac{\hbar^2 J(J+1)}{2I} = B \cdot hc \cdot J(J+1). \tag{5.61}$$

B is calculated by the mean value of the three principal moments of inertia $(\bar{I})$

$$B = \frac{h}{8\pi^2 c \bar{I}} \approx 0.072 \text{ cm}^{-1}. \tag{5.62}$$

The energy $\langle E \rangle = 0.38 \text{ eV}$ then corresponds to an angular momentum quantum number of $J \approx 200$. A large number of rotational levels will be populated.

The previous section shows that the Al_4^- molecules will occupy large angular momentum quantum numbers. Consequently, the role of rotations to delayed electron detachment is described. The following reasoning and description is taken from J. Andersen, Bonderup, and Hansen 2002. For clusters, most of the angular momentum is typically stored in collective rotation. With the moment of inertia being so large, the spacing of the rotational levels is rather small. Therefore it is unlikely that a significant amount of angular momentum is transfered from rotation to internal excitation (electronic or vibrational) because this excitation of an internal state with large angular momentum would have to take out a substantial amount of energy. Both properties, the internal and rotational energy, are assumed as serparately conserved.

Generally it is assumed that electron attachment or detachment only leads to small changes in angular momentum or moment of inertia, which is why the rotational energy is almost unchanged (J. Andersen, Bonderup, and Hansen 2002). Rotations are often referred to as spectators in regard of delayed electron detachment (Kafle et al. 2015). Consequently, we will ignore rotational excitation in our analysis.

5.5 Delayed fragmentation and emission from metal cluster anions

The macroscopic process of thermionic emission of electrons from hot metals (Dushman 1930) is comparable to the statistical process of delayed electron emission for cluster anions (J. Andersen, Bonderup, and Hansen 2002), which were studied for initially hot stored cluster ions (see J. U. Andersen et al. 2003, L. Andersen, Heber, and Zajfman

2004, J. Andersen, Bonderup, and Hansen 2002 and Concina, Lépine, and Bordas 2017 as examples). Additionally, photon-induced delayed electron emission of clusters has been measured by Toker et al. 2007 and Nielsen et al. 2003. In principal, delayed electron emission occurs when the amount of energy from several degrees of freedom is transferred into the electronic degree of freedom (Nielsen et al. 2003 and Hansen et al. 2001). In the following subsections the statistical approach for temperature induced delayed electron emission will be given and a way to model photon-induced electron emission will be introduced.

Starting with the production in hot sources, where often sputter sources are used as the standard for cluster and molecule production, the clusters occupy all kinds of highly excited electronic, vibrational and rotational states, which leads to thermal emission in the following process of storing the clusters. Different kinds of thermal emissions of electrons, atoms and small molecules have been studied previously in experiments (for more details: J. U. Andersen et al. 2003, L. Andersen, Heber, and Zajfman 2004, J. Andersen, Bonderup, and Hansen 2002). Typically the delayed emission of very hot ions is observed on very short time scales, while at longer time scales radiative cooling becomes more dominant as the probability for emission goes down with longer storage times. In the following text a short theoretical description is presented.

5.5.1 Temperature related cluster dissociation: Statistical description of electron emission

The approach discussed in the following is based on the arguments made in J. Andersen, Bonderup, and Hansen 2002. The decay rate is linked to the reverse process of particle absorption by detailed balance for the case of particle emission from a cluster in statistical equilibrium. In order to get the rate constants k, the sum of all transition rates over their final states is taken, and the average over the initial states is needed. Having the number of accessible states given by the level density ρ, the resulting statistical balance can be written as

$$k_{\text{decay}}\rho_{\text{parent}} = k_{\text{formation}}\rho_{\text{products}}.$$ (5.63)

The rate constant $k(E, \epsilon)$ for electron emission in the energy interval $(\epsilon, \epsilon + \mathrm{d}\epsilon)$ can be expressed as (J. Andersen, Bonderup, and Hansen 2002)

$$k(E,\epsilon)d\epsilon = \frac{2m}{\pi^2\hbar^3}\sigma_c(\epsilon)\epsilon\frac{\rho_d(E - E_a - \epsilon)}{\rho_p(E)}d\epsilon.$$ (5.64)

m denotes the electron mass, parent and daughter level densities ρ have the index p and d, respectively. The electron binding energy is denoted by E_a, and the internal excitation of the parent is given by E. For the derivation of the above formula, it is assumed that the kinetic energy of the electron ϵ is small, such that $ln\rho(E - E_a - \epsilon)$ is expanded to first order at $\epsilon = 0$.

The microcanonical temperature T_m for a system at excitation energy E with level density $\rho(E)$ is written as

$$\frac{1}{k_b T_m} = \frac{d}{dE} ln\rho(E),\qquad(5.65)$$

with k_B denoting the Boltzmann constant. Combining this equation with equation (5.64), the expression for the emission rate of electrons is

$$k(E,\epsilon)d\epsilon = \frac{2m}{\pi^2\hbar^3}\frac{\rho_d(E - E_b - \epsilon)}{\rho_p(E)}\sigma_c(\epsilon)\epsilon e^{-\epsilon/k_B T_d}d\epsilon.\qquad(5.66)$$

5.5.2 Total electron emission rate

The total emission rate $I(t)$ of a cluster is calculated by convoluting the energy distribution $g(E,T)$ with the rate constant $k(E)$ as it was described in Hansen et al. 2001

$$I(t) = \int dE k(E) g(E,t).\qquad(5.67)$$

Assuming that all interactions of this cluster with other clusters and the surrounding can be ignored, the excitation energy E is conserved and the clusters decay independently. (Note that this assumption also neglects absorption and emission from radiation.) This results in a alternated shape of the energy distribution $g(E,t)$, which is expressed in

$$I(t) = \int dE k(E) g(E,0) e^{-k(E)t}\qquad(5.68)$$

With $k(E)$ rapidly increasing, $k \cdot e^{-k(E)t}$ will have a sharp maximum at the energy E_m for $k = 1/t$. This gives the typical $1/t$ dependence of $I(t)$ for the decay of molecules with a broad energy distribution. From the integral, a gaussian approximation of the maximum yields the peak width, which is time-dependent. Various studies have confirmed the $1/t$ power law behavior (J. U. Andersen et al. 2003, Fedor et al. 2005, Hansen et al. 2001, J. Andersen et al. 2001).

5.5.3 Radiative cooling correction

Following the arguments in J. U. Andersen et al. 2003, the emission of low-energetic photons act in a way to continuously cool the cluster, especially for the case of IR radiation by vibrational de-excitation. The radiated power P_r varies slowly with temperature, in contrast to the exponential dependence of the dissociation rate on the temperature. Earlier experiments (J. U. Andersen et al. 2003) have observed this effect by quenching of radiative cooling in a narrow time range. Consequently, the radiated

power variation has been ignored and then cooling can be expressed in first order of t/τ_c (cooling time τ_c):

$$T(t) = \frac{T}{(1 + t/\tau_c)} \qquad \text{with} \quad \frac{1}{\tau_c} = \frac{P_r}{CT_m}. \tag{5.69}$$

Here C denotes the microcanonical heat capacity. E and T_e denote the initial values of energy and effective decay temperature in the finite heat bath correction (see J. Andersen, Bonderup, and Hansen 2002 for more details)

$$T_e = T - \frac{E_a}{2C} - \frac{E_a^2}{12C^2T}, \tag{5.70}$$

with E_a denoting the barrier energy for emission and T denoting the temperature of the molecule before the decay. The advantage of choosing these variables is that instead of a time variation in the effective temperature T_e, the combination of both above equations can be expressed as reduction of the decay rate with time related to radiative cooling. Multiplying this factor $(1 + t/\tau_c')^{-1}$ (note that τ_c' to τ_c is slightly different becaues of the finite-heat-bath correction $\tau_c' = (T_e/T(0))\tau_c$) with the denominator in the exponent of the Arrhenius expression ($k = \nu \cdot \exp(-E_a/k_BT)$) gives:

$$I(t) \simeq g(E_m)C(E_m) \int dT_e \nu \exp\left(\frac{E_a(1 + t/\tau_c')}{k_BT_e}\right) \times \exp\left(-\nu \int_0^t dt' \exp\left[-\frac{E_a(1 + t')/\tau_c'}{k_BT_e}\right]\right)$$

$$= g(E_m)C(E_m) \int dT_e k(T_e)e^{-Gt/\tau_c'} \times \exp\left(-k(T_e)G^{-1}\tau_c'\left(1 - e^{-Gt/\tau_c'}\right)\right). \tag{5.71}$$

The slowly varying energy and heat capacity has been extracted from the integral by changing the variables from E to T_e. The so-called Gspann parameter

$$G = \frac{E_a}{k_BT_e} \tag{5.72}$$

changes more slowly with temperature in comparison with k, and is often referred to as constant. An effective decay temperature $T_{e,m}$ with an energy E_m may then be introduced and is defined as the maximum of the integrand

$$k(T_{e,m}) = \left[G^{-1}\tau_c'(1 - \exp(-Gt/\tau_c'))\right]^{-1} \tag{5.73}$$

Combining both formulae gives the following expression:

$$I(t) = \frac{1}{\tau(\exp(t/\tau) - 1)}g(E_m)C(E_m)\frac{k_BT_{e,m}^2}{E_a}, \tag{5.74}$$

with $\tau = \tau_c'/G$. For very short times $t \ll \tau$, at which radiative cooling is not yet important, the equation (5.74) gives the expected $1/t$ power law decay. For time scales, which are on the order of τ, the total emission rate is exponentially surpressed by radiative cooling. The last three factors can be expressed by $(t/\tau)^\delta$.

5.6 Photon-induced delayed electron emission

The process of clusters or molecules being illuminated by a short (nanosecond) laser pulse and emitting electrons on a time scale of up to several hundreds of microseconds is called photon-induced delayed electron emission and is observable on much longer time scales than the temperature related delayed electron emission. This process has been studied in previous works as in Breitenfeldt et al. 2018.

A photon, which is high enough in energy, will lead to direct emission of an electron for a certain part of the ion distribution. As discussed in the previous sections, the strong coupling between electronic and vibrational states may cause an energy transfer to the vibrational modes of the ion. The electron is only detached if enough energy is transferred back to the electronic degree of freedom. Since this is a statistical process, and this one degree of freedom is not likely to have high amounts of energy stored, electron emission is observable for a rather long time scale of up to hundreds of microseconds after photon absorption. Therefore, the energy of the absorbed photon is stored in the ion's vibrational modes. Now, the time correlation of the delayed electron detachment rate after the laser irradiation can be linked to the internal excitation energy of the cluster before the photon absorption. Consequently, hotter ions will emit the electron at earlier times than colder ions. The photon-induced delayed electron emission rate can be used as a temperature probe of the stored ions.

The shape of delayed electron emission can be described similarily as in Toker et al. 2007 for Al_4^- and Nielsen et al. 2003 for bio molecules. A cluster with the internal energy ϵ_i is defined by a canonical ensemble with the temperature T_i and the distribution is estimated by a Gaussian

$$g(\epsilon, \epsilon_i) = \rho(\epsilon)\exp\left(\frac{-\epsilon}{k_B T_i}\right) \simeq \frac{1}{\sqrt{2\pi\sigma^2}}\exp\left((\epsilon - \epsilon_i)^2/2\sigma^2\right) \qquad (5.75)$$

with

$$\sigma = \sqrt{k_B C} \cdot T_i. \qquad (5.76)$$

Here, $\rho(\epsilon)$ is the density of states and ϵ_i is the energy (where the microcanonical temperature is $T(\epsilon_i) = T_i$). After absorbing a photon ($h\nu$), the distribution is shifted by the photon energy. The delayed emission curve $I_i(\tau)$ can be written as

$$I_i(\tau) = \int d\epsilon N(t_i) P_{ph} g(\epsilon, \epsilon_i + h\nu) k(\epsilon)\exp\left(-k(\epsilon)\tau\right). \qquad (5.77)$$

$N(t_i)$ denotes the number of ions in the trap or storage ring at times t_i, τ is the time after the laser pulse, and P_{ph} is the probability of the ion to absorb a photon.

A useful method, which will also be utilized later for the analysis, is the calculation of the delayed electron emission rate. The energy in the cluster after photon absorption is given by $\epsilon_T = \epsilon + \epsilon_{ph}$, with ϵ_{ph} being the photon energy. The rate for electron emission is $k(\epsilon_T)$. E_a is the activation energy for electron emission and $k(\epsilon_T) = 0$ for the case
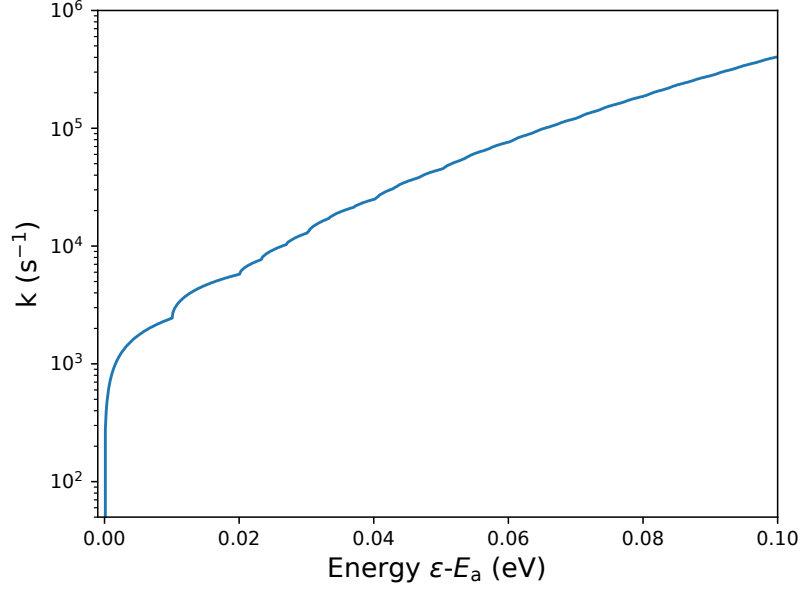
Figure 5.6: Calculated delayed emission rate $k(\epsilon_T)$ as a function above activation energy. The rate was calculated for $E_a = 2.21 \, \text{eV}$ and $\alpha_p = 18 \text{Å}^3$.

that $\epsilon_T \leq E_a$. From detailed balance and given that $\epsilon_T > E_a$, $k(\epsilon_T)$ can be written (as describend in Hansen 2013):

$$k(\epsilon_T) = \frac{2m_e}{\pi \hbar^3} \sqrt{\frac{2\alpha_p q_e^2}{4\pi\epsilon_0}} \frac{1}{\rho_p(\epsilon_T - E_a)} \int_0^E \sqrt{\epsilon'} \rho_d(\epsilon_T - E_a - \epsilon') d\epsilon'. \qquad (5.78)$$

Here q_e and m_e denote the electron charge and mass, α_p is the polarizability, ϵ' is the energy of the emitted electron, ρ_p is the density of states of the parent Al_4^- ion and ρ_d is the density of states of the daughter Al_4 neutral (ρ_d has been calculated in the same way as for the anionic case based on the vibrational level energies given by our collegue Mark Iron using the same computational methods Iron 2022). In Fig. 5.6 the calculated delayed emission rate $k(\epsilon_T)$ is shown for energies above the activation energy $E_a = 2.21 \, \text{eV}$ and for $\alpha_p = 18 \text{Å}^3$. The first two increases in delayed emission rate correspond to the first two energy vibrational energy levels, indicating a threshold behavior.

The rate of IR cooling from a state ϵ_T is denoted by $k_r(\epsilon_T)$. The probability $P(\epsilon_T, t_1, t_2)$ for ions that absorb a photon at time $t = 0$ to emit an electron in the timewindow $t_1 \leq t \leq t_2$, is defined by the formula

$$P(\epsilon_T, t_1, t_2) = \frac{k(\epsilon_T - E_a)}{k(\epsilon_T) + k_r(\epsilon_T)} \left[e^{-(k(\epsilon_T) + k_r(\epsilon_T)t_1)} - e^{-(k(\epsilon_T) + k_r(\epsilon_T)t_2)} \right]. \qquad (5.79)$$

Here, $g(\epsilon)$ denotes the internal energy distribution prior to laser absorption. In the
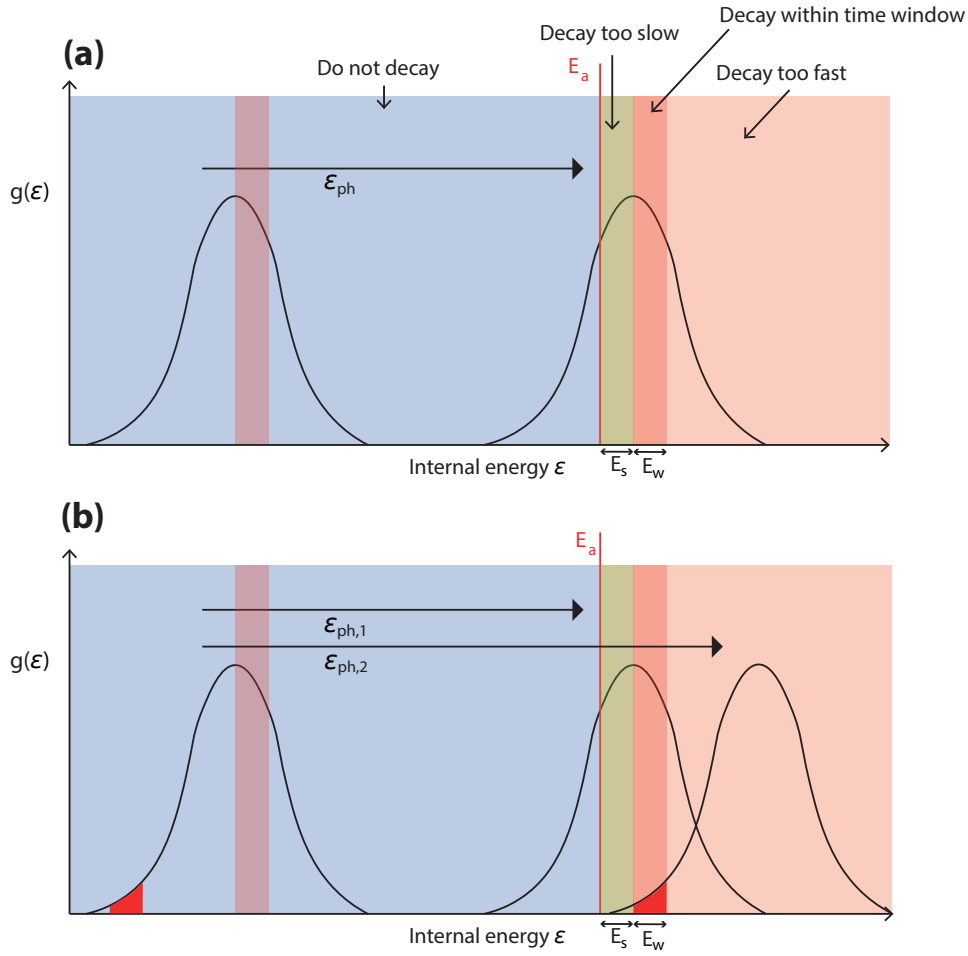
Figure 5.7: Schematic for the shift of the cluster distribution after absorption of a photon. Two cases are shown, which will be discussed in the main text.

following, the kinetic factor $I(t_1, t_2, \epsilon_{ph})$ is introduced

$$I(t_1, t_2, \epsilon_{ph}) = \int_{E_a - \epsilon_{ph}}^{\infty} g(\epsilon) P(\epsilon + \epsilon_{ph}, t_1, t_2) d\epsilon. \qquad (5.80)$$

This factor will be proportional to the number of ions, which are neutralized and then counted on the detector after photon absorption and it is used for fitting experimental data such as shown later in subsection 7.7.1.

A schematic illustration for photon-induced delayed electron emission is shown in Fig. 5.7. After absorbing a photon with the energy ϵ_{ph}, the energy distribution of the ions is shifted towards higher energies. First the upper part of Fig. 5.7 **(a)** is described. In case that the cluster's internal energy after photo-excitation is lower than the activation energy for electron emission E_a, the cluster does not decay at all. For the opposite case, decay is possible. Those ions with a high energy will decay directly via *prompt* decay and will not appear in the delayed signal. Ions, which are just above the activation

energy, will decay very slowly, in a time window, which will not be accessible by the experiment. This energy range is denoted by E_S. Finally, there are ions that decay within the time window, which is probing the energy distribution prior to the laser pulse. The energy width for this window is denoted by E_w. Both values E_S and E_w will be determined from the experimental data in subsection 7.7.1.

For the lower part of 5.7 **(b)**, we consider two different photon energies $\epsilon_{ph,1}$ and $\epsilon_{ph,2}$. For the same time windows the part of the distribution that is probed, will be different. By this method the energy distribution of the stored ions can be probed. Probing the energy distribution at different storage times, probes the temporal evolution of the internal excitation and temperature of the stored ions.

Chapter 6

Experimental Setup Al_4^-

The measurements on Al_4^- have been performed at the CSR. Fundamental properties of the CSR have already been discussed in section 1.5. In this chapter a description of the laser setup and measurement scheme, which have been developed in the course of this work, is given.

6.1 Photodetachment Setup

In order to study the cooling of stored Al_4^-, the ions are overlapped with two laser beams in a straight section of the CSR. A schematic of all relevant parts of the experiment is depicted in Fig. 3.3. For measurements on Al_4^-, two laser beams on the same alignment axis were needed. A pulsed OPO laser at $20\,\text{Hz}$ repetition rate and $\approx 1\,\text{mJ}$ pulse energies, and a CW laser (OBIS LX by Coherent) at $3.07\,\text{eV}$ (or $403\,\text{nm}$) and $100\,\text{mW}$ power, which can be modulated with up to $150\,\text{MHz}$, were used. The pulsed OPO is used as a probe laser and the CW OBIS laser is used as normalization laser. The power of the OBIS laser is recorded by a photodiode (PD), which detects a fraction of the laser beam that is reflected from a glass plate. Both lasers are merged onto one axis by a dichroic mirror. The laser setup is shown in Fig. 6.1. After leaving the laser box both beams are on the same axis. Two irises are installed without any optical elements in between in order to help reducing beam pointing of the OPO laser beam, which will be discussed in more details in 7.4. Right before entering the vacuum chambers, a beamsplitter is installed, where a small part of the beam is measured on the powermeter PM 1. The laser beams enter the experimental vacuum chamber by passing through two view ports and are overlapped to the ion beam at an angle of $\sim 1.1°$. Two mirrors are installed inside the experimental vacuum chambers that reflect wavelengths in the
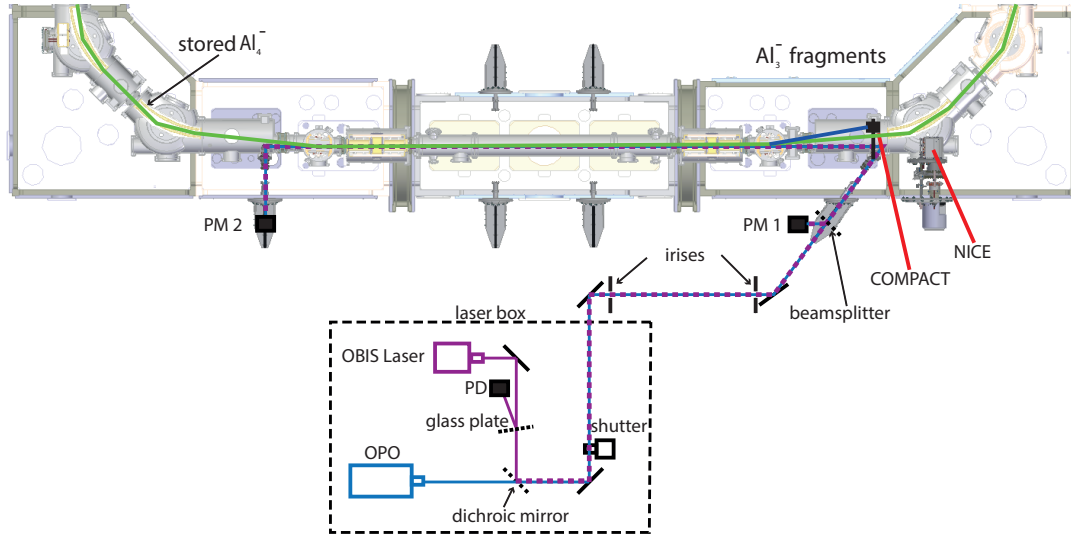
Figure 6.1: Schematic of the laser interaction section at the CSR. The CW OBIS laser (purple) and the OPO laser (blue) are aligned by a dichroic mirror and then guided towards the CSR and overlapped with the stored ion beam (green). The neutrals are collected by the NICE detector and charged fragments can be collected by the COMPACT detector.

range from $300 \, \mathrm{nm} - 2000 \, \mathrm{nm}$. After exiting the vacuum chambers the laser power is measured again on PM 2.

Al_4^- ions were produced in a sputter ion source, accelerated up to 275 keV, mass selected with a dipole magnet and injected into the ring. Following photo-absorption the two dissociation channels of Al_4^- that are accessible with our laser setup are

$$Al_4^- + h\nu \rightarrow Al_4^{-*} \rightarrow Al_4 + e^-, \tag{6.81}$$

$$Al_4^- + h\nu \rightarrow Al_4^{-*} \rightarrow Al_3^- + Al. \tag{6.82}$$
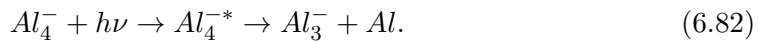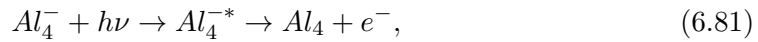
Two detectors are used. Charged fragments have a lighter mass than the stored ions and are deflected more by the parallel plate deflectors. COMPACT is a movable single particle detector that can be moved in the orbit of the Al_3^- fragments. The Al and Al_4 neutrals are detected on the MCP-based NICE detector, which is further downstream of the interaction zone. Agreeing with previous works (Aviv et al. 2011 and Kafle et al. 2015), the fragmentation events occur much less frequent than the electron emission events for the photon energies that have been studied in this work. All of the results that will be presented in the scope of this work will focus on the delayed electron emission exclusively, because this process is sensitive to the cooling times of the Al_4^- molecule and can be understood as a thermometer.

6.2 Measurement scheme

In order to monitor the cooling behavior of Al_4^- by photo-excitation and the subsequent electron emission, a dedicated measurement time-scheme was developed during the thesis. For one injection the scheme is illustrated in figure 6.2. The concept of the measurement cycle is to record photodetachment signals versus storage time and to account for various background contributions. This is achieved by switching of the lasers and power measurements. A LabVIEW NI PCIe-6612 card is used for this purpose. The timing scheme developed for the laser measurement, which is shown by black lines in Fig. 6.2, is running on the 20 Hz synchronization trigger of the OPO laser. The trigger for the OPO laser has to be running before injecting ions into the storage ring. It can not be turned on by an external trigger signal.

After sending a request pulse, the confirmation pulse by the attaclock, which controls the storage ring injection (shown in orange), is sent. By switching a fast pair of electrodes, which are called chopper, ions are able to enter the storage ring for $30\,\mu$s, 10 ms after the confirmation. The data acquisition program (shown in green) controls the injection and is recording the detected signals in steps of 10 ms. Injection and beam-on phase start as soon as the injection confirmation is sent.

All of the following lines are triggered by this confirmation pulse except for those triggers that are generated by the laser program (shown in black) and are already running before the measurement starts. It is not possible to synchronize the OPO laser with the injection easily. Within the laser program all lines are triggered on the 20 Hz synchronization trigger. The OPO laser is set on the falling flank of the synchronization trigger and the laser light is emitted right after the falling flank of this trigger. PM 1 and PM 2 record the energy of each shot that is fired and the corresponding trigger uses the falling flank of the OPO trigger. The OBIS laser is switched on before and after each laser shot for 2.5 ms typically. In order to achieve a reasonable amount of neutrals during the laser pulse, the signal is digitized with nanosecond resolution. Continuous measurement with this MCP based detector would be impossible, hence one detector acquisition step is set to 10 ms which means that the detection system has 40 ms of downtime during which no events are recorded. This allows very long monitoring of the stored ions. 5 ms prior to the laser shot, the detector is triggered.

The shutter can be opened and closed in the desired time frame. During the beam-off time the fraction of power from the OBIS laser is recorded and dark counts on the NICE detector are recorded.

The process of switching wavelengths of the OPO laser depends on the size of the step, which is taken. Larger steps require larger movement of the motors, in order to rotate the OPO crystals and it also takes some time to reach thermal equilibrium within the optics. For small steps, like they were done in this work, it takes less than 1 s. While rotating the OPO crystals, light consisting of various wavelengths may exit the OPO laser box and could possibly damage optics along the laser beam path. Undefined laser light with small variations of the set wavelength may even enter the experimental vac-

uum chamber, which demonstrates why closing a shutter for the process of wavelength change in between an injection is needed. For this work, wavelength changes were only done after an injection was completed, which was also always performed with a closed shutter.

Besides the timing program, there is also communication between the laser and the data acquisition program via TCP IP. For a complete run, which consists of multiple injections, the data acquisition is sending commands related to data storage, such as *run number*, *number of injection*, *shutter status*, *set wavenumber* and *cw measurement*, which are all written away in columns in the various laser data files. In the analysis, the recorded detector signal and the power measurements on the laser side have to be assigned to each other. Thus, gaps in the data need to be avoided, which is achieved by a semaphore-like structure, only enabling data storage of the power measurements when the detector signal is also recorded.
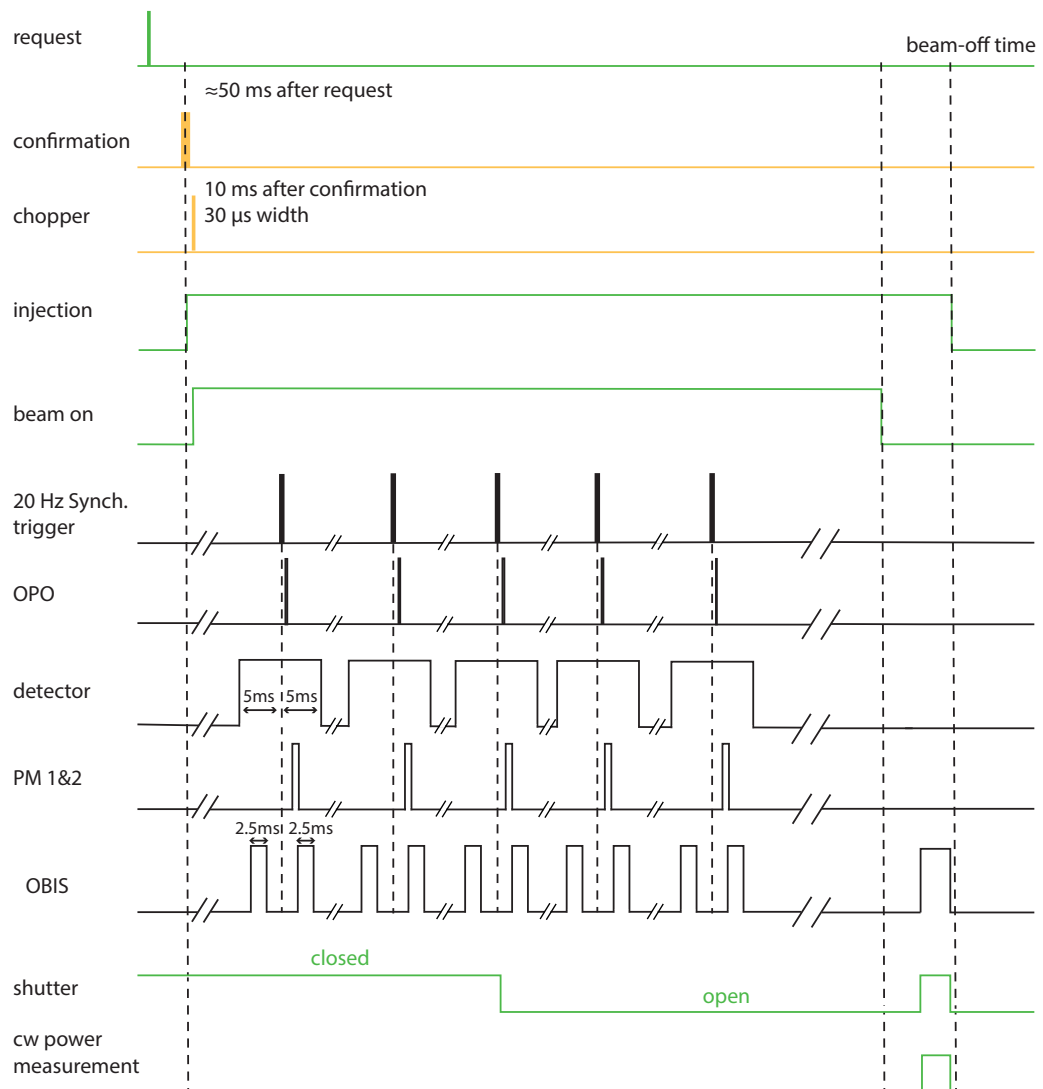
Figure 6.2: Timing scheme for the Al_4^- measurement. The green lines indicate timing generated by the data acquisition program. The orange lines show the timing done by the attaclock (timing generator) and the black lines show the timing signals generated by the laser control program. The time scheme for one complete injection is displayed.

Chapter 7

Experimental Results Al_4^-

In this chapter the analysis on the Al_4^- measurement will be presented and discussed. The main steps in order to normalize the data and to account for background contributions will be explained. In the end, the experimental results will be compared to theoretical calculations.

7.1 Time of flight spectrum

A pulsed OPO and a CW OBIS laser, which can be modulated, were installed. In the ion-laser overlap region neutrals are produced by excitation of the Al_4^-, which then either fragments or is neutralized (see equations (6.81) and (6.82)). In order to record a time of flight spectrum, the time after which the neutralized particles hit the detector, is linked to the laser pulse. As mentioned in the previous chapter, one detection step is 10 ms long and starts 5 ms prior to the laser shot and ends 5 ms after.

The ions travel at a velocity $v_{ion} = \beta c = \sqrt{\frac{2E_{kin}}{m_{ion}}}$ and observe an electromagnetic wave at a frequency

$$f_{ion} = f_{laser} \frac{\sqrt{1-\beta^2}}{1-\beta cos(\alpha)}, \tag{7.83}$$

which is Doppler shifted with respect to the photon frequency f_{laser}. The angle between both beams is $\alpha = 1.1°$. Since neutralized particles from the interaction region do not experience deflection by the electrostatic elements situated further downstream, they hit the NICE detector. Neutrals are assigned to detection times after the 5 ns short laser pulse. The overlap length for the ions and the laser is about 50 cm long. During the laser shot, the Al_4^- ions, which have a kinetic energy of 275 keV and a mass
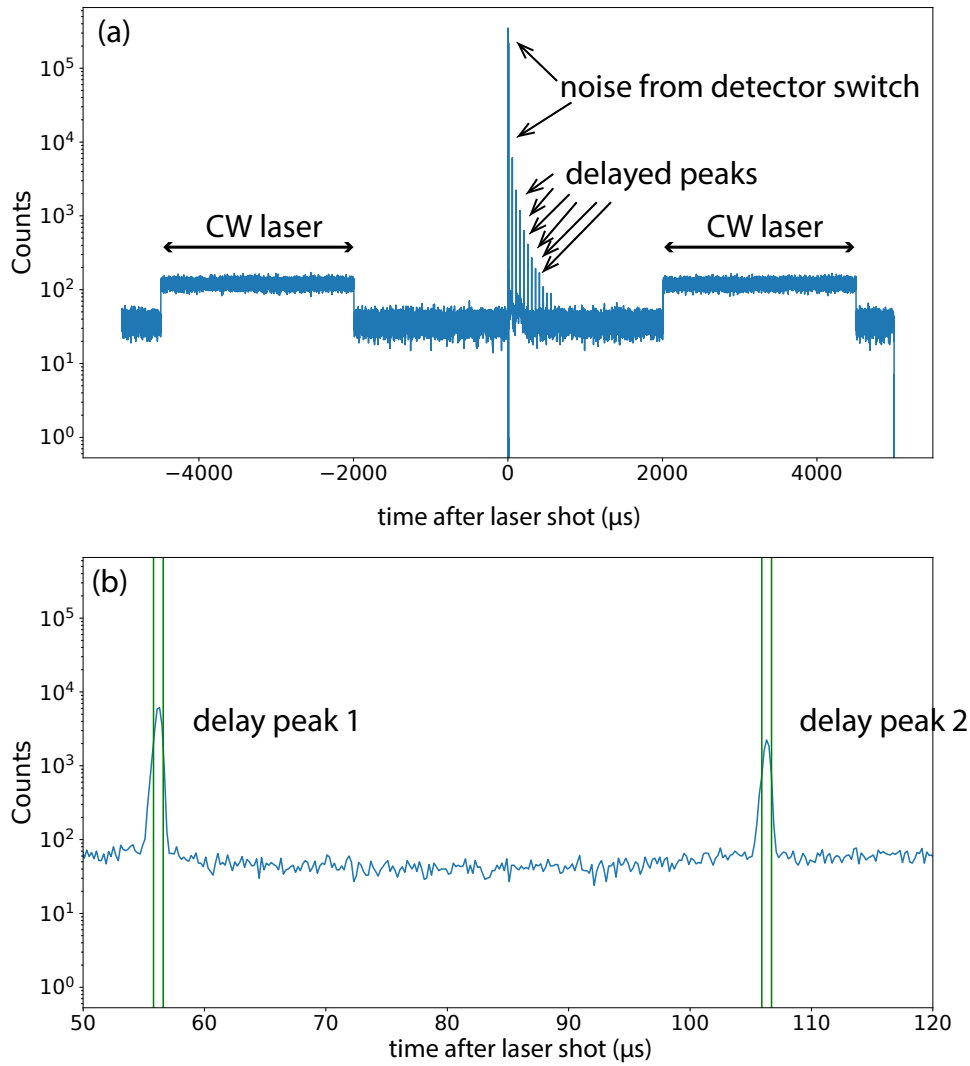
Figure 7.1: Time of flight spectrum. Counts on the NICE detector versus time after the pulsed laser shot. (a) The OBIS laser increases the yield in neutralized particles while it is on. The two large peaks at 0 are related to switching noise of the detector. Multiple peaks appear after the laser shot. Each peak is assigned to revolutions of the stored ions in the ring. (b) This shows a zoom in on the first two delayed peaks. The green lines show the time windows, in which the counts are assigned to delayed events in the data analysis.

of $m_{ion} = 108\,\mathrm{u}$, cover a distance of

$$l_{ion} = \sqrt{\frac{2E_{kin}}{m_{ion}}} \cdot t_{laser} = 0.35\,\mathrm{cm}, \tag{7.84}$$

which is small compared to the total overlap length.

After a flight time of $t \approx 5.4\,\mu$s (taking the distance of 3.8 m from the center of the overlap region to the position of the NICE detector from the technical drawing) after the laser shot, the ions are detected.

In case of the Al_4^- ions, we were mostly interested in the delayed detachment signal. The delayed detachment signal is more sensitive (see Sec. 5.6) to the internal energy distribution of Al_4^- ions than the direct events following the laser shot. The revolution time of Al_4^- in the CSR with a circumference of ≈ 35 m is about $51\,\mu$s. This value has to be added to the flight time t in order to get to the position of the first delayed detachment peak in the time of flight spectrum. In Fig. 7.1 multiple delayed detachment signals are visible.

Fig. 7.1 (a) shows all of the recorded steps from one run. The two areas of increased events during the cw laser-on phases are assigned to OBIS events. The measured counts during the OBIS laser-on phases are about a factor 3 higher than the collisional background events. Approximately $56\,\mu$s after the laser shot, the first delayed events are recorded. Every following delayed peak comes after a multiple of the revolution time. Events between the CW laser window and the pulsed laser events are assigned to collisional background detachment. The laser light intensity needs to be tuned in such a way that the statistics within the delayed counts is sufficient and that the detector is not saturated. For multiple events on the detector within a short time window, the detection system is limited by its dead time. Laser power was tuned such that after the laser shot, there is not more than 1 event per laser shot in the first delayed peak, keeping the detector system in the linear operating regime. The signal of the prompt events that occur directly after the laser is shot, would be way too high and the detector could be damaged. Consequently, the NICE detector was switched off right before the pulsed laser was fired, and switched on again shortly after. The two large peaks around $0\,\mu$s appear due to the noise of the switching.

Delayed detachment is happening as soon as the ions are hit by the laser. However, this measurement is only sensitive to those ions that detach within the field-free straight section before hitting the NICE detector. Each turn the stored ions take, the produced neutrals in the straight section hit the detector. Fig. 7.1 (b) shows the first two delayed peaks after the pulsed laser shot. The green lines indicate the time windows, where the counts are assigned to laser events. Choosing the time windows this narrow, helps increasing the background suppression. Since the pulsed laser is only fired every 50 ms, it would theoretically be possible to measure up to 1000 revolutions of the ions before another laser shot is fired. However, for all the data taken, a maximum of 15 delayed peaks were observed and for the analysis typically 10 delayed time windows were applied. For higher numbers the laser signal was not distinguishable from the background any more.

By checking the time of flight spectrum carefully, the assignment of possible mechanisms that result in neutralization is done by setting time windows ($[t_1, t_2]$) in the analysis program:
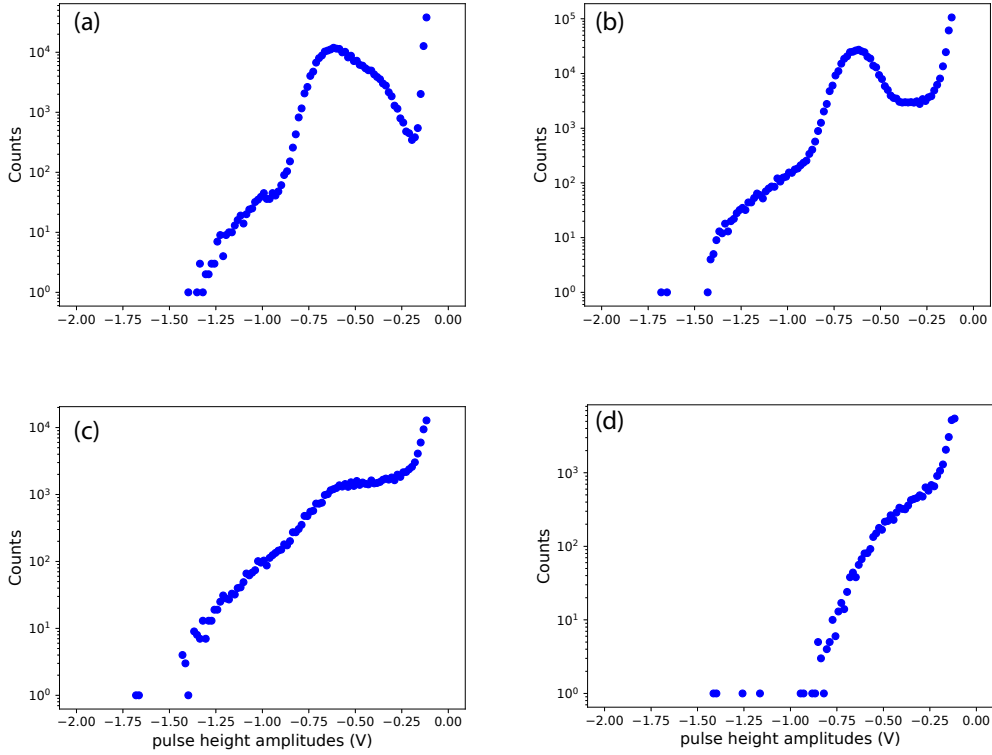
Figure 7.2: Pulse height distributions at the NICE detector for the delayed events(a), OBIS events (b), background events (c) and dark counts (d).

1 Delayed detachment which will be called *delayed events* with the formula for the time windows: $[(t_{tof} + i \cdot t_{rev} - 0.3)\mu s, (t_{tof} + i \cdot t_{rev} + 0.3)\mu s]$ (t_{tof} is the flight time of the ions, t_{rev} the revolution time and i the number of delayed peaks that are visible). The time window width is $\Delta t = 0.6\,\mu$s

2 Detachment by the cw OBIS laser (*OBIS events*). Two time windows are set: $[-4.4\,\text{ms}, -1.9\,\text{ms}]$ and $[2.1\,\text{ms}, 4.4\,\text{ms}]$

3 Detachment by collisions with residual background (*background events*) with two time windows: $[-1.9\,\text{ms}, -0.2\,\text{ms}]$ and $[4.6\,\text{ms}, 4.9\,\text{ms}]$

Also recorded and analyzed are the detector dark counts, which are measured at the end of each injection, when the ion beam is kicked out. This is achieved by switching of an electrostatic deflection element, which deflects the ions off their orbit.

7.2 Pulse Amplitude Cuts

For the three types of possible neutralization events on the detector, a pulse height discrimination helps in reducing the signal to background ratio. Therefore, the pulse height distributions need to be studied. They are shown in Fig. 7.2.

The electrodes of the NICE detector are set such that the recorded pulse height is sensitive to the type of impact. Molecules are able to produce multiple electrons on impact with the MCP surface, while photons in the visible light regime are only able to release one electron. The accuracy of the detected amplitude is limited by the discretization of the voltage levels with 128 bits devided over a 2 V range (accuracy $= \frac{2\,\text{V}}{128} = 0.0156\,\text{V}$). A first discriminator value is hardware-set on the pulse heights at $-0.28\,\text{V}$. Only pulses that have higher negative amplitudes are recorded. Delayed events are gated with a narrow time window of $0.6\,\mu\text{s}$, which results in a reduced signal to noise ratio. It is desirable to improve the delayed events to background events ratio and the OBIS events to background events ratio.

When carefully checking the background signal from Fig. 7.1 right after the laser shot, it appears that the collisional background is not constant, but shows some wavy structure as shown in a zoomed in picture (see Fig. 7.3). The curvy structure in the spectrum is removed by applying a lower amplitude cut of $-0.5\,\text{V}$ (see panel 7.3 (a) to (b)). In panel (c) and (d) the ratio of OBIS laser to background and the ratio of delayed events to background is shown for a set of amplitude cuts, which were taken in one run. This method has been applied to multiple runs and the ratios all look very similar. For the later analysis the amplitude cut of $[-0.5\,\text{V}, -1.3\,\text{V}]$ (olive green data point) has been chosen. Here, the signal to noise ratios look very promising, without losing too much of the data taken.

7.3 Non-Random noise between two pulses

Fig. 7.4 shows the digital timing trace of integrated counts for one run for events within the OBIS laser (black curve) and background (blue curve) timewindow. The initial steep decay from high counts close to $0\,\mu\text{s}$ is attributed to the event itself. The two peaks arising within the first $2\,\mu\text{s}$ are linked to a reflection signal obtained on the NICE detector. The front voltage of the detector is set to $-600\,\text{V}$, so that neutral Al_4 and neutral Al fragments that hit the detector may lose an electron upon impact or impact ionize atoms on the detector surface, which are then again detected by the detector. This process is depending on the distance of the initial impact spot, which leads to the peak-like structure as seen in the signal for the OBIS and background events. Note that the curve for OBIS events has been scaled by a factor of 2 and amplitude cuts of $[-0.5\,\text{V}, -1.3\,\text{V}]$ have been applied here, which already lead to a suppressed number of
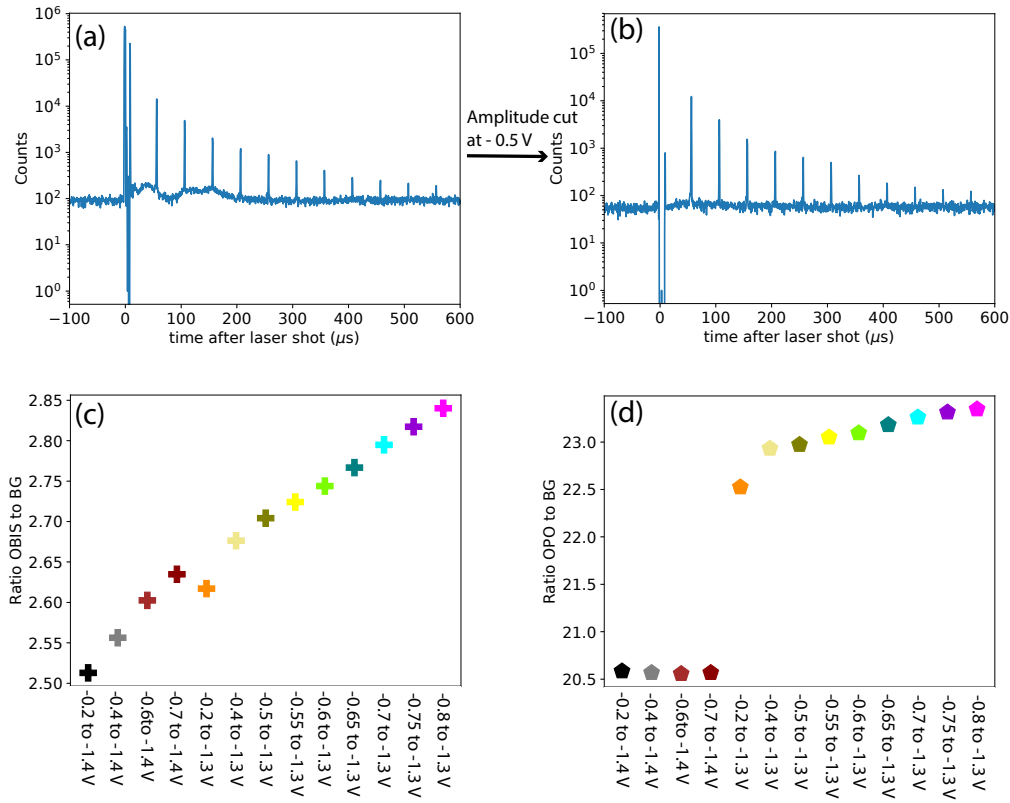
Figure 7.3: Check of various amplitude cuts for one run. The top panels (a) and (b) show how the wavy structure in the time of flight spectrum is removed by applying a lower limit for the amplitude height. (c) shows the OBIS to background events and panel (d) shows the ratio of delayed events to background events for a set of different amplitude cuts. The values for the amplitude cuts are shown on the x-axis.

reflection events within the OBIS window. We get rid of these non-random noise events by applying a time cut at $2.5\,\mu$s.

7.4 Normalization by photon number

The pulsed laser was tuned over a wide range from $1.7\,$eV up to $2.3\,$eV. The power measurement of PM 2 (located behind the end of the overlap section) was used to normalize the events, which were obtained on the detector, with the amount of photons that the ions were exposed to.

Changing photon energies leads to small changes in the beam pointing of the laser. After leaving the laser box, the light is guided over a distance of $\approx 12\,$m before hitting
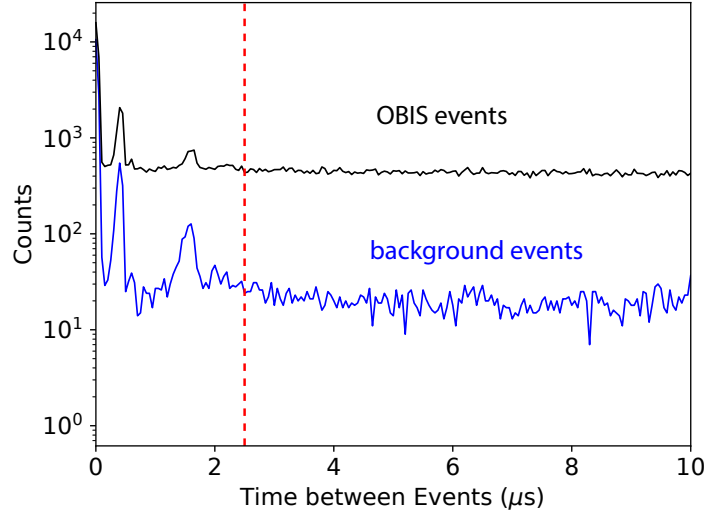
Figure 7.4: OBIS events (black) and background events (blue) versus time after last event. After 2.5 μs (red dashed line) there is no reflection peak in both signals.

PM 2. Therefore, already small changes in the beam pointing can be seen on PM 2. Another powermeter was placed right after the exit of the OPO laser, which was used to check the power output stability. A small fraction of the laser light is reflected by a glass plate onto this power meter. Both signals on the power meters are shown in Fig. 7.5. The number of photons N is calculated:

$$N = \frac{I}{hc\nu} \tag{7.85}$$

with I being the averaged measured pulse energy and ν being the set wave number. For every laser shot the pulse energy is measured. It is averaged for the desired time window. The standard deviation σ_N of the single measurement is:

$$\sigma_N = \sqrt{\frac{1}{n-1}(\sum_i (N_i - \bar{N}))^2}. \tag{7.86}$$

The standard deviation of the mean value $\sigma_{\bar{N}}$ then is

$$\sigma_{\bar{N}} = \frac{\sigma_N}{\sqrt{n}} \tag{7.87}$$

Both power measurements show an incline in the photon number N for higher photon energies. For the power measurement after the OPO laser exit, the measured curve is more smooth in comparison to the measured PM 2 curve. This means that the peak structure measured for the PM 2 curve is related to beam pointing of the laser and not to power fluctuations.

Two irises have been implemented between two mirrors, where there is no additional optical elements in between (for the exact position see Fig. 6.1). The idea is to reduce
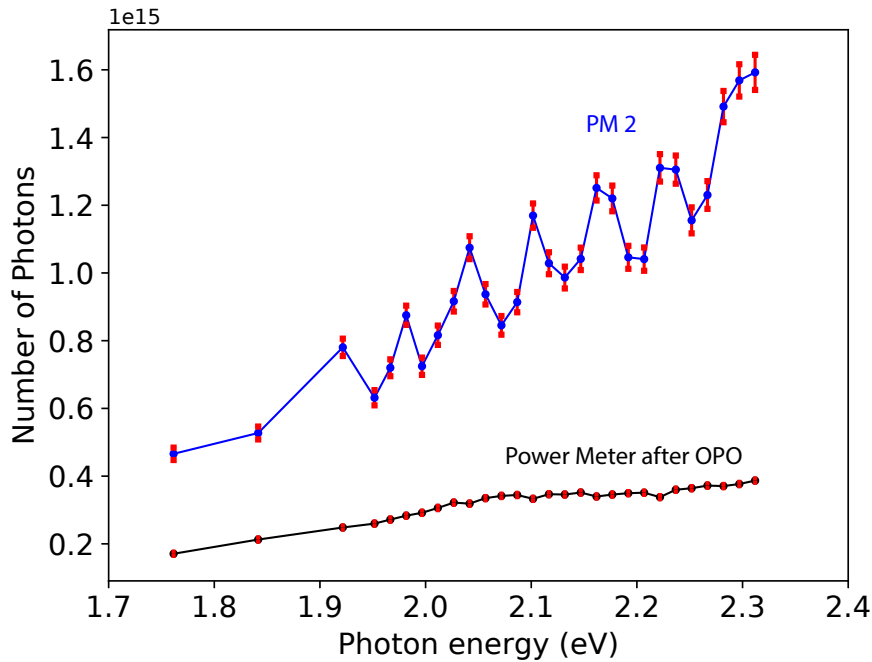
Figure 7.5: Number of photons versus photon energy. The blue curve shows the number of photons for PM 2 and the black curve shows a fraction of the laser light right after the OPO laser exit in terms of number of photons.

beam pointing and therefor power fluctuations measured on PM 2 in the relevant photon energy range. Closing the irises down to 1 mm reduces the power fluctuation caused by the beam pointing instabilities on the long laser path. The measurements were conducted using 1 mm aperture settings.

7.5 Normalization by OBIS laser signal

The first normalization step, which is taking into account the number of photons for the observed signals, has been described above. In the following, the normalization to the number of stored ions is made. Since the energy of the OBIS laser of 3.07 eV is much higher than the probe energies, it is assumed that this laser is high enough in energy, to photodetach all of the stored ions with the same cross section. For normalization, the background events are subtracted from the OBIS events (both normalized to their respective time window). This means that the dark count events are automatically subtracted. The difference (see Fig. 7.6) is proportional to the number of stored ions. The errors for the OBIS N_{OBIS} and background N_{BG} events are calculated using Poisson statistics and the error for the difference ΔN_{ion} is calculated with
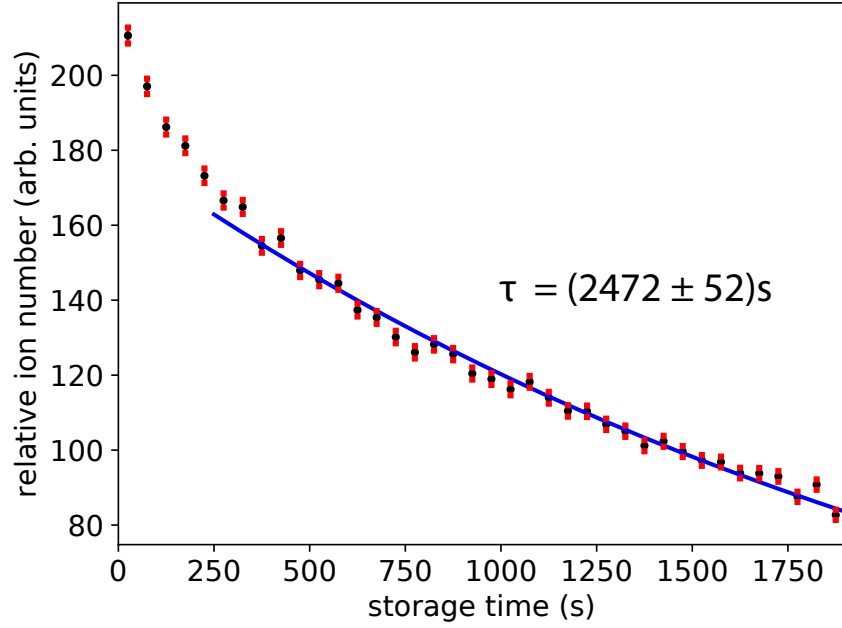
Figure 7.6: Relative number of ions versus storage time (for 1.97 eV photon energy set at OPO laser). A single exponential fit (blue curve) has been applied to the data for storage times above 250 s.

$$\Delta N_{\mathrm{ion}} = \sqrt{(\Delta N_{\mathrm{BG}})^2 + (\Delta N_{\mathrm{OBIS}})^2}. \tag{7.88}$$

In order to compare different runs with different settings, the ion number N_{ion} is scaled with the power, measured by the photo diode PD for the OBIS laser.

The signal shown in Fig. 7.6 shows the relative stored ion number versus the storage time. From the decay, the lifetime of the stored ions inside the storage ring can be inferred. A single exponential fit has been applied to the data set for storage times above 250 s and from the decay constant the beam lifetime of the stored Al_4^- ions can be estimated to $\tau = (2472 \pm 52)$s. As it was shown in Sec. 4.3 in the first part of this thesis, the beam decay is described by a set of exponential functions. Therefore, the deviations from a single exponential fit for this data set, especially at short storage times, are expected. Nevertheless, the 2500 s show an approximation for the beam lifetime.

A summary of the applied methods for analyzing the data is given below:

1. The time of flight spectrum is essential to assign the various type of events that occure during the measurement. Three types of interaction have been categorized in Sec. 7.1 and the respective time windows have been set.

2. The amplitude cut helps in increasing signal to noise for OBIS and delayed events. By choosing an amplitude cut of $[-0.5\,\mathrm{V}, -1.3\,\mathrm{V}]$ the signal to noise ratio has been

greatly improved and time correlated background (see Fig. 7.3) below the delayed peaks has been suppressed.

3. Removing non-random noise by applying a time cut (see Fig. 7.4) at $2.5\,\mu$s avoids adding systematic shifts to the data.

4. Measuring the photon number for the various photon energies is essential for normalizing the obtained delayed signals to the exposed laser light.

5. The OBIS laser signal N_{ion} gives the normalization for the delayed signal to the number of stored ions.

7.6 Constructing the delayed detachment signal

The rate R of the observed delayed events in the linear regime, is given by

$$R(t, \epsilon_{ph}) \propto \sigma_{pd}(\epsilon_{ph}) \cdot \rho(t) \cdot l \cdot \Phi, \tag{7.89}$$

where $\sigma_{rel}(\epsilon_{ph})$ is the relative cross section for the respective photon energy, $\rho(t)$ is the ion density for the stored ion beam, l is the overlap length and ϕ is the photon flux. The exact overlap for the ion and laser beam is not known, which does not allow measurements of the total cross section. The ion density $\rho(t)$ is proportional to the difference between OBIS events and background events $\rho \sim N_{\text{ion}}$, as explained in Sec. 7.5. The photon flux Φ is calculated as described in Sec. 7.4. Obtaining values for the relative cross section σ_{rel} in a given time window is done by calculating Φ, the relative ion number and the number of delayed events N_l (after applying steps 1.- 3. see Sec. 7.5) in the specific time window:

$$\sigma_{rel} = \frac{N_l}{N_{\text{ion}}\Phi} \tag{7.90}$$

The errors are calculated by error propagation:

$$\Delta\sigma_{rel} = \sqrt{\left(\frac{\Delta N_l}{N_{\text{ion}}\Phi}\right)^2 + \left(\frac{N_l\Delta N_{\text{ion}}}{N_{\text{ion}}^2\Phi}\right)^2 + \left(\frac{N_l\Delta\Phi}{N_{\text{ion}}\Phi^2}\right)^2} \tag{7.91}$$

Fig. 7.7 shows the normalized yield on the NICE detector as a function of photon energy for multiple runs. The beam was stored for $12\,$s with $1\,$s beam-off time. A set of storage time t_s cuts has been applied. Towards later times the curves become narrower and are shifted to higher photon energies. The longer the aluminum clusters are stored, the more they cool. As a result, a higher photon energy is needed to detach colder molecules. The blue and red curves have been normalized to the area under the black curve.
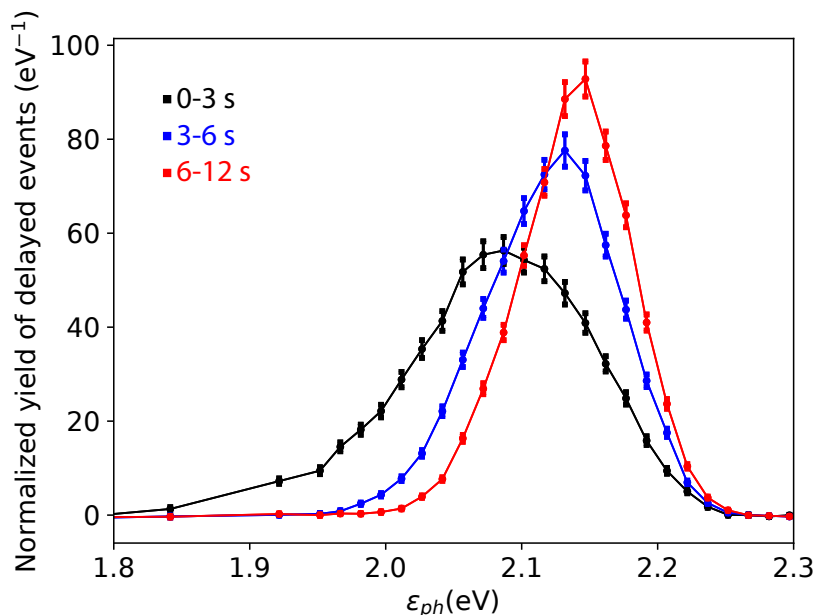
Figure 7.7: Normalized yield of delayed events on NICE versus photon energies ϵ_{ph} for different storage time cuts. For later times the spectrum gets narrower and is shifted to higher photon energies.

7.7 Photo absorption for different storage times

The low temperatures and excellent vacuum conditions inside the CSR allowed us to follow the cooling of the Al_4^- clusters for up to 2100 s. The results are shown in Fig. 7.8. In principle, even longer measurements would have been possible since the observed beam lifetime for this specific molecule was around 2500 s (and even up to 3500 s in some cases). However, measuring a full curve like for the 2100 s data already took 28 hours of measurement time. It is also challenging to keep the ion source and the cryostat in a stable condition throughout the measurement. In a nutshell, there simply was not enough time during the beam time to go for even longer storage times.

The photo absorption curves, which are shown for multiple runs with different storage times, are shown in Fig. 7.8. The gray curves show data taken at a room temperature ion trap (Aviv et al. 2011) and the colored curves show data taken at the CSR. For every curve there have been multiple runs, where the data have been combined and analyzed as described in the previous sections. In order to avoid depletion for laser exposure of more than 15 s, the shutter for both lasers has been closed all the time for the longer storage times and was only opened at the end of every injection cycle. Photon energies were only changed in between injections. The curves have been normalized by their respective area. For this purpose, Gaussian fits have been applied, which represent the measured points really well, except for the curve with the longest storage time. A zoom
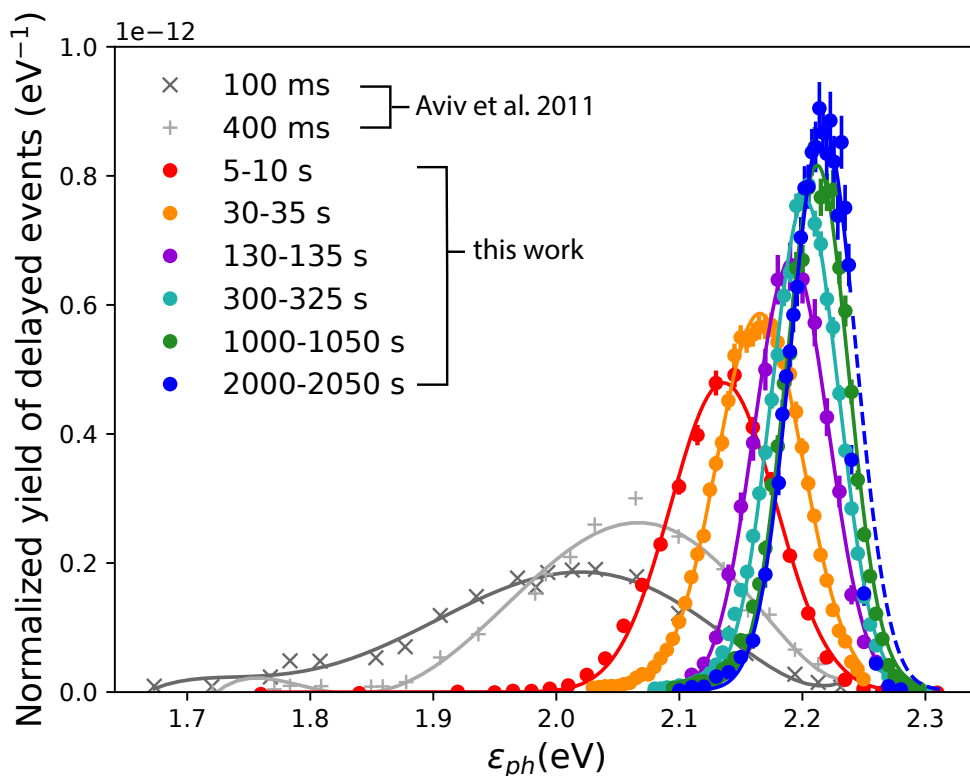
Figure 7.8: Normalized yield of delayed events on NICE versus photon energies ϵ_{ph} for different storage time cuts up to 2050 s. Both gray curves show previous data from Aviv et al. 2011 and the colored curves show data taken at CSR.

in to photon energies ϵ_{ph} $(2.07\,\text{eV} - 2.28\,\text{eV})$ is shown in Fig. 7.9. The final measured cooling curve is not represented by a Gaussian fit anymore. The width of the curve is less than 57 meV. This would mean that per degree of freedom $(3N - 6 = 6$ for $N = 4)$, an energy of less than 10 meV would be remaining. This energy would correspond to a temperature of $T \cong 115\,\text{K}$, which is already well below room temperature (subthermal).

7.7.1 Determination of the energy shift E_S

So far, we have taken into account all of the accessible delayed peaks in our time of flight spectrum. The position and width of the individual delayed peaks can be used to learn more about the internal excitation of the molecule. Observing later delay peaks corresponds to probing the low energy part of the cluster's energy distribution. Thus, later delayed peaks probe a colder part of the Al_4^- distribution. A first approach to get the value for the energy shift E_S (illustration of this value in Fig. 5.7 in section 5.6) is by applying the fit for the kinetic factor (see Sec. 5.6) to the individual delayed peak distributions as shown in Fig. 7.10 (a). The energy E_S corresponds to those ions that are decaying on a time scale, which is not observable by our experiment. These are delayed events occuring so late that they are not distinguishable from the background
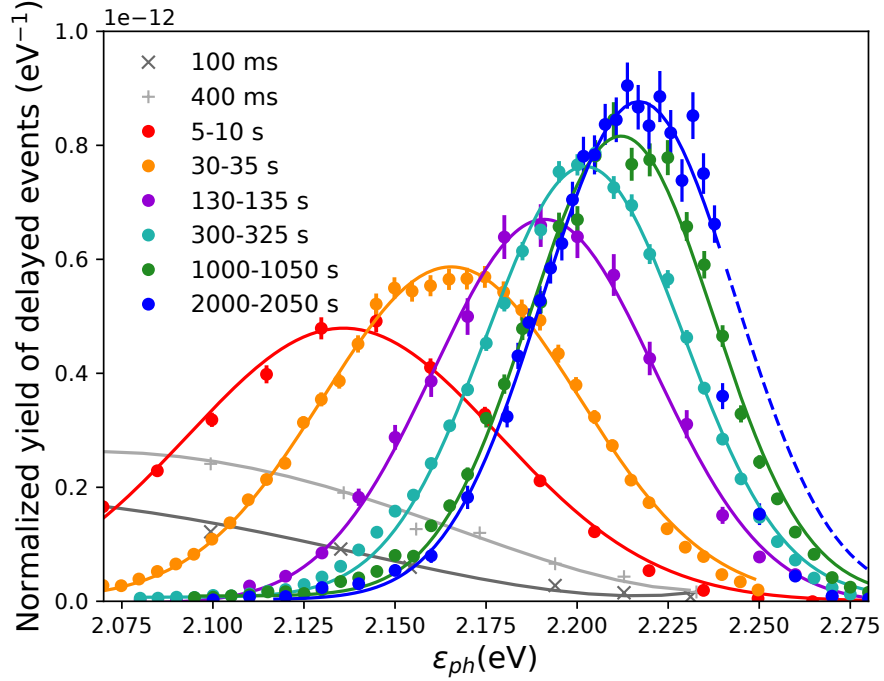
Figure 7.9: Normalized yield on NICE versus photon energies for different storage time cuts up to 2200 s for photon energies between $2.07\,\mathrm{eV} - 2.28\,\mathrm{eV}$. For the blue curve, the Gaussian fit is clearly off on the right side.

anymore. The kinetic factor is a convolution of the Maxwell-Boltzmann distribution with the probability of ions to emit an electron in the respective time window of the delayed peak after photo absorption.

In order to understand this parameter, it is required to look at the delayed peaks individually and check for their positions. Note that the curve for the delayed peaks 4-10 was normalized, such that its area is the same as the area for delayed peaks 1-3. The distributions are shifted into the expected direction, later time windows probe lower internal energies. From applying the fit for the kinetic factor to the curves, the parameter E_S is determined to $E_S = (0.02 \pm 0.01)\mathrm{eV}$ from the peak positions and the energy windows $E_{w,1-3} = 0.064\,\mathrm{eV}$ and $E_{w,4-10} = 0.049\,\mathrm{eV}$ can be estimated. The following parameters have been used for the fit: $T = 156\,\mathrm{K}$, $k_r = 1000\,\mathrm{s}^{-1}$, $E_a = 2.23\,\mathrm{eV}$ and $\alpha_p = 45\,\text{Å}^3$. Note that both curves do not represent the data very well. Within the model the width of both curves cannot be adjusted in such a way that they fit for both data sets. One obvious explanation is that there is something missing in the model. The Maxwell-Boltzmann distribution does not represent the energy distribution of the clusters while cooling down in the CSR. It will be affected by the energy-dependent density of states of the clusters. In conclusion, the clusters may not be thermalized at all times during this long cooling phase and the assumptions for a Maxwell-Boltzmann distributions do not hold anymore.
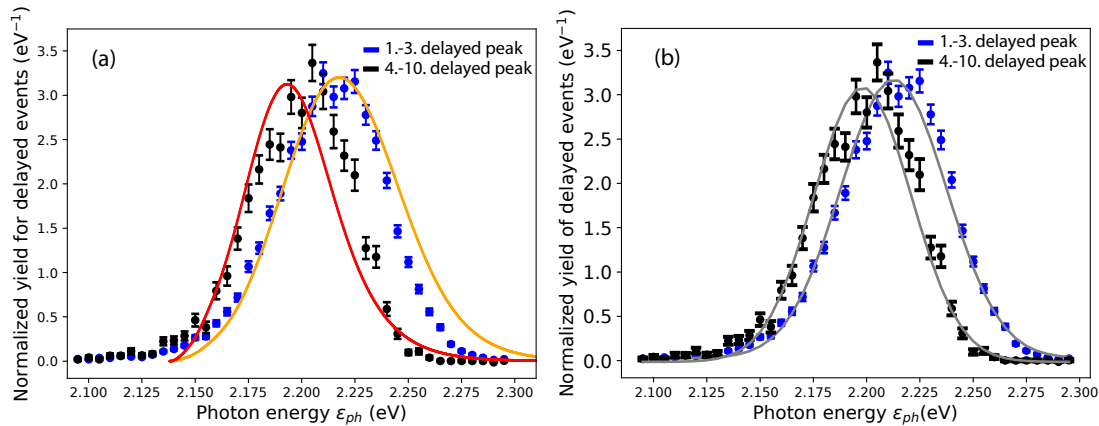
Figure 7.10: Normalized yield versus photon energies ϵ_{ph} for the delayed peaks 1.-3. and for the delayed peaks 4.-10. with the 1050 s data set. Fits for the kinetic factor are applied to both curves in panel (a). Gaussian fits are applied to the curves in panel (b).

Obtaining an estimate on this parameter (E_S) is an important step in order to calculate the internal energy of the ions, which will also be required later on. The internal energy ϵ is given by

$$\epsilon = E_a - E_S - \epsilon_{ph}. \tag{7.92}$$

In order to obtain a more reliable value for the energy shift E_S, a different approach is chosen, where the datapoints are approximated by Gaussian fits as shown in Fig. 7.10 (b) and the positions of both delayed peak distributions are given by the centroid of the respective fit and the errors are also taken from the fit. The positions of both distributions are determined to be $\bar{E}_{1-3} = (2.2127 \pm 0.0004)$eV and $\bar{E}_{4-10} = (2.1981 \pm 0.0009)$eV. With those two values the energy shift is calculated to $E_S = (0.0146 \pm 0.0009)$eV.

7.8 Time dependence of the delayed emission yield

A new aspect of the measurement on the Al$_4^-$ system is presented in this section. The yield of delayed events for a fixed photon energy versus storage time will be discussed. With the help of Fig. 5.7, the goal of this section can be understood better. Choosing a fixed photon energy and observing the delayed electron emission versus storage time is analogue to scanning the energy-axis, since internal excitation distributions of Al$_4^-$ molecules that have been stored for longer times, will shift towards lower energies.

The observed delayed electron emission signal has been normalized to the OBIS laser signal for the respective time window. The decay curves have been analyzed for all

photon energies and a few selected curves are shown in the Fig. 7.11. For the curves up to 2.09 eV the lasers were on for the entire storage time. For longer times it is necessary to avoid laser depletion on the stored ions. Thus, the lasers were only switched on at certain times by opening and closing the laser shutter. For the blue curves the lasers were turned on from $30 - 35$s, $40 - 45$s, $50 - 55$s and $60 - 65$s. For the pink 2.15 eV and 2.18 eV curves (see the inset of Fig. 7.11) the ions were exposed to the lasers every 50 s for 5 s. Note that the values for the delayed yields have been scaled such that all the curves fit into one figure. The fits that have been applied to the data points were done by a feed and decay model, which consists of two decay constants k_{feed} and k_{LT}

$$Y(t) = \frac{k_{LT}}{k_{feed} - k_{LT}} N \left(e^{-k_{LT}t} - e^{-k_{\text{feed}}t} \right), \tag{7.93}$$

where $Y(t)$ is the integrated yield of neutrals from delayed electron emission on the detector normalized to the OBIS laser window, N is the number of ions and t is the storage time.

A clear trend in this figure is observable as for later times the decay constant becomes smaller meaning that $\tau_{\text{decay}} = k_{LT}^{-1}$ becomes longer. Interestingly, the green curve at $\epsilon_{ph} = 2.09$ eV for $t_s < 3$ s and the pink curve at $\epsilon_{ph} = 2.12$ eV for $t_s < 50$ s show an increase in delayed yield at early storage time. This is a direct hint towards radiative cooling happening, as the population of the ions gets colder, more of them are able to be detached by a certain wavelength.

These kind of fits have been applied to various photon energies for runs with different storage time settings and from the fits the decay constant is used to determine the yield of delayed events as a function of photon energy. The resulting curve will be shown and discussed in the following section (see Sec. 7.9).

7.9 Cooling rate of Al$_4^-$

Fig. 7.12 shows the decay constant k_{LT} in dependence of the photon energy. Every single data point results from a fit in the form of equation (7.93). The error bars are given by the respective fit. Multiple runs for storage times of up to 500 s are represented by these points. The colorcode is the same as for the delayed emission yield in Fig. 7.11. The blue line shows a fit to the data, which is resembling a power law trend and clearly not a single exponential decay. A first approach to understand the measured data is by comparison to the *rapid exchange model* that has been used for previous studies at shorter storage times with less elaborate data. Although the absolute scale of its rate cannot be calculated (might still move up or down on the absolute scale), it is obviously not fitting the experimental data very well.
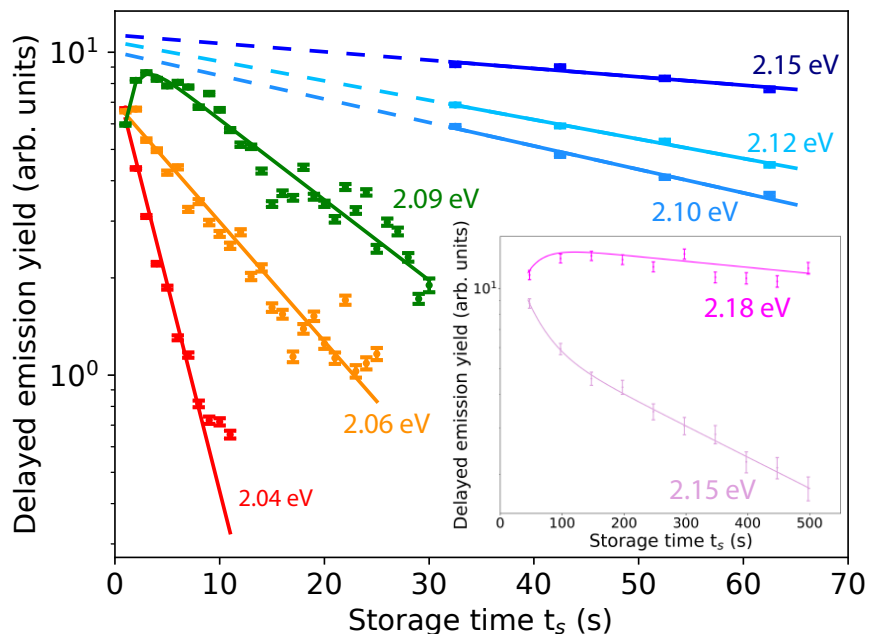
Figure 7.11: Delayed emission yield for various photon energies shown versus storage time. The curves represent fits that have been made by the feed and decay model (see equation (7.93)).

For excitation energies below the first electronically excited state (vertical dashed line), the data is fitted with the *slow exchange model* indicated by the blue line (as described in sub section 5.4.3.1) and extrapolated (dashed blue line) towards higher excitation energies. For photon energies above $\epsilon_{ph} > 2.07 \, \text{eV}$ (or below $\epsilon < 0.15 \, \text{eV}$) the experimental data is well represented. But for higher excitation energies also the first electronic excited state might be populated and contribute to the decay constant. Thus, for excitation energies above $0.15 \, \text{eV}$ the data is fitted with the sum of the *slow exchange model* that is extrapolated towards higher excitation energies and the addition of the recurrent fluorescence (RF) rate from the first electronic excited state:

$$k_{LT} = \begin{cases} B \cdot (\rho_0(\epsilon) - \rho_1(\epsilon)) \ \text{ for } \ \epsilon < 0.15 \, \text{eV}, & \text{(7.94a)} \\ A_1(E_1) \cdot \dfrac{\rho_0(\epsilon - E_1)}{\rho_0(\epsilon)} + B \cdot (\rho_0(\epsilon) - \rho_1(\epsilon)) \ \text{ for } \ \epsilon > 0.16 \, \text{eV}. & \text{(7.94b)} \end{cases}$$

ρ_0 is the density of states for Al_4^- and ρ_1 is the density of states without the short-lived component B_{2u}. The Einstein coefficient of the first electronically excited state $A_1(E_1)$ is unknown and is treated as a fit constant in this figure. In order to approximate the measured rates by equation (7.94a), $\rho_0(\epsilon)$ and $\rho_1(\epsilon)$ had to be converted (with $\epsilon = E_a - E_S - \epsilon_{ph}$) to $\rho_0(E_a - E_S - \epsilon_{ph})$ and $\rho_1(E_a - E_S - \epsilon_{ph})$, respectively . The energy value $E_v = E_a - E_S$ is then treated as another fit constant together with fit constant B. From the fit the values $B = 1.3 \times 10^{-5} \text{s}^{-1}$ and $E_v = (2.22 \pm 0.02) \text{eV}$ are estimated. With this value, the zero point energy for the ϵ scale
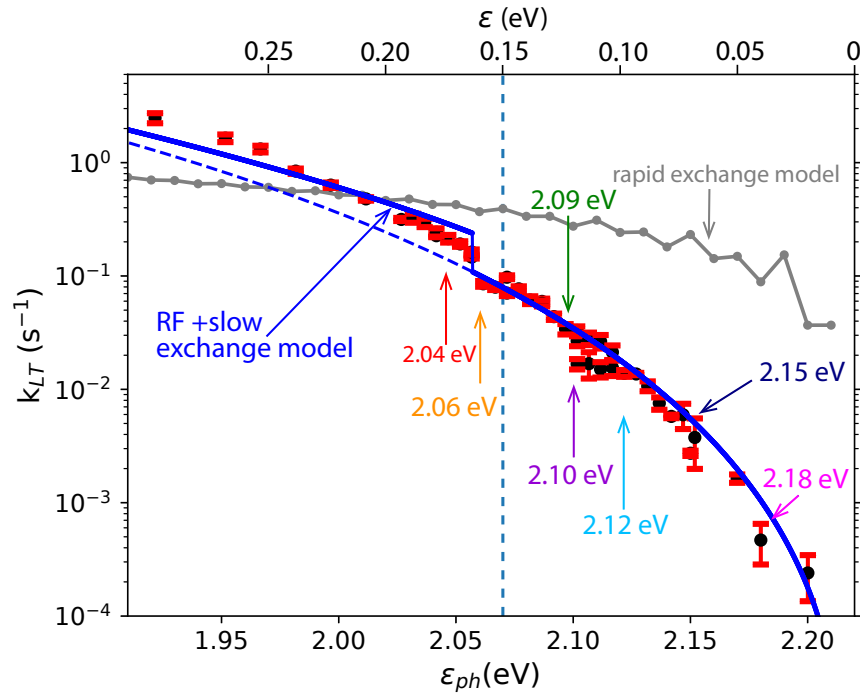
Figure 7.12: Decay constant k_{LT} versus photon energy ϵ_{ph} and internal energy ϵ. Each data point is a result from the fit as described in the previous section. The solid blue line is a fit as described in equation (7.94) and in main text. The dashed blue line is the extrapolated fit for equation (7.94a). The lower x-axis is the photon energy and the zero point of the upper scale is derived from the fit paramters as described in the main text.

$$\epsilon = E_v - \epsilon_{ph} \tag{7.95}$$

can be added to our figure (see upper x-axis scale in Fig. 7.12). Furthermore, from the value for the energy shift $E_S = (0.0146 \pm 0.0009)$eV (see previous section 7.7.1), the value for the adiabatic electron affinity (AEA) is calculated

$$E_a = E_v - E_S = (2.21 \pm 0.02)\text{eV}. \tag{7.96}$$

Two models for the description of the expected decay rate have been introduced in subsection 5.4.3.1:

1. The *rapid exchange model* is represented by the gray line in Fig. 7.12. Within this model it is assumed that IVR occurs much faster (quasi instantaneous) than the infrared emission. This model does not represent the measured data very well. For high internal excitations the rate is too low, while for low internal excitations, the expected rate is too high.

2. The *slow exchange model* in combination with RF is shown by the blue line in Fig. 7.12. Here the opposite case is described, with IVR rates being much slower than the infrared emission rates. Below the threshold for recurrent fluorescence (set to $\epsilon = 0.15\,\text{eV}$), the data is fitted by the slow exchange model. For energies above this value, the rate for recurrent fluorescence is added on top of the rate from the slow exchange model. This case matches our experimental data very nicely, especially for small internal excitations. One possible explanation for the curve to be more skewed at higher internal excitations is that there might be more electronic excited states being available for the RF process, which would result in a steeper curve.

7.10 Summary and conclusive remarks

In this second part of the thesis we have observed cooling of the isolated Al$_4^-$ cluster at the cryogenic storage ring. The beam lifetimes during this beamtime have improved significantly and beam lifetimes of up to 3400 s have been measured in some cases, which also enabled very long measurements on the cooling behavior of Al$_4^-$.

Delayed electron emission spectra were measured and the cooling process for this model system has been studied within the low black body radiation field of the CSR. We have observed vibrational radiative cooling of Al$_4^-$ for up to 2100 s by utilizing the delayed electron emission spectra using a pulsed tunable laser (used in the range from 1.85 eV up to 2.3 eV) for sampling in combination with a cw laser (OBIS laser at 3.07 eV), which has been used to normalize the spectra to the number of ions. Cooling is observable on this very long time scale - in comparison to previous room temperature experiments (Aviv et al. 2011) as shown in Fig. 7.12 - although the lifetimes of the vibrational levels are much shorter (longest vibrational lifetime of 39.17 s of the B$_{1u}$ state see table 5.2). This already shows that there has to be a process responsible for enabling these long cooling time scales. We attribute this to the IVR process, which is redistributing the energies of the vibrational degrees of freedom over all possible modes including the IR inactive modes. Inerestingly, the CSR allows us to reach time scales, where IVR becomes the bottle neck for cooling and we are able to observe it on a much longer time scale than shown in previous experiments, where it was found to be on the picosecond time scale (Makarov, Malinovsky, and Ryabov 2012) or for carbon cluster ions, where it is assumed to be fast on the order of nanoseconds up to miliseconds (Stockett et al. 2020 and Bull et al. 2019). This already is a very interesting finding and could be followed even further, by investing time in observing delayed electron emission spectra for even longer storage times (so far one data point for the 2100 s data, took 35 minutes) or even check for IVR of Al$_5^-$ ions, which are suspected (Lange et al. 2012) to have even longer radiative cooling times.

By observing the cooling for specific photon energies versus storage times (see Fig. 7.11), we can extract the cooling rate constants and we can compare those with the predictions of our theoretical models (see Fig. 7.12). Via fitting the measured data with the *slow exchange model* we can extract the value for the adiabatic electron affinity to be $E_a = (2.21 \pm 0.02)$ eV. The value for the AEA is in agreement with previous measurements and close to theory (see Kafle et al. 2015, Zhao and Zhang 2007 and Li et al. 1998). Combining the *slow exchange model* with the rate for recurrent fluorescence for excitation energies above the first electronic excited level $\epsilon > 0.15$ eV reproduces our measured data. The slightly flatter curve by our model (at higher excitation energies) is caused by only taking the lowest electronically excited state into account, when in fact at higher internal excitation energies of Al_4^- more levels could contribute to the RF rate. In summary, with our quantum chemical calculations, we can analyze the data and show the influence of IVR for isolated clusters for the first time.

Chapter 8

Outlook

In the course of this work, the analysis of photodetachment on two systems of negative ions has been presented. Silicon anions and Al_4^- molecules have been studied at the Cryogenic Storage Ring, which enables measurements at low ambient temperatures and with very long storage times.

In the first part of the thesis, the lifetime of the very fragile ^2P states $\tau = (22.5\pm2.5)s$ of Si^- has been measured and a lower limit of the lifetime $\tau_r > 5.7\,h$ (within a confidence level of 90%) for the very long-lived ^2D states has been given, which is the longest atomic metastable state in anions ever observed. Further improvements on the lifetime studies of the metastable ^2D states of Si^- could be possible, aiming to resolve the difference in the $^2D_{5/2}$ and $^2D_{3/2}$ lifetimes of about $10\,h$ and $12\,h$, respectively (in the recent MCDHF calculation). Simply re-measuring would already lead to improved beam lifetimes since the presented measurements were conducted in the first cold beamtime of the CSR and a lot of improvements and knowledge considering the storage ring settings have been obtained since then. Also, the electron cooler could be added to the measurement scheme, where after injecting the ions, a certain time period would be dedicated towards phase-space cooling of the stored silicon anions, which leads to an increased beam lifetime.

The cooling behavior of isolated clusters, in the case of Al_4^-, has been shown in the second part of the thesis. Understanding the energy flow, and especially the IVR process, within the molecule's degree of freedom is essential for understanding chemical reactions (Gruebele and Wolynes 2004 and Makarov, Malinovsky, and Ryabov 2012). Vibrational cooling was observed for up to $2100\,s$ and time scales have been reached where we can shine a light on the IVR process of isolated molecules. Our calculations, assuming IVR to be the governing process represent the experimental data very well.

Additional measurements could be conducted in combination with the cryogenic reaction microscope (REMI), which is currently in the process of being included in the forth straight section of the CSR. It would offer the possibility to measure the kinetic

energy of the detached electron.

So far, we have only been looking at the delayed electron emission. With further measurement time dedicated to the Al_4^- molecule, we could also still try to understand the delayed or direct fragmentation process, which was found to be a competing process in Aviv et al. 2011. By studying the fragmentation process, the influence of rotational cooling could be investigated.

Bibliography

Alton, G.D. (1989). 'The sputter generation of negative ion beams.' In: *Nuclear Instruments and Methods in Physics Research Section B: Beam Interactions with Materials and Atoms* 37–38, pp. 45–55. DOI: https://doi.org/10.1016/0168-583X(89)90134-1.

Amitay, Z. et al. (1999). 'Dissociative recombination of vibrationally excited HD$^+$: State-selective experimental investigation.' In: *Phys. Rev. A* 60 (5), pp. 3769–3785. DOI: 10.1103/PhysRevA.60.3769.

Andersen, J. U., H Cederquist, JS Forster, BA Huber, P Hvelplund, J Jensen, B Liu, B Manil, L Maunoury, S Brøndsted Nielsen, et al. (2003). 'Power-law decay of collisionally excited amino acids and quenching by radiative cooling.' In: *The European Physical Journal D-Atomic, Molecular, Optical and Plasma Physics* 25.2, pp. 139–148.

Andersen, JU, E Bonderup, and K. Hansen (2002). 'Thermionic emission from clusters.' In: *Journal of Physics B: Atomic, Molecular and Optical Physics* 35.5, R1.

Andersen, JU, C Gottrup, K Hansen, P Hvelplund, and MO Larsson (2001). 'Radiative cooling of fullerene anions in a storage ring.' In: *The European Physical Journal D-Atomic, Molecular, Optical and Plasma Physics* 17.2, pp. 189–204.

Andersen, LH, Oded Heber, and Daniel Zajfman (2004). 'Physics with electrostatic rings and traps.' In: *Journal of Physics B: Atomic, Molecular and Optical Physics* 37.11, R57.

Andersen, T (2004). 'Atomic negative ions: structure, dynamics and collisions.' In: *Physics Reports* 394.4, pp. 157–313. DOI: https://doi.org/10.1016/j.physrep.2004.01.001.

Andersen, T, H. K. Haugen, and H. Hotop (1999). 'Binding Energies in Atomic Negative Ions: III.' In: *Journal of Physical and Chemical Reference Data* 28.6, pp. 1511–1533. DOI: 10.1063/1.556047.

Andersson, Pontus et al. (2006). 'Radiative lifetimes of metastable states of negative ions.' In: *Phys. Rev. A* 73 (3), p. 032705. DOI: 10.1103/PhysRevA.73.032705.

Aviv, Ofer, Y Toker, Daniel Strasser, ML Rappaport, Oded Heber, Dirk Schwalm, and Daniel Zajfman (2011). 'Competition between delayed ionization and fragmentation of laser-excited Al 4-.' In: *Physical Review A* 83.2, p. 023201.

Becker, Arno (2016). 'Imaging of Neutral Fragmentation Products from Fast Molecular Ion Beams: Paving the Way for Reaction Studies in Cryogenic Environment.' PhD thesis. University of Heidelberg. DOI: https://doi.org/10.11588/heidok.00020213.

Bernath, Peter F (2020). *Spectra of atoms and molecules.* Oxford university press.

Bixon, Mordechai and Joshua Jortner (1968). 'Intramolecular radiationless transitions.' In: *The Journal of chemical physics* 48.2, pp. 715–726.

Blondel, C., W. Chaibi, C. Delsart, C. Drag, F. Goldfarb, and S. Kröger (2005). 'The electron affinities of O, Si, and S revisited with the photodetachment microscope.' In: *The European Physical Journal D - Atomic, Molecular, Optical and Plasma Physics* 33. DOI: 10.1140/epjd/e2005-00069-9.

Breitenfeldt, Christian, Klaus Blaum, Sebastian George, Juergen Goeck, Gregorio Guzman-Ramirez, Jonas Karthein, Thomas Kolling, Michael Lange, Sebastian Menk, Christian Meyer, et al. (2018). 'Long-term monitoring of the internal energy distribution of isolated cluster systems.' In: *Physical Review Letters* 120.25, p. 253001.

Buckman, Stephen J. and Charles W. Clark (1994). 'Atomic negative-ion resonances.' In: *Rev. Mod. Phys.* 66 (2), pp. 539–655. DOI: 10.1103/RevModPhys.66.539.

Bull, James N, Michael S Scholz, Eduardo Carrascosa, Moa K Kristiansson, Gustav Eklund, Najeeb Punnakayathil, Nathalie de Ruette, Henning Zettergren, Henning T Schmidt, Henrik Cederquist, et al. (2019). 'Ultraslow radiative cooling of C n-(n= 3–5).' In: *The Journal of Chemical Physics* 151.11, p. 114304.

Cairncross, William B., Daniel N. Gresh, Matt Grau, Kevin C. Cossel, Tanya S. Roussy, Yiqi Ni, Yan Zhou, Jun Ye, and Eric A. Cornell (2017). 'Precision Measurement of the Electron's Electric Dipole Moment Using Trapped Molecular Ions.' In: *Phys. Rev. Lett.* 119 (15), p. 153001. DOI: 10.1103/PhysRevLett.119.153001.

Chaibi, W., R. J. Pelaez, C. Blondel, C. Drag, and C. Delsart (2010). 'Effect of a magnetic field in photodetachment microscopy.' In: *The European Physical Journal D* 58. DOI: 10.1140/epjd/e2010-00086-7.

Chandrasekaran, Vijayanand, Bhim Kafle, Aneesh Prabhakaran, Oded Heber, Michael Rappaport, Hilel Rubinstein, Dirk Schwalm, Yoni Toker, and Daniel Zajfman (2014). 'Determination of absolute recurrent fluorescence rate coefficients for C6–.' In: *The Journal of Physical Chemistry Letters* 5.23, pp. 4078–4082.

Concina, Bruno, Franck Lépine, and Christian Bordas (2017). 'A detailed-balance model for thermionic emission from polyanions: The case of fullerene dianions.' In: *The Journal of Chemical Physics* 146.22, p. 224311.

Donnally, Bailey L. and George Thoeming (1967). 'Helium Negative Ions from Metastable Helium Atoms.' In: *Phys. Rev.* 159 (1), pp. 87–90. DOI: 10.1103/PhysRev.159.87.

Dunbar, Robert C (1992). 'Infrared radiative cooling of gas-phase ions.' In: *Mass Spectrometry Reviews* 11.4, pp. 309–339.

Dushman, Saul (1930). 'Thermionic emission.' In: *Reviews of Modern Physics* 2.4, p. 381.

Dyall, K.G., I.P. Grant, C.T. Johnson, F.A. Parpia, and E.P. Plummer (1989). 'GRASP: A general-purpose relativistic atomic structure program.' In: *Computer Physics Communications* 55.3, pp. 425–456. DOI: https://doi.org/10.1016/0010-4655(89)90136-7.

Ebara, Yuta, Takeshi Furukawa, Jun Matsumoto, Hajime Tanuma, Toshiyuki Azuma, Haruo Shiromaru, and K. Hansen (2016). 'Detection of recurrent fluorescence photons.' In: *Physical Review Letters* 117.13, p. 133004.

Fantz, U et al. (2007). 'Negative ion RF sources for ITER NBI: status of the development and recent achievements.' In: *Plasma Physics and Controlled Fusion* 49.12B, B563–B580. DOI: 10.1088/0741-3335/49/12b/s53.

Farley, John W. (1989). 'Photodetachment cross sections of negative ions: The range of validity of the Wigner threshold law.' In: *Phys. Rev. A* 40 (11), pp. 6286–6292. DOI: 10.1103/PhysRevA.40.6286.

Fedor, J, K Hansen, JU Andersen, and P Hvelplund (2005). 'Nonthermal power law decay of metal dimer anions.' In: *Physical review letters* 94.11, p. 113201.

Feldmann, D. (1971). 'Photoablösung von Elektronen bei Si- und NH2-.' In: *Zeitschrift für Naturforschung A* 26.6, pp. 1100–1101. DOI: doi:10.1515/zna-1971-0630.

Frenzel, U, U Hammer, H Westje, and D Kreisle (1997). 'Radiative cooling of free metal clusters.' In: *Zeitschrift für Physik D Atoms, Molecules and Clusters* 40.1, pp. 108–110.

Frenzel, U, A Roggenkamp, and D Kreisle (1995). ''Black-body'radiation of free niobium clusters heated by oxidation.' In: *Chemical physics letters* 240.1-3, pp. 109–113.

Frisch, MJ, GW Trucks, HB Schlegel, GE Scuseria, MA Robb, JR Cheeseman, G Scalmani, V Barone, GA Petersson, H Nakatsuji, et al. (2016). 'Gaussian 16 Revision C. 01. 2016; Gaussian Inc.' In: *Wallingford CT* 421.

Fritzsche, S. (2012). 'The Ratip program for relativistic calculations of atomic transition, ionization and recombination properties.' In: *Computer Physics Communications* 183.7, pp. 1525–1559. DOI: https://doi.org/10.1016/j.cpc.2012.02.016.

Froese Fischer, C., G. Gaigalas, P. Jönsson, and J. Bieroń (2019). 'GRASP2018—A Fortran 95 version of the General Relativistic Atomic Structure Package.' In: *Computer Physics Communications* 237, pp. 184–187. DOI: https://doi.org/10.1016/j.cpc.2018.10.032.

Galli, Daniele and Francesco Palla (2013). 'The dawn of chemistry.' In: *Annual Review of Astronomy and Astrophysics* 51, pp. 163–206.

Glover, Simon (2005). 'The formation of the first stars in the Universe.' In: *Space Science Reviews* 117.3, pp. 445–508.

Goudsmit, S and Ta-You Wu (1934). 'Note on the Spectrum of the Corona.' In: *The Astrophysical Journal* 80, p. 154.

Grant, I.P., B.J. McKenzie, P.H. Norrington, D.F. Mayers, and N.C. Pyper (1980). 'An atomic multiconfigurational Dirac-Fock package.' In: *Computer Physics Communications* 21.2, pp. 207–231. DOI: https://doi.org/10.1016/0010-4655(80)90041-7.

Gruebele, Martin and Peter Guy Wolynes (2004). 'Vibrational energy flow and chemical reactions.' In: *Accounts of chemical research* 37.4, pp. 261–267.

Grussie, F., A.P. O'Connor, M. Grieser, D. Müll, A. Znotins, X. Urbain, and H. Kreckel (2022). 'An ion-atom merged beams setup at the Cryogenic Storage Ring.' In: *Review of Scientific Instruments.* DOI: placeholder.

Grussie, Florian (2016). 'Experimental studies of ion-neutral reactions under astrophysical conditions.' PhD thesis. University of Heidelberg. DOI: https://doi.org/10.11588/heidok.00021435.

Haarhoff, P.C. (1964a). 'H-D isotope effects in the decomposition of acetylene by electron impact.' In: *Molecular Physics* 8.1, pp. 49–63. DOI: 10.1080/00268976400100061. eprint: https://doi.org/10.1080/00268976400100061.

Haarhoff, P.C. (1964b). 'The density of vibrational energy levels of polyatomic molecules.' In: *Molecular Physics* 7.2, pp. 101–117. DOI: 10.1080/00268976300100871. eprint: https://doi.org/10.1080/00268976300100871.

Hackermüller, Lucia, Klaus Hornberger, Björn Brezger, Anton Zeilinger, and Markus Arndt (2004). 'Decoherence of matter waves by thermal emission of radiation.' In: *Nature* 427.6976, pp. 711–714.

Hansen, K. (2008). 'Comparison of algorithms for the calculation of molecular vibrational level densities.' In: *The Journal of Chemical Physics* 128.19, p. 194103. DOI: 10.1063/1.2920483. eprint: https://doi.org/10.1063/1.2920483.

Hansen, K. (2013). *Statistical physics of nanoparticles in the gas phase.* Springer.

Hansen, K., JU Andersen, PREBEN Hvelplund, SP Møller, UV Pedersen, and VV Petrunin (2001). 'Observation of a 1/t decay law for hot clusters and molecules in a storage ring.' In: *Physical review letters* 87.12, p. 123401.

Harris, Robert A (1963). 'Predissociation.' In: *The Journal of Chemical Physics* 39.4, pp. 978–987.

Hartree, D. R. (1928). 'The Wave Mechanics of an Atom with a Non-Coulomb Central Field. Part I. Theory and Methods.' In: *Mathematical Proceedings of the Cambridge Philosophical Society* 24.1, pp. 89–110. DOI: 10.1017/S0305004100011919.

Hotop, H. and W. C. Lineberger (1975). 'Binding energies in atomic negative ions.' In: *Journal of Physical and Chemical Reference Data* 4.3, pp. 539–576. DOI: 10.1063/1.555524.

Iron, Mark A (2022). *Private communication.*

Iron, Mark A and Jonathan Gropp (2019). 'Cost-effective density functional theory (DFT) calculations of equilibrium isotopic fractionation in large organic molecules.' In: *Physical Chemistry Chemical Physics* 21.32, pp. 17555–17570.

Jönsson, P., X. He, C. Froese Fischer, and I.P. Grant (2007). 'The grasp2K relativistic atomic structure package.' In: *Computer Physics Communications* 177.7, pp. 597–622. DOI: https://doi.org/10.1016/j.cpc.2007.06.002.

Jordan, E., G. Cerchiari, S. Fritzsche, and A. Kellerbauer (2015). 'High-Resolution Spectroscopy on the Laser-Cooling Candidate La$^-$.' In: *Phys. Rev. Lett.* 115 (11), p. 113001. DOI: 10.1103/PhysRevLett.115.113001.

Kafle, Bhim, Ofer Aviv, Vijayamand Chandrasekaran, Oded Heber, ML Rappaport, Hilel Rubinstein, Dirk Schwalm, Daniel Strasser, and Daniel Zajfman (2015). 'Electron detachment and fragmentation of laser-excited rotationally hot Al 4-.' In: *Physical Review A* 92.5, p. 052503.

Karmakar, Sourav and Srihari Keshavamurthy (2020). 'Intramolecular vibrational energy redistribution and the quantum ergodicity transition: a phase space perspective.' In: *Physical Chemistry Chemical Physics* 22.20, pp. 11139–11173.

Kasdan, A., E. Herbst, and W. C. Lineberger (1975). 'Laser photoelectron spectrometry of the negative ions of silicon and its hydrides.' In: *The Journal of Chemical Physics* 62.2, pp. 541–548. DOI: 10.1063/1.430508.

Kassel, L. S. (1928). 'Studies in Homogeneous Gas Reactions. II. Introduction of Quantum Theory.' In: *The Journal of Physical Chemistry* 32.7, pp. 1065–1079. DOI: 10.1021/j150289a011.

Kellerbauer, Alban and Jochen Walz (2006). 'A novel cooling scheme for antiprotons.' In: *New Journal of Physics* 8.3, pp. 45–45. DOI: 10.1088/1367-2630/8/3/045.

Kreckel, H., H Bruhns, M Cizek, SCO Glover, KA Miller, Xavier Urbain, and DW Savin (2010). 'Experimental results for H2 formation from H- and H and implications for first star formation.' In: *Science* 329.5987, pp. 69–71.

Kreckel, H., J. Tennyson, D. Schwalm, D. Zajfman, and A. Wolf (2004). 'Rovibrational relaxation model for H$_3^+$.' In: *New Journal of Physics* 6, pp. 151–151. DOI: 10.1088/1367-2630/6/1/151.

Lange, Michael, Michael Wayne Froese, Sebastian Menk, Dennis Bing, Florian Fellenberger, Manfred Grieser, Felix Laux, Dmitri A Orlov, Roland Repnow, Thomas Sieber, et al. (2012). 'Radiative cooling of Al- 4 and Al- 5 in a cryogenic environment.' In: *New Journal of Physics* 14.6, p. 065007.

Laux, Felix (2011). 'Entwicklung von kapazitiven Positions-, Strom- und Schottkysignal-Messsystemen für den kryogenen Speicherring CSR.' PhD thesis. University of Heidelberg.

Lee, D. H., W. D. Brandon, D. J. Pegg, and D. Hanstorp (1997). 'Cross section for photodetachment of the excited C$^-$(^2D) ion using fast ion-laser-beam electron spectroscopy.' In: *Phys. Rev. A* 56 (2), pp. 1346–1350. DOI: 10.1103/PhysRevA.56.1346.

Li, Xi, Hongbin Wu, Xue-Bin Wang, and Lai-Sheng Wang (1998). 's-p hybridization and electron shell structures in aluminum clusters: A photoelectron spectroscopy study.' In: *Physical review letters* 81.9, p. 1909.

Luna, H., F. Zappa, M. H. Martins, S. D. Magalhães, G. Jalbert, L. F. Coelho, and N. V. de Castro Faria (2001). 'Comparative study of the collisional electron detachment of C-, Si-, and Ge- by light noble gases.' In: *Phys. Rev. A* 63.5, p. 052716. DOI: 10.1103/PhysRevA.63.052716.

Makarov, Aleksandr A, Aleksandr L Malinovsky, and Evgenii A Ryabov (2012). 'Intramolecular vibrational redistribution: from high-resolution spectra to real-time dynamics.' In: *Physics-Uspekhi* 55.10, p. 977.

Manikandan, Paranjothy and Srihari Keshavamurthy (2014). 'Dynamical traps lead to the slowing down of intramolecular vibrational energy flow.' In: *Proceedings of the National Academy of Sciences* 111.40, pp. 14354–14359. DOI: 10.1073/pnas.1406630111.

Marcus, R. A. (1952). 'Unimolecular Dissociations and Free Radical Recombination Reactions.' In: *The Journal of Chemical Physics* 20.3, pp. 359–364. DOI: 10.1063/1.1700424.

Massey, HSW (1938). *Negative ions 1st edn.*

Matthews, Devin A, Lan Cheng, Michael E Harding, Filippo Lipparini, Stella Stopkowicz, Thomas-C Jagau, Péter G Szalay, Jürgen Gauss, and John F Stanton (2020). 'Coupled-cluster techniques for computational chemistry: The CFOUR program package.' In: *The Journal of Chemical Physics* 152.21, p. 214108.

McCarthy, M. C., C. A. Gottlieb, H. Gupta, and P. Thaddeus (2006). 'Laboratory and Astronomical Identification of the Negative Molecular Ion C6H-.' In: *The Astrophysical Journal* 652.2, pp. L141–L144. DOI: 10.1086/510238.

Meier, U, SD Peyerimhoff, and F Grein (1990). 'Ab initio MRD-CI study of neutral and charged Ga2, Ga3 and Ga4 clusters and comparison with corresponding boron and aluminum clusters.' In: *Zeitschrift für Physik D Atoms, Molecules and Clusters* 17.3, pp. 209–224.

Meyer, C. et al. (2017). 'Radiative Rotational Lifetimes and State-Resolved Relative Detachment Cross Sections from Photodetachment Thermometry of Molecular Anions in a Cryogenic Storage Ring.' In: *Phys. Rev. Lett.* 119 (2), p. 023202. DOI: 10.1103/PhysRevLett.119.023202.

Meyer, Christian (2018). 'The lowest rotational quantum states of the hydroxyl anions probed by electron photodetachment in a cryogenic storage ring.' PhD thesis. University of Heidelberg.

Middleton, R (1989). *A negative ion cookbook.*

Mitzner, Rolf and Eleanor EB Campbell (1995). 'Optical emission studies of laser desorbed C60.' In: *The Journal of chemical physics* 103.7, pp. 2445–2453.

Müll, D. et al. (2021). 'Metastable states of Si^- observed in a cryogenic storage ring.' In: *Phys. Rev. A* 104 (3), p. 032811. DOI: 10.1103/PhysRevA.104.032811.

Nesbitt, David J and Robert W Field (1996). 'Vibrational energy flow in highly excited molecules: Role of intramolecular vibrational redistribution.' In: *The Journal of Physical Chemistry* 100.31, pp. 12735–12756.

Nielsen, S Brondsted, JU Andersen, JS Forster, P Hvelplund, B Liu, UV Pedersen, and S Tomita (2003). 'Photodestruction of adenosine 5-monophosphate (AMP) nucleotide ions in vacuo: statistical versus nonstatistical processes.' In: *Physical Review Letters* 91.4, p. 048302.

Nishino, H. et al. (2009). 'Search for Proton Decay via $p \to e^+\pi^0$ and $p \to \mu^+\pi^0$ in a Large Water Cherenkov Detector.' In: *Phys. Rev. Lett.* 102 (14), p. 141801. DOI: 10.1103/PhysRevLett.102.141801.

O'Connor, A. P. et al. (2016). 'Photodissociation of an Internally Cold Beam of CH^+ Ions in a Cryogenic Storage Ring.' In: *Phys. Rev. Lett.* 116 (11), p. 113002. DOI: 10.1103/PhysRevLett.116.113002.

O'Malley, Steven M and Donald R Beck (2003). 'Relativistic configuration interaction calculations of lifetimes of Si 3p3bound excited states.' In: *Journal of Physics B: Atomic, Molecular and Optical Physics* 36.21, pp. 4301–4309. DOI: 10.1088/0953-4075/36/21/009.

Pavlov, A. V. (2014). 'Photochemistry of Ions at D-region Altitudes of the Ionosphere: A Review.' In: *Surveys in Geophysics* 35. DOI: 10.1007/s10712-013-9253-z.

Peebles, PJE and RH Dicke (1968). 'Origin of the globular star clusters.' In: *The Astrophysical Journal* 154, p. 891.

Pegg, David J (2004). 'Structure and dynamics of negative ions.' In: *Reports on Progress in Physics* 67.6, pp. 857–905. DOI: 10.1088/0034-4885/67/6/r02.

Radloff, W, V Stert, Th Freudenberg, IV Hertel, C Jouvet, C Dedonder-Lardeux, and D Solgadi (1997). 'Internal conversion in highly excited benzene and benzene dimer: Femtosecond time-resolved photoelectron spectroscopy.' In: *Chemical Physics Letters* 281.1-3, pp. 20–26.

Rice, Oscar Knefler and Herman C. Ramsperger (1927). 'THEORIES OF UNIMOLECULAR GAS REACTIONS AT LOW PRESSURES.' In: *Journal of the American Chemical Society* 49.7, pp. 1617–1629. DOI: 10.1021/ja01406a001.

Rienstra-Kiracofe, Jonathan C., Gregory S. Tschumper, Henry F. Schaefer, Sreela Nandi, and G. Barney Ellison (2002). 'Atomic and Molecular Electron Affinities: Photoelectron Experiments and Theoretical Computations.' In: *Chem. Rev.* 102 (1). DOI: 10.1021/cr990044u.

Saha, K, V Chandrasekaran, O Heber, MA Iron, ML Rappaport, and D Zajfman (2018). 'Ultraslow isomerization in photoexcited gas-phase carbon cluster C10.' In: *Nature communications* 9.1, pp. 1–9.

Sarre, Peter J. (2006). 'The diffuse interstellar bands: A major problem in astronomical spectroscopy.' In: *Journal of Molecular Spectroscopy* 238.1, pp. 1–10. DOI: https://doi.org/10.1016/j.jms.2006.03.009.

Scheer, Michael, René C. Bilodeau, Cicely A. Brodie, and Harold K. Haugen (1998). 'Systematic study of the stable states of C^-, Si^-, Ge^-, and Sn^- via infrared laser spectroscopy.' In: *Phys. Rev. A* 58 (4), pp. 2844–2856. DOI: 10.1103/PhysRevA.58.2844.

Sherrill, C. David and III Schaefer Henry F. (1999). 'The Configuration Interaction Method.' In: *Advances in Quantum Chemistry* 34, pp. 143–269. DOI: 10.1016/S0065-3276(08)60532-8.

Sommerfeld, Thomas (2010). 'Al 4- cluster anion: Electronic structure, excited states, and electron detachment.' In: *The Journal of chemical physics* 132.12, p. 124305.

Spruck, Kaija et al. (2015). 'An efficient, movable single-particle detector for use in cryogenic ultra-high vacuum environments.' In: *Review of Scientific Instruments* 86.2, p. 023303. DOI: 10.1063/1.4907352.

Stanton, John F (1997). 'Why CCSD (T) works: a different perspective.' In: *Chemical Physics Letters* 281.1-3, pp. 130–134.

Stockett, Mark H, James N Bull, Jack T Buntine, Eduardo Carrascosa, Emma K Anderson, Michael Gatchell, Magdalena Kaminska, Rodrigo F Nascimento, Henrik Cederquist, Henning T Schmidt, et al. (2020). 'Radiative cooling of carbon cluster anions C2n+ 1-(n= 3–5).' In: *The European Physical Journal D* 74.7, pp. 1–9.

Sun, Jiao, Wen Cai Lu, Hong Wang, Ze-Sheng Li, and Chia-Chung Sun (2006). 'Theoretical study of Al n and Al n O (n= 2- 10) clusters.' In: *The Journal of Physical Chemistry A* 110.8, pp. 2729–2738.

Tang, Rulin, Yuzhu Lu, Hongtao Liu, and Chuangang Ning (2021). 'Electron affinity of uranium and bound states of opposite parity in its anion.' In: *Physical Review A* 103.5, p. L050801.

Thaddeus, P., C. A. Gottlieb, H. Gupta, S. Brünken, M. C. McCarthy, M. Agúndez, M. Guélin, and J. Cernicharo (2008). 'Laboratory and Astronomical Detection of the Negative Molecular Ion C3N-.' In: *The Astrophysical Journal* 677.2, pp. 1132–1139. DOI: 10.1086/528947.

Thomson, Joseph John (1913). 'Bakerian Lecture: Rays of positive electricity.' In: *Proceedings of the Royal Society of London. Series A, Containing Papers of a Mathematical and Physical Character* 89.607, pp. 1–20. DOI: 10.1098/rspa.1913.0057. eprint: https://royalsocietypublishing.org/doi/pdf/10.1098/rspa.1913.0057.

Toker, Y (2022). *Private communication.*

Toker, Y, Ofer Aviv, M Eritt, ML Rappaport, Oded Heber, Dirk Schwalm, and Daniel Zajfman (2007). 'Radiative cooling of Al 4- clusters.' In: *Physical Review A* 76.5, p. 053201.

Umeda, N., M. Kashiwagi, M. Taniguchi, H. Tobari, K. Watanabe, M. Dairaku, H. Yamanaka, T. Inoue, A. Kojima, and M. Hanada (2014). 'Long-pulse beam acceleration of MeV class H$^-$ ion beams for ITER NB accelerator.' In: *Review of Scientific Instruments* 85.2, 02B304. DOI: 10.1063/1.4825161.

Upton, TH (1987). 'A perturbed electron droplet model for the electronic structure of small aluminum clusters.' In: *The Journal of chemical physics* 86.12, pp. 7054–7064.

Vogel, Stephen (2016). 'Developments at an Electrostatic Cryogenic Storage Ring for Electron-Cooled keV Energy Ion Beams.' PhD thesis. University of Heidelberg. DOI: https://doi.org/10.11588/heidok.00020262.

von Hahn, R. et al. (2016). 'The cryogenic storage ring CSR.' In: *Review of Scientific Instruments* 87.6, p. 063115. DOI: 10.1063/1.4953888.

Walter, C. W., N. D. Gibson, Y.-G. Li, D. J. Matyas, R. M. Alton, S. E. Lou, R. L. Field, D. Hanstorp, Lin Pan, and Donald R. Beck (2011). 'Experimental and theoretical study of bound and quasibound states of **Ce⁻**.' In: *Phys. Rev. A* 84 (3), p. 032514. DOI: 10.1103/PhysRevA.84.032514.

Warring, U., M. Amoretti, C. Canali, A. Fischer, R. Heyne, J. O. Meier, Ch. Morhard, and A. Kellerbauer (2009). 'High-Resolution Laser Spectroscopy on the Negative Osmium Ion.' In: *Phys. Rev. Lett.* 102 (4), p. 043001. DOI: 10.1103/PhysRevLett.102.043001.

Wigner, Eugene P. (1948). 'On the Behavior of Cross Sections Near Thresholds.' In: *Phys. Rev.* 73 (9), pp. 1002–1009. DOI: 10.1103/PhysRev.73.1002.

Wildt, Rupert (1939). 'Electron Affinity in Astrophysics.' In: *The Astrophysical Journal* 89, pp. 295–301.

Wilhelm, Patrick (2019). 'First Studies of Low-Energy Electron Cooling of keV Energy Ion Beams at the Electrostatic Cryogenic Storage Ring CSR.' PhD thesis. University of Heidelberg. DOI: https://doi.org/10.11588/heidok.00026821.

Zhao, YL and RJ Zhang (2007). 'Structures and properties of stable Al4, Al4+, and Al4- comparatively studied by ab initio theories.' In: *The Journal of Physical Chemistry A* 111.30, pp. 7189–7193.

Danksagung

Ich möchte mich für das Zustandekommen dieser Arbeit bei allen Menschen bedanken, die mich auf diesem Weg begleitet und unterstützt haben. Ganz besonders will ich mich bei folgenden Menschen bedanken:

Prof. Dr. Klaus Blaum für die Möglichkeit eine Promotion in der Arbeitsgruppe zu beginnen.

PD Dr. Holger Kreckel für die ausgezeichnete fachliche Führung, Betreuung und die zahlreichen Hilfestellungen.

Yoni Toker für die zahlreichen Diskussionen und die immer freundliche und hilfsbereite Art.

Prof. Dr. Andreas Wolf, Dr. Oldřich Novotný, Dr. Sebastian George für die herzliche Aufnahme in die CSR Gruppe und die hilfreichen Diskussionen und Erklärungen.

Dr. Florian Grussie für die zahlreichen Hilfestellungen und Gespräche vor allem zu Beginn meiner Zeit am Institut. Alle gemeinsamen Strahlzeiten sind mir hierbei sehr positiv im Gedächtnis geblieben.

Viviane und Felix für die zahlreichen gemeinsamen Male an denen wir den CSR gesperrt haben, um anschliessend den Laser zu bereits fortgeschrittener Stunde einzurichten.

Meinen anderen Kollegen: Abel, Aigars, Daniel, Julia, Leonard, Lisa, Lukas für die gemeinsamen Mittags oder Kaffeepausen und die angenehm ablenkenden Gespräche, auch und vor allem während des Zusammenschreibens der Arbeit.

Dem CSR-Team für die vielen Unterstützungen und die oft sehr kurzen Wartezeiten falls es doch mal ein Problem am Experiment gab.

Meinen besten Freunden Marc und Christian für die vielen gemeinsamen Aktiviäten, die mit euch jederzeit möglich waren. Die Motivation und Ablenkung, waren einfach großartig.

Meinen Eltern für die bedigungslose seelische und moralische Unterstützung.

Meiner Freundin Sofie, die mir zu jedem Zeitpunkt Rückhalt geboten hat und es immer verstanden hat mich weiter zu motivieren.

Allen anderen Freunden, Bekannten und Kollegen.